Design and construction of a test stand for photocathode research and experiments

Konstruktion und Bau eines Teststands für Photokathodenforschung und Experimente
Vom Fachbereich Physik der Technische Universität Darmstadt zur Erlangung
des Grades eines Doktors der Naturwissenschaften (Dr. rer. nat.)
genehmigte Dissertation von Neeraj Kurichiyanil, M.Sc. aus Kerala, India.
Januar 2017, Darmstadt — D 17

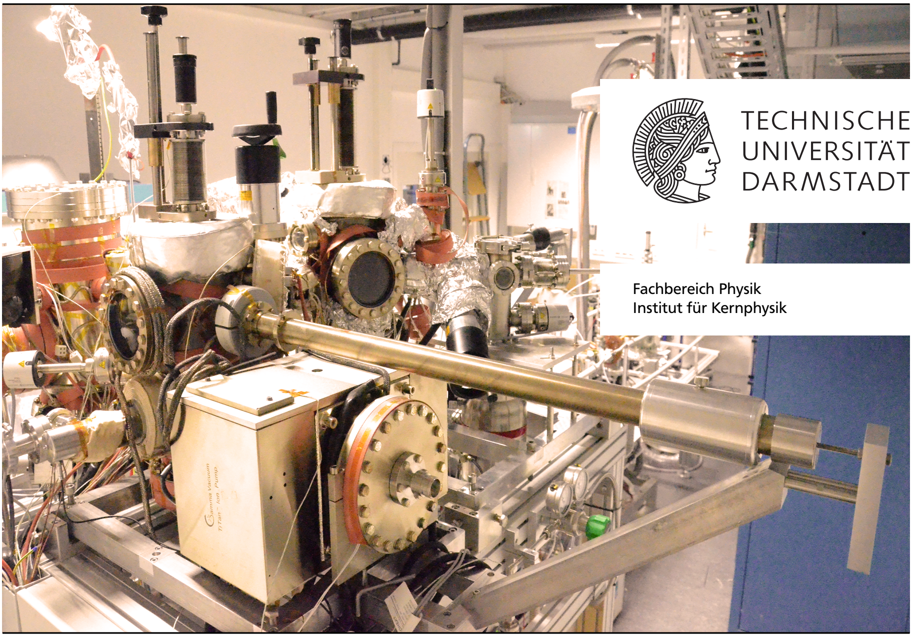

TECHNISCHE
UNIVERSITÄT
DARMSTADT

Fachbereich Physik
Institut für Kernphysik

Funded by DFG through SFB 634 and GRK 2128

Design and construction of a test stand for photocathode research and experiments
Konstruktion und Bau eines Teststands für Photokathodenforschung und Experimente

Genehmigte Dissertation von Neeraj Kurichiyanil, M.Sc. aus Kerala, India.

1. Referee: Prof. Dr. Joachim Enders
2. Referee: Prof. Dr. Markus Roth

Tag der Einreichung: 12 Juli 2016
Tag der Prüfung: 14 November 2016

Darmstadt — D 17

Bitte zitieren Sie dieses Dokument als:
URN: urn:nbn:de:tuda-tuprints-59037
URL: http://tuprints.ulb.tu-darmstadt.de/5903

Dieses Dokument wird bereitgestellt von tuprints,
E-Publishing-Service der TU Darmstadt
http://tuprints.ulb.tu-darmstadt.de
tuprints@ulb.tu-darmstadt.de

Die Veröffentlichung steht unter folgender Creative Commons Lizenz:
Namensnennung–Keine kommerzielle Nutzung–Keine Bearbeitung
4.0 Deutschland
https://creativecommons.org/licenses/by-nc-nd/4.0/de

Printed with support from the German Academic Exchange Service (DAAD)

Quod gratis asseritur, gratis negatur.
What can be asserted without evidence,
can be dismissed without evidence.

- *Latin proverb*.

Abstract

Within the scope of this thesis, a test stand Photo-CATCH for research on semiconductor photocathodes used at the spin-polarized electron injector of the superconducting Darmstadt electron linear accelerator S-DALINAC is constructed and brought into operation. Ultra-high vacuum conditions are achieved in all parts of the system. Atomic-hydrogen assisted low-temperature cleaning of cathodes in a chamber with base pressure better than 3×10^{-11} mbar is used for preparing clean cathode surfaces for negative electron affinity (NEA) activation. Using a standardised activation procedure, atomic-hydrogen cleaning of heavily contaminated bulk-GaAs samples is optimized to an upper limit of 10 kL hydrogen-dosage. Cleaning of samples has been performed with a dosage as low as 0.7 kL. Activation of photocathodes with $\mathrm{Cs+O_2}$ and $\mathrm{Cs+Li+O_2}$ have been studied in a dedicated vacuum chamber with base pressure better than 2×10^{-11} mbar. By using a 405 nm laser, quantum efficiencies above 25% have been achieved from an NEA-GaAs photocathode. Oxygen-induced quantum-efficiency degradation of NEA cathodes has been investigated. A vacuum lifetime of (298±35) hours was observed in the activation chamber for a novel two-stage activation using Cs, O_2 and Li. This system can provide photocathodes with high quantum efficiency and lifetime for polarized and unpolarized beam production at the 60 keV electron beamline of Photo-CATCH. Additionally, atomic-hydrogen cleaned cathode samples can be transported to the photoelectron source at S-DALINAC using a transport-vessel conceptualized in this work.

Zussamenfassung

Im Rahmen dieser Arbeit wurde der Teststand Photo-CATCH zur Untersuchung von Halbleiter-Photokathoden, welche am spin-polarisierten Elektroneninjektor des supraleitenden Darmstädter Elektronenlinearbeschleunigers S-DALINAC genutzt werden, entwickelt und instandgesetzt. Ultrahochvakuumbedingungen wurden in allen Teilen des Systems erreicht. Atomare Wasserstoff unterstützte Niedertemperaturreinigung von Kathoden in einer Kammer mit einem Basisdruck von weniger 3×10^{-11} mbar wurde für die Präparation sauberer Kathodenoberflächen für negative Elektronenaffinitätsaktivierung (NEA) genutzt. Durch Nutzung einer standardisierten Aktivierungsprozedur wurde die atomare Wasserstoffreinigung von stark kontaminierten bulk-GaAs Proben auf ein oberes Limit von 10kL Wasserstoffdosierung optimiert. Die Reinigung der Proben wurde mit einer Dosis bis zu 0.7 kL durchgeführt. Die Aktivierung von Photokathoden mit $Cs+O_2$ und $Cs+Li+O_2$ wurden in einer dafür vorgesehenen Vakuumkammer mit einem Basisdruck von $<2 \times 10^{-11}$ mbar untersucht. Durch die Nutzung eines 405 nm Lasers wurden Quanteneffizienzen von über 25% aus NEA-GaAs Photokathoden erreicht. Sauerstoff induzierte Quanteneffizienzverschlechterung der NEA Kathoden wurde untersucht. Eine Vakuumlebensdauer von (298±35) Stunden wurde in der Aktivierungskammer für eine neuwertige Zwei-Stufen-Aktivierung mit Cs, O_2 und Li beobachtet. Das System kann Photokathoden mit hoher Quanteneffizienz und Lebensdauer für polarisierte und unpolarisierte Strahlerzeugung bei der 60 keV Elektronenstrahlführung von Photo-CATCH liefern. Zusätzlich können mit atomaren Wasserstoff gereinigte Kathoden zu der Photoelektronenquelle des S-DALINAC durch die Verwendung eines Transportgefäßes, welches in dieser Arbeit entworfen wurde, transportiert werden.

Contents

1 Introduction

Photoelectron sources are in wide use ranging from optoelectronic devices to high-energy particle physics. Common electron sources used at accelerators are based on field emission, thermionic emission, photo-electric emission, or seldom a combination of all three [1, 2]. Accelerator photoelectron sources can be categorized into direct current (DC) and radio frequency (RF) electron-guns, of which the DC electron-gun technology is considered to be the most mature [3]. In DC-guns, a static electric field, parametrized by a potential difference Φ, applied between the cathode and the anode accelerate particles of charge q to a final energy of $q \cdot \Phi$ eV. Further acceleration using RF structures are necessary to boost the charges to higher energies. The limits on achievable gradient around $7\,\mathrm{MV\,m^{-1}}$ and applicable high-voltage of 750 kV on present day DC-guns are set by field emission, dark currents and electric field breakdown in vacuum [3, 4]. However, only DC-photoguns are capable of holding the extreme ultra-high vacuum (XHV) conditions required by semiconductor photocathodes used for high-brightness and polarized electron beam production, and the use of an RF photoinjector for this purpose, with high operational reliability, is yet to be demonstrated [5, 6]. The superconducting electron linear accelerator of Darmstadt S-DALINAC [7] features a DC spin-polarized electron gun [8] based on photoemission from Gallium Arsenide (GaAs) photocathodes, operating at −100 kV potential, which is complementary to the −250 kV DC thermionic gun.

For the success of experimental programs using polarized electron beams [9–11], it is desirable that the S-DALINAC Polarized Injector SPIN durably delivers electron beams with a high degree of polarization greater than 80% at suitable currents up to tens of μA. Strained-layer and strained-superlattice structures of GaAs and Indium-GaAs or GaAs-Phosphide are used at SPIN to produce polarized electron beams, following other polarized-electron facilities in operation around the world [12–15]. In spite of offering high average current, polarized emission, fast response and low thermal-emittance, which are tremendously sought by modern accelerator sources, the downside of GaAs-based semiconductor photocathodes lies in their poor lifetimes–the amount of time to which the cathode is able to maintain a satisfactory photoresponse–compared to conventional unpolarized metallic photocathodes [16–19]. Photocathodes providing high average currents of 10 to 100 mA and possessing long lifetimes are in high demand by energy recovery linacs (ERL) and continuous wave photoinjectors [20–22]. High availability of SPIN is expected during the planned ERL operation of S-DALINAC within the *AccelencE* initiative at the Institut für Kernphysik (IKP) of TU Darmstadt. A more efficient, reliable, and stable polarized electron source is also of interest to future accelerators for particle physics experiments, such as the International Linear Collider (ILC) [23].

Two issues have to be tackled in order to increase the performance of the photocathodes at SPIN. Firstly, since the semiconductor photocathode surfaces are easily contaminated both by native surface oxides and reactive gases in the operational environment [24, 25], an effective surface cleaning mechanism is essential to reproducibly prepare atomically clean sample surfaces. Moreover, subsequent surface contamination of cleaned cathodes needs to be prevented by observing stringent vacuum conditions during their storage as well as possible transport. Secondly, the surface modification technique known as the negative electron affinity (NEA) activation has to be optimized to ensure both longevity and high quantum efficiency (the number of electrons emitted per photon) , QE, of the cathodes [26, 27]. It is often observed that the NEA activation parameters for the highest lifetime do not always correspond to those for the highest quantum yield. In essence, the performance of GaAs photocathodes in an electron gun ultimately depends on the quality of the photocathode preparation and the vacuum conditions in the source-chamber. Therefore, to achieve the best performance of the GaAs cathodes at SPIN, a systematic study of cathode preparation techniques and the testing of a novel design of the high voltage gun are vital.

The preparation of a photocathode involves mainly two stages: a) producing an atomically clean cathode surface and b) depositing a thin layer of alkali-oxidant mixture on the cleaned surface, a process known as *activation*. These procedures together take hours to complete and a systematic analysis of these processes would require frequent cathode-preparations. To conduct research on cleaning and activation methods on cathodes being used at the SPIN without interrupting the accelerator beamtimes, a standalone system is required. Such a system must be capable of establishing a better surface cleaning procedure for the GaAs crystals and in addition, should include novel activation techniques and derive reproducible activation recipes. In this regard, a test stand *Photo-CATCH* is constructed at IKP. This dissertation presents the design, construction and operation of the photocathode preparation system of the Photo-CATCH set-up. The design and construction of an inverted-insulator geometry electron-gun and a diagnostic beamline of this facility is described in the reference [28].

Chapter 2 presents the S-DALINAC and SPIN, and discusses their operational parameters relevant to the design of Photo-CATCH. In this chapter, the case for further research on photocathode preparation is set forth. The physics of photoemission from GaAs photocathodes is introduced in **chapter 3**. A brief discussion about spin-polarized electron emission from lattice-strained cathodes and the steps involved in cathode preparation for an accelerator photoelectron source are given. **Chapter 4** details the design of Photo-CATCH system. Basic vacuum technology required for ultra-high vacuum production is discussed along with specifications of associated process-chambers. The particulars of the 60 keV polarized electron beamline of Photo-CATCH and associated diagnostics elements are also outlined. First experimental findings using the preparation facility are presented and discussed in **chapter 5**. The influence of different activation procedures on the final performance of the cathode, behavior of GaAs photocathodes activated with multiple alkali, and parameters for atomic hydrogen cleaning of the photocathodes are evaluated. **Chapter 6** gives a summary of the thesis.

2 S-DALINAC

The Superconducting-DArmstadt LINear ACcelerator S-DALINAC is a recirculating, continuous wave (cw) electron linear accelerator housed in the Institut für Kernphysik of Technische Universität Darmstadt. It has been providing continuous electron beams of up to 85 MeV for nuclear and radiation physics experiments since the beginning of 1991 [29, 30]. The layout of the accelerator facility can be seen in figure 2.1. Electrons are generated from either a −250 kV thermionic injector providing a continuous beam of electrons or a source of spin-polarized electrons, based on photoemission from GaAs photocathodes, capable of producing bunched or continuous beams. The superconducting (sc) injector module accelerates electron bunches to 10 MeV prior to their injection into the main accelerator structure. The injection section contains a 2-cell ($\beta = 0.85$) and a 5-cell ($\beta = 1$) capture cavities as well as two 20-cell cavities. The main structure has eight 20-cell cavities and provides an energy gain of 40 MeV. The superconducting cavities are made of Niobium (Nb) and operate at 3 GHz at a liquid helium temperature of 2 K.

Principal areas of research at the S-DALINAC are nuclear structure physics, nuclear astrophysics, quantum physics and radiation science. Five experimental facilities are prominent. A Quadrupole-Clam (QCLAM) magnetic spectrometer [31] is used for (e,e′x) experiments and inelastic (e,e′) scattering, in particular at 180°. The 169.7° magic-angle double-focussing Lintott[1] spectrometer with its beam transport system is used for high-resolution electron scattering experiments [32]. The low-energy photon tagger (NEPTUN) is able to tag bremsstrahlung photons in an energy range of 6 to 20 MeV [33]. Tagged photons are used to study energy dependence of the photodissociation cross-section especially in the astrophysically relevant region close above the threshold in the case of (γ,n) reactions [34]. The Darmstadt High Intensity Photon Setup (DHIPS) is used to perform photon scattering (γ,γ') experiments. It is located beyond the injector section of the accelerator and utilizes bremsstrahlung produced by 10 MeV electrons [35]. At this site, the DArmstadt GAmma ray Tracking Assembly (DAGATA) is foreseen to measure the polarization of high-energy gamma rays in a region of several MeV where the analyzing power of the Compton effect is too low for the use of conventional Compton polarimeters [36].

---

[1] Lintott Engineering Ltd., Sussex, England.

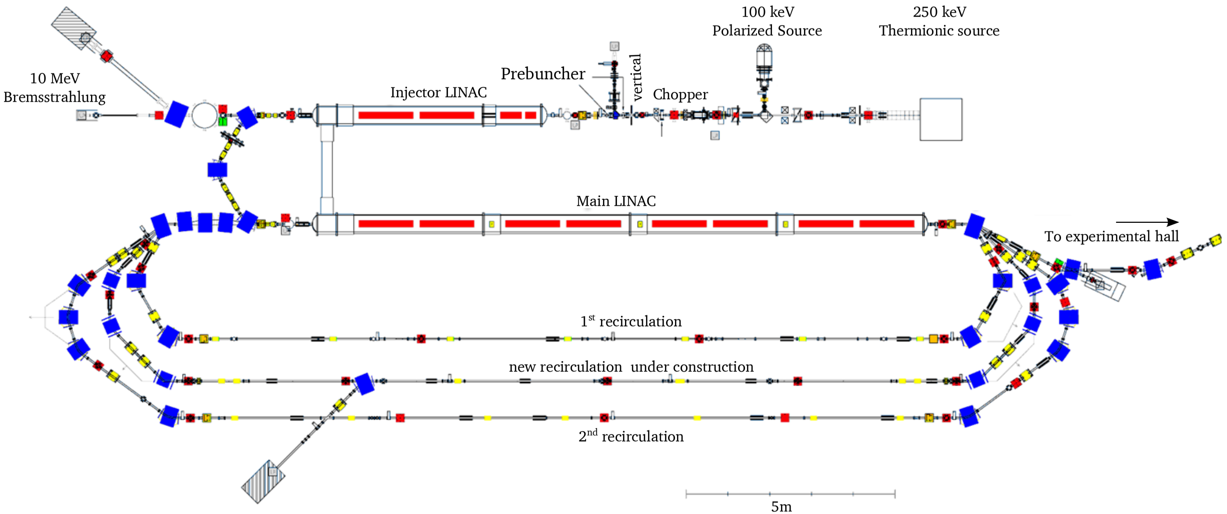

Figure 2.1: The layout of the superconducting Darmstadt linear accelerator S-DALINAC. Electron beams from either the thermionic gun or the photoelectron source are pre-bunched and accelerated by the injector module. The beam can be recirculated through the main LINAC up to three times to reach the maximum energy. Extraction is possible after the injector section to the bremsstrahlung area, or after each turn to different experimental caves that are not shown in the picture [37].

Due to the recirculating design, up to three passes of the beam through the main structure is possible, leading to the ultimate design energy of 130 MeV. Since the electron beam can be extracted after each pass, S-DALINAC can ideally provide electron beams with energies from 0.1 to 130 MeV with currents up to 20 μA for physics experiments [7, 38]. The main design parameters of S-DALINAC are summarized in table 2.1. An upgrade to the accelerator, to meet the requirements of nuclear resonance fluorescence experiments at the DHIPS, will replace the injection module changing the old injection energy 10 MeV and current 60 μA to 14 MeV and 200 μA, respectively [39, 40]. The accelerator is currently undergoing a design upgrade phase with the addition of a new recirculation path between the first and the second recirculations as shown in figure 2.1. This upgrade will modify the energy gain in each of the accelerating sections while increasing the final energy in the cw operation to achieve the original design energy by four passes of the beam through the main accelerator structure [41].

Beam energy	0.1–130 MeV
Energy spread	$\leq \pm$ 13 keV
cw current	$\leq$ 20 μA
Operating frequency	2997 GHz
Number of 20-cell cavities (1 m)	10
5-cell cavity (0.25 m, $\beta = 1$)	1
2-cell cavity (0.085 m, $\beta = 0.85$)	1

Table 2.1: A summary of the main design parameters of S-DALINAC.

2.1 The spin-polarized injector

The photoelectron source of spin-polarized electrons, the S-DALINAC Polarized Injector SPIN, provides the experimental programmes at S-DALINAC with spin-polarized electrons since late 2010 [8, 10, 42, 43]. The injector design is an adaptation of the MAMI[2] source of polarized electrons [15], modified to allow for the space constraints at S-DALINAC. SPIN is situated next to the thermionic gun, as shown in figure 2.1, and is placed vertically to the beamline which it shares with the thermionic source. As the use of semiconductor photocathodes require supreme vacuum condition in contrast to that in the thermionic emission source and in the

---

[2] Mainz Microtron, Mainz, Germany.

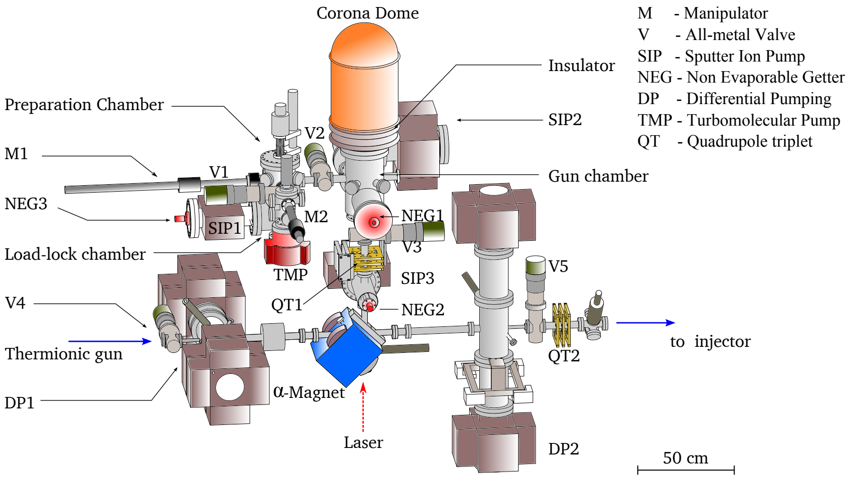

Figure 2.2: Schematic of spin-polarized electron injector of S-DALINAC. The differential pumping stages DP1 and DP2 isolate the ultra-high vacuum environment in SPIN from the thermionic gun (left) and the accelerator beamline (right). The cathode is activated to NEA in the preparation chamber and transferred to the gun-chamber for polarized beam extraction. The corona dome electrically shields the 100 kV contact. Laser enters from below the gun through the α-magnet chamber which bends the photoemitted electrons focused by a quadrupole-triplet, into the horizontal beamline.

beamline, and since the back-streaming ions produced by electron impact ionization during the accelerator operation are detrimental to the photocathode surface, the SPIN gun-chamber and its beam transport line are kept at ultra-high vacuum (UHV) conditions via differential pumping. An α-magnet bends the photoemitted electrons into the horizontal plane by an angle of 270°. Essential components downstream the beamline include a chopper and pre-buncher system as well as several beam steering and diagnostic elements. A Wien filter [44–46] for manipulating the electron spin orientation and a Mott polarimeter [47–49] for the determination of the degree of polarization of the electron beam are available.

A schematic drawing of SPIN is presented in figure 2.2. The SPIN subsystems include a load-lock chamber (LLC) for fast entry of the samples into a UHV chamber for cleaning and NEA activation. The LLC is pumped by a $180\,\mathrm{l\,s^{-1}}$ turbo-molecular pump backed by a diaphragm pump, and is capable of reaching a base pressure below 1×10^{-8} mbar. A GaAs crystal piece of 11 mm × 11 mm is held inside a molybdenum puck (figure 2.3) using a tungsten (W) spring and loaded into the LLC. A magnetically coupled manipulator can then transport the puck into the preparation chamber, where up to eight cathode pucks could be stored in a carousel. The preparation chamber is pumped by a combination of a $100\,\mathrm{l\,s^{-1}}$ sputter ion pump (SIP) and a $400\,\mathrm{l\,s^{-1}}$ non-evaporable getter (NEG). During a typical cleaning and NEA activation cycle, the pressure in this chamber rises up to, but never allowed to exceed, 1×10^{-8} mbar and 5×10^{-9} mbar, respectively. Surface cleaning is performed by annealing the sample at 580 °C for ≥30 minutes, depending on the surface contamination. After a cool-down time of about 40 minutes, the sample is activated to negative electron affinity (NEA) by depositing a layer of caesium (Cs) and oxygen (O_2) on its surface. The photo-response is monitored using a He-Ne laser (633 nm) of a few μW and a ring anode positioned below the photocathode.

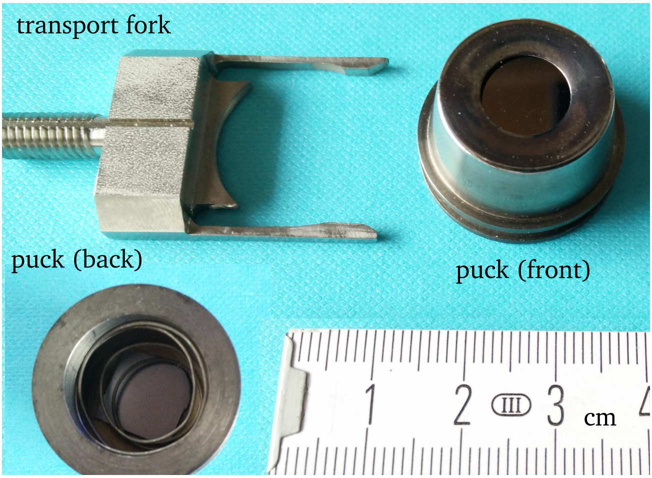

Figure 2.3: Photograph of the transport fork and the puck holding a photocathode sample. Inside the vacuum annealed molybdenum puck, a square piece of GaAs is held in position using a tungsten spring. The circular section of the crystal face exposed on the front side is used as the photoemitting surface.

The 100 kV electrode in the gun-chamber has a modified Pierce type geometry [42, 50]. The high-voltage is isolated externally by a conventional large-bore cylindrical alumina (Al_3O_2)-ceramic insulator and is corona shielded by a dome structure to prevent electric sparks. The activated cathodes are transferred using a magnetically coupled linear transfer arm to the cathode-elevator in the electrode for polarized electron beam extraction. The gun vacuum chamber is pumped by a $400\,\mathrm{l\,s^{-1}}$ SIP and $400\,\mathrm{l\,s^{-1}}$ NEG combination, in addition to a $1300\,\mathrm{l\,s^{-1}}$ NEG pump. A base pressure better than 1.9×10^{-11} mbar is measured by a hot-cathode vacuum gauge.

SPIN is driven by either a Titanium-Sapphire (Ti:Sapph) laser or one of the available diode-laser systems. The current optimum wavelength corresponding to the maximum polarization is 780 nm, but may vary depending on the structure of the photocathodes used. To be able to use different cathode types for polarized beam production at SPIN, a laser system with a tunable wavelength range is ideal. The wavelength of the available Ti:Sapph laser system is adjustable between 680 to 1000 nm and it can provide up to 1 W of laser power. Laser pulses as short as 220 fs at a repetition rate of 75 MHz, which is the 40th harmonic of S-DALINAC's operating frequency, can be generated using this system. The Ti:Sapph is situated in a dedicated laser laboratory about 40 m away from SPIN, and a stabilized transport of the laser beam to the source is realized via a system of mirrors in evacuated tubes [51]. Circularly polarized light required for spin-polarized emission is generated from the linearly polarized laser using a Pockels cell that can alter the photon helicity at a rate of up to 30 Hz, and the degree of polarization is determined using a Stokes polarimeter [52]. Polarized electron pulses with a repetition rate of 3 GHz can be produced from super-lattice cathodes using a 780 nm diode laser set-up near SPIN. Unpolarized beams of very high current can be drawn in continuous-mode using a diode-laser system with average power up to 800 mW and wavelength of 415 nm.

2.2 Operational challenges at SPIN

At SPIN, it has been possible to produce highly polarized beams with degrees of polarization as high as 86% from a stained-superlattice GaAs/GaAsP cathode B702[3]. A lower degree of polarization was observed from a strained-layer GaAs/InGaAs structure[4]. Extraction of electron pulses of lengths ≤5 ps from a superlattice cathode was also verified [53]. The latest results on the photocathode performance at SPIN are summarized in table 2.2.

The heat-cleaning of photocathodes practised at SPIN has several disadvantages. The cleanliness of a heat cleaned cathode surface, directly influencing the resulting *QE* of the activated cathode, depends strongly on the annealing temperature. For

---

[3] SVT Associates, Inc. Minnesota, USA.

[4] Saint Petersburg State University, Russia

Type	QE (%)	P (%)	Lifetimes Vacuum (hours)	Charge (C)
bulk	–	35.5 ± 1.4	300 ± 14	–
Strained layer	–	75.1 ± 2.1	1164 ± 165	–
Strained-superlattice	0.32	86.1 ± 1.4	–	9.6 ± 0.7

Table 2.2: Available data on the performance of various cathodes used at SPIN [53]. Peak polarization is obtained at 830 nm from bulk and strained-layer cathodes, and at 780 nm from a strained-superlattice. Vacuum lifetime of the strained-layer cathode was measured at the gun-chamber, and that of the bulk was measured in the preparation chamber at a test stand.

example, the QE after a heat cleaning at 450 °C is found to be two times lower than that obtained after cleaning at 600 °C [54]. The GaAs photocathodes have a heavily doped thin top-layer of few nanometers to produce the necessary band-bending for high QE and for the removal of the charge limiting phenomenon [55]. Heat cleaning close to 600 °C promotes dopant diffusion resulting in a reduced band-bending effect. Also there is a risk in heating close to the incongruent evaporation temperature of GaAs(100) face, which is between 657 to 663 °C. Close to this temperature Ga and As evaporate at different rates leaving the surface with Ga droplets, whereas As-stabilized surface is preferred for the operation of the NEA cathode [12]. It has been reported that the required temperature increases linearly with the oxide layer thickness on the sample surface, but at the same time higher temperatures result in rougher GaAs surfaces [56]. In the case of multilayer structures of GaAs used for highly polarized electron production, a high-temperature cleaning may cause strain relaxation due to differing thermal expansion coefficients of the mismatched lattices. It is crucial to avoid this as it will cause an irrecoverable damage to the multilayer structure and will consequently reduce the degree of polarized emission from such cathodes. In contrast, a lower temperature cleaning alone cannot effectively remove all the impurities found on GaAs surfaces. Atomic-hydrogen (H_1) assisted low-temperature surface cleaning is a well-known technique for removing oxides and carbon contaminants from a semiconductor surface. A detailed discussion about this method is given in chapter 3.

A reproducible recipe for activating both bulk and superlattice photocathodes is highly desirable for the steady operation of the photoelectron source. The activation procedure followed at SPIN requires manually controlling the Cs dispenser current and O_2 leak-rate while simultaneously observing the photo-response from the cathode. Although this approach has been able to produce cathodes with reasonable photo-yields, the repeatability is found to be rather poor [53, 57]. Establishing a computer controlled, automated activation procedure will be beneficial for activation studies on various cathode materials as well as for supplying SPIN with high performance photocathodes. Testing different activation methods other than the conventional co-deposition could result in improved QE as well as longer lifetimes.

The beam injection from SPIN into the accelerating structure of S-DALINAC requires an additional 2-cell superconducting-cavity due to the low operating potential of the source compared to the thermionic-gun. Injection at energy similar to the thermionic-gun, i.e. $\geq$200 keV, maybe possible with an upgrade of the SPIN gun to an inverted-insulator geometry gun resembling those at SLAC[5] or TJ-NAF[6] [58,59]. Moreover, the operation of a photoelectron gun at a higher potential reduces the space-charge effects that influence the extracted electron-bunch length and the transverse emittance of the beam. The main difficulty in adapting one of the existing inverted insulator geometry electron gun designs is to integrate the cathode-elevator concept used at SPIN into these fixed-electrode type designs. The feasibility of such an arrangement will have to be tested to overcome first the engineering, and then the operational difficulties in order to commission an upgraded gun at SPIN in the future. Opportunity for research is also present in improving the accuracy of the polarization measurements using an electron-polarimeter based on double Mott scattering [60, 61].

Since both the electron sources of S-DALINAC share a beamline, the availability of SPIN as a platform for research on photocathode performance and new operational concepts depends on the S-DALINAC run schedules. A standalone facility dedicated to research can serve as a test bench for future photocathodes for SPIN and concurrently function as a set-up to perform experiments with low-energy spin-polarized electrons.

---

[5] Stanford Linear Accelerator Center

[6] Thomas Jefferson National Accelerator Facility

3 Physics of photocathodes

During 1950-70's, Einstein's model of photoemission has undergone immense revision due to the emergence of alkali-antimony and group III-V photoemitters, giving way to a more sophisticated formulation of the photoemission process leading to a three-step model (TSM), largely due to works of W. E. Spicer and C. N. Berglund [62–65]. Photoemission in solids is treated as a multi-step bulk-phenomenon by TSM, as opposed to earlier theories that attributed surface phenomena to the process [66–68]. Photoemission, as a bulk-effect, proceeds through three stages:

- photoexcitation of electrons from the valance band into the conduction band, which depends on the absorption coefficient $\alpha(h\nu)$,
- transport of the excited electrons to the material surface, influenced by the ratio of the absorption length ℓ_α and the diffusion length $\mathcal{L}$ of the photoelectrons,
- and emission of electrons into the vacuum, determined by the escape probability $\mathcal{P}_{\mathrm{E}}(h\nu)$ at the surface of the material.

Figure 3.1 depicts the photoemission process in a semiconductor. The minimum energy required by a photon to excite an electron from the valance band maximum (VBM) into the conduction band minimum (CBM) is determined by the forbidden energy-band gap, $\mathcal{E}_{\mathrm{G}}$. The escape of the excited electrons from the conduction band into the vacuum depends upon the electron affinity, $\mathcal{E}_{\mathrm{A}}$, at the material surface which defines the energy difference between CBM and the vacuum level, $\mathcal{E}_{\mathrm{VAC}}$. The photoemission criteria in a semiconductor can be written as [69]

$$h\nu = \mathcal{E}_{\mathrm{G}} + \mathcal{E}_{\mathrm{A}} = e\phi + \delta\mathcal{E}_{\mathrm{VF}} \quad , \tag{3.1}$$

where $h\nu$ is the photon energy, $e\phi$ is the material workfunction defined as the energy difference between the Fermi-level, $\mathcal{E}_{\mathrm{F}}$, and vacuum. $\delta\mathcal{E}_{\mathrm{VF}}$ is the energy difference between VBM and $\mathcal{E}_{\mathrm{F}}$. Photoelectrons which have insufficient kinetic energy to overcome the potential barrier posed by $\mathcal{E}_{\mathrm{A}}$ at the surface, fail to make their escape to constitute a photocurrent and are eventually recombined through radiative and non-radiative processes. Most of the photoemitters naturally possess

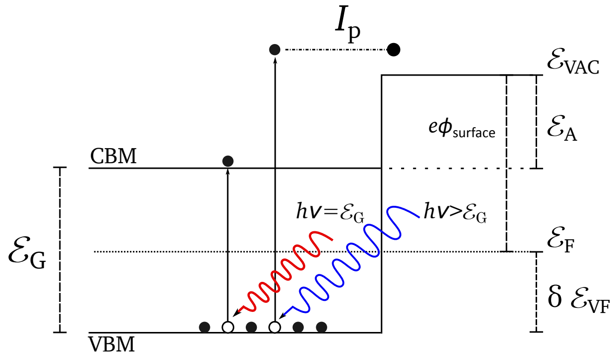

Figure 3.1: Upon absorption of photons, the electrons in the valance band maximum (VBM) are excited into the conduction band minium (CBM). $\mathcal{E}_G$, $\mathcal{E}_A$, $\mathcal{E}_{VAC}$, $e\phi_{surface}$ are the band-gap energy, electron affinity, vacuum level and the workfunction of the material, respectively. Electrons excited to CBM have to overcome the potential barrier $\mathcal{E}_A$ at the surface to be emitted from the material, allowing photoemission majorly to excitation with photons of energy $h\nu \geq \mathcal{E}_G + \mathcal{E}_A$.

a positive value for their electron affinity (PEA), making them poor candidates for high current applications.

An important qualifier for a photocathode is its quantum efficiency, QE, defined as the ratio of the number electrons emitted to the number of absorbed photons. The TSM assigns specific probabilities to the three independent stages of photoemission. The QE can then be calculated as a product of these probabilities, and is given as [70]

$$QE = \frac{(\alpha_{pe}/\alpha)\cdot\mathcal{P}_E}{1+(\ell_\alpha/\mathcal{L})} \quad , \tag{3.2}$$

where α_{pe}/α represents the fraction of electrons excited above the vacuum level. The ratio of the lengths signifies that if the absorption of the photons is to take place at a depth larger than $\mathcal{L}$ from the material surface, the probability of photoelectrons reaching the surface with enough energy to escape from the surface will be diminished. Therefore, for a photocathode to posses high QE, it is important that its α_{pe}/α and $\mathcal{P}_E$ be large and $\ell_\alpha/\mathcal{L}$ small. Detailed theoretical treatments and corroborative experiments validating the TSM can be found in references [64], [65] and [71].

Usually, more photoelectrons are generated internally than what is observed outside the material as a photocurrent. For a given material the externally measured photocurrent depends entirely on the value of $\mathcal{P}_{\mathrm{E}}$, which is governed by the surface conditions of the material. In relevance to accelerator-photoelectron sources, QE usually refers to the 'external' QE which is quantified by the measured photocurrent, I_{P}, and is a function of the incident photon wavelength, λ. For an incident laser power, P_{L}, the absolute QE is given by the equation

$$QE(\lambda) = \left| \frac{hc_0 I_{\mathrm{P}}}{P_{\mathrm{L}} \lambda e} \right| \times 100\% \quad , \tag{3.3}$$

where h is Planck's constant, c_0 is the speed of light in vacuum and e is the elementary charge. Instead of percentile values, QE is also often expressed in $\mu\mathrm{A\,mW^{-1}}$ for practical purposes. The reflectance, $R(\lambda)$, of the emitting surface can be included in equation (3.3) to represent the true efficiency as $QE' = QE/(1-R)$.

Gallium Arsenide (GaAs) is perhaps the most researched group III-V *direct* band-gap semiconductor photocathode material. Direct band-gap materials have their CBM and VBM at the same value of crystal momentum, $\boldsymbol{k}$, which restricts transitions between valance and conduction bands to vertical in the momentum space, and gives rise to high values for α near the band-edge. The band-gap energy of GaAs at room temperature is about 1.42 eV corresponding to a wavelength of about 870 nm. Variations in the direct band-gap energy of GaAs with respect to crystal temperature is calculated using the formula [72]

$$\mathcal{E}_{\mathrm{G}} = 1.519 - \frac{5.405 \times 10^{-4} T^2}{T + 204} \quad \mathrm{eV}, \tag{3.4}$$

where T is the temperature in Kelvin and the value 1.519 eV is the projected band-gap energy of GaAs at absolute zero.

The band structure of GaAs is well established [73, 74]. Figure 3.2 shows the GaAs band structure in the vicinity of the conduction band and the valance band edges. At the symmetry Γ-points ($\boldsymbol{k}_x = \boldsymbol{k}_y = \boldsymbol{k}_z = 0$) where CBM and VBM are located, the conduction band is denoted by Γ_6. The valance band in the momentum space Γ_8 contains the heavy hole ($\Gamma_{8\mathrm{hh}}$) and the light hole ($\Gamma_{8\mathrm{lh}}$) degenerate-bands, separated by $\Delta_{\mathrm{SO}} = 340$ meV from the spin-orbit split-off band Γ_7 [75]. When photons of energy $\mathcal{E}_{\mathrm{G}} < h\nu < \mathcal{E}_{\mathrm{G}} + \Delta_{\mathrm{SO}}$ are absorbed, transitions occur from $\Gamma_{8\mathrm{hh}}$ and $\Gamma_{8\mathrm{lh}}$ to Γ_6. If the photon energy is such that $h\nu \geq \mathcal{E}_{\mathrm{G}} + \Delta_{\mathrm{SO}}$, transitions from Γ_7 will also take place. A detailed review of the semiconducting and other relevant properties

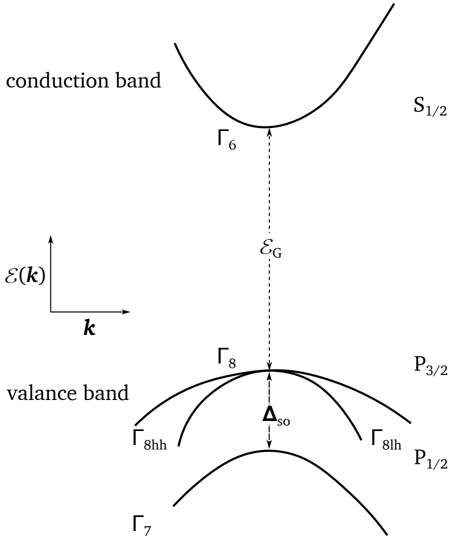

Figure 3.2: The band structure of GaAs near the band edges. Γ_6, Γ_{8lh} and Γ_{8hh} represent the conduction band, the light-hole valance band and the heavy-hole valance band, respectively. At $\boldsymbol{k} = 0$, CBM and VBM are separated by the band-gap energy $\mathcal{E}_G$. The spin-orbit split-off band Γ_7 of s-symmetry is separated from heavy- and light-hole bands by an energy Δ_{SO}. The conduction band at Γ_6 has s-symmetry and the degenerate Γ_8 bands have p-symmetry.

		Reference
Crystal structure	zincblende	[77]
Cleavage plane	[110]	
Band-gap, $\mathcal{E}_G(300\,\mathrm{K})$	1.422 eV	
Electron affinity, $\mathcal{E}_A$	4.01 eV	
Melting point, T_M	$(1513 \pm 1)\,\mathrm{K}$	[78]
Preferential evaporation point, $T_{co}(100)$	657–663 °C	[79, 80]
Spin-orbit split-off energy, Δ_{SO}	340 meV	[75]
Reflectivity, $R(\lambda)$	30–60%	[81]

Table 3.1: Properties of bulk-GaAs crystals relevant to their use as photocathodes.

of GaAs is given in the reference [76]. Some of the important crystal properties of GaAs are summarized in table 3.1.

Another advantage of group III-V semiconductors is the tunable nature of their spectral sensitivity through alloying with elements from the same groups [82]. For example, a continuous addition of In to GaAs continuously decreases the band-gap of the ternary mixture $\mathrm{Ga}_x\mathrm{In}_{1-x}\mathrm{As}$ from 1.4 to 0.36 eV [83]. Alloyed III-V materials are of particular interest in wide spectral range devices as well as in multilayer structures of III-V semiconductors discussed in section 3.1, which are used for highly-polarized electron beam production. The advantages and disadvantages of alloying GaAs to exploit the band-gap tuning can be found in references [70] and [84].

3.1 Polarized electron emission

In an unpolarized electron bunch, the electron spin vectors, $\vec{s}$, are randomly oriented and cancel out each other to result in a total spin, $\vec{S}$, equal to zero. Conversely, if an ensemble of electrons has a direction for which the opposing spin states are not equally populated, it is said to be polarized. The degree of polarization, P, of the spin-polarized ensemble can be written as [85]

$$P = \left| \frac{N_\uparrow + N_\downarrow}{N_\uparrow - N_\downarrow} \right| \times 100\% \quad , \tag{3.5}$$

where $N_{\uparrow/\downarrow}$ is the number of electrons with spin parallel ($s_z = +\frac{1}{2}\hbar$) or anti-parallel ($s_z = -\frac{1}{2}\hbar$) to a chosen quantization direction $\hat{z}$.

Spin-polarized electron ensembles can be generated in many ways, for instance, through β-decay from radioactive sources, Mott scattering, photo-ionization or Fano-effect in alkali atoms [86]. However, these methods cannot produce the intense beams of polarized electrons required by modern experiments at collider facilities. A polarized electron source utilizing bulk-GaAs which satisfied the high-current requirement was first proposed by E. L. Garwin and D. T. Pierce in 1974 [87], based on band-to-band optical pumping of spin-polarized conduction electrons in semiconductors [88–90]. Since the late 70's this type of sources are preferably used at accelerators due to their simplicity in construction as well as easiness of operation.

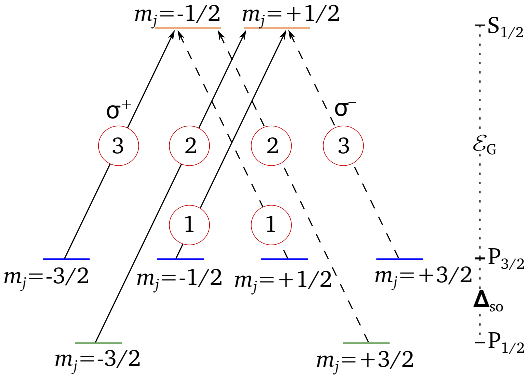

Figure 3.3: Digram depicting orbital level transitions for photoexcitation in bulk-GaAs. The arrows labeled with $\sigma^{\pm}$ represent incident photons with right or left circular polarization, respectively. The numbers in circles correspond to the relative transition probabilities between the sub-levels.

Theoretically, emission of electrons with a degree of polarization up to 50% is possible from bulk-GaAs due to the spin-orbit splitting of otherwise degenerate valance bands. The spin-orbit interaction causes the six-fold degenerate p-band at Γ_8 to split into a four-fold degenerate $P_{3/2}$ level, and a two-fold degenerate $P_{1/2}$ level which lies 340 meV lower. Specific spins can be overpopulated as a result of the optical selection rules and differing transition probabilities for magnetic transitions. Orbital level transitions for photoexcitation in GaAs are shown in figure 3.3. Optical pumping with circularly polarized light at the band-gap minimum can exclusively excite electrons from the $J = 3/2$ valance band, so long as the excitation of electrons in the $J = 1/2$ split-off band is not energetically possible. The selection rules for inter-band absorption are the same as for an atomic transition between levels with angular momenta 3/2 and 1/2, i.e., only direct band transitions obeying $\Delta m_j = \pm 1$ are allowed upon absorption of circularly polarized light of helicity $\sigma^{\pm}$. Here, σ^{+} represents the angular momentum of photons in the direction of propagation and σ^{-}, opposite to it.

The relative strengths of these transitions are determined by the corresponding Clebsch-Gordon coefficients. If σ^{+} light of energy $h\nu < \mathcal{E}_G + \Delta_{SO}$ is used to excite electrons, only two transitions are possible: $|{}^3\!/_2, -{}^3\!/_2\rangle \rightarrow |{}^1\!/_2, -{}^1\!/_2\rangle$ and $|{}^3\!/_2, -{}^1\!/_2\rangle \rightarrow |{}^1\!/_2, {}^1\!/_2\rangle$. The probabilities for these transitions are in the ratio 3:1, giving rise to a maximum net polarization of

$$P = \frac{3-1}{3+1} \Rightarrow 50\% \quad . \tag{3.6}$$

It is possible to reverse the polarization direction simply by switching the helicity of the impinging photon. The theoretical value of 50% polarization is not usually achieved in a laboratory due to depolarization of the excited electrons prominently during (i) thermalization process, (ii) transport to the band-bending region (BBR), (iii) crossing of the heavily p-doped BBR and (iv) their escape into the vacuum across the NEA layer surface barrier [91]. The resulting polarization, P, of the emitted electrons can be expressed as a product of the depolarization probabilities associated with each of these steps as

$$P = P_0 \cdot R_{\mathrm{th}} \cdot R_{\mathrm{tr}} \cdot R_{\mathrm{BBR}} \cdot R_{\mathrm{emi}} \quad , \tag{3.7}$$

where P_0 is the electron polarization in the conduction band at the moment of excitation. Typically a polarization loss of 6–8% is inherent to emission from GaAs. Photoemission from bulk-GaAs typically yields polarization of about 30% at room temperature and 35–40% at or below liquid nitrogen temperature, while polarization close to 50% have also been observed with very thin ($\leq 100\,\mathrm{nm}$) GaAs epitaxial cathodes [92].

3.1.1 Lattice-strained photocathodes

Removing the degeneracy in the $\Gamma_{8\mathrm{hh}}$ and $\Gamma_{8\mathrm{lh}}$ bands (see figure 3.2) can effectively remove the maximum polarization limit on photoemission from GaAs. First attempts to fulfil this condition included applying uni-axial stress to GaAs [93] and engineering of semiconductors to incorporate an internal-strain through lattice-mismatching [94]. Research centred around the latter soon yielded electron polarization well above 50%, as was reported by several groups using epitaxially grown strained-layer (SL) semiconductor structures such as GaAs/InGaAs and GaAs/GaAsP [95–98]. Optical pumping of a semiconductor which has its $\Gamma_{8\mathrm{hh}}$ and $\Gamma_{8\mathrm{lh}}$ separated by an energy $\Delta\mathcal{E}_{\mathrm{strain}}$ with a circularly polarized light of energy $h\nu < \mathcal{E}_{\mathrm{G}} + \Delta\mathcal{E}_{\mathrm{strain}}$ can excite electrons exclusively from $m_j = \pm 3/2$ levels. Figure 3.4 represents the photoexcitation scheme of such an SL-GaAs crystal. Correct choice of the polarization and energy of the excitation light can result in 100% polarized electron emission, in theory.

The strain in the SL-GaAs is introduced by epitaxially growing an *active* layer of GaAs on a lattice-mismatched buffer layer, for example, $\mathrm{GaAs}_{1-x}\mathrm{P}_x$. The strain induced is proportional to the difference in the lattice constants of the active and buffer layers, which in turn is proportional to the phosphorus fraction in the buffer layer. The symmetry of GaAs crystal is reduced from cubic to tetragonal due to the

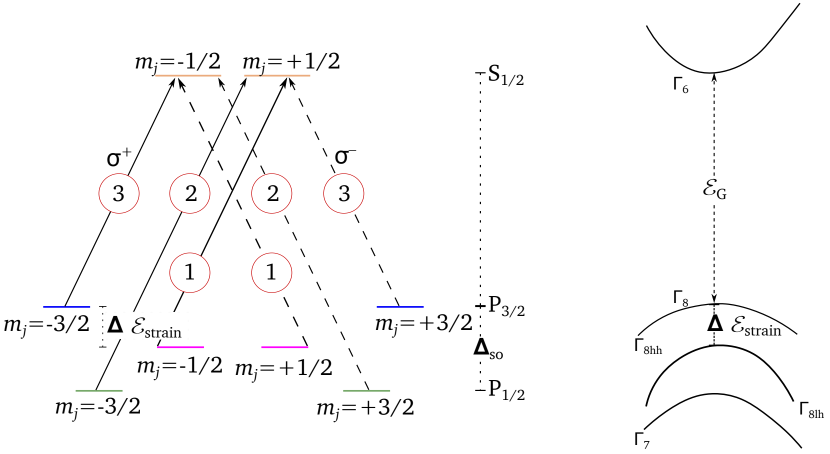

Figure 3.4: Band diagram of a strained-GaAs crystal. With the degeneracy at the valance band removed by $\Delta\mathcal{E}_{\text{strain}}$, electrons from $m_j = \pm 3/2$ can be selectively excited to produce 100% polarized electrons in the conduction band.

strain so that the degeneracy between light- and heavy-hole valence bands at the center of the Brillouin zone is lifted. Strained GaAs photocathodes have been used to produce highly polarized electron beams with degrees of polarization amounting to 70–85% at Nagoya University [99], SLAC [14] and MAMI [100]. Although SL-GaAs cathodes produce highly polarized beams, their *QE* is very low (≤0.3%) due to a limit on the thickness of the active layer, which should be kept below a critical value, t_c, in order to preserve the strain as well as to reduce depolarization. With such a technical limitation in place, an increment of *QE* of a strained layer cathode could only be achieved at the expense of the degree of polarization.

The issue of critical thickness was overcome by the introduction of strained-superlattice (SSL) photocathodes [101,102], in which quantum-well structures are formed by strained active layers and relaxed potential barriers. Using molecular beam epitaxy (MBE) techniques, every separate strained layer of a few nanometre thickness can be grown thinner than t_c and at the same time the total thickness of the periodic structure can exceed t_c by several times to obtain high *QE*. The superlattice periods are usually *p*-doped to a low value $\sim 5 \times 10^{17}\,\text{cm}^{-3}$ to suppress electron spin-relaxation, while the top layer of the structure is heavily *p*-doped to not less than $5 \times 10^{19}\,\text{cm}^{-3}$ in order to achieve a high-quality NEA surface and to overcome the surface charge limit (SCL) [55]. Nowadays, SSL photocathodes are regularly used at polarized electron sources worldwide. GaAs/GaAsP (12 pairs of 3 nm each) superlattice grown by metal-oxide chemical vapour deposition (MOCVD) at Nagoya University had been able to deliver a beam polarization of 92% at *QE* of 0.5% [103]. A peak polarization of 85% at 1% *QE* has been reported by SLAC by using an MBE grown SSL-GaAs/GaAsP (14 pairs of 4 nm and 3 nm each) [104].

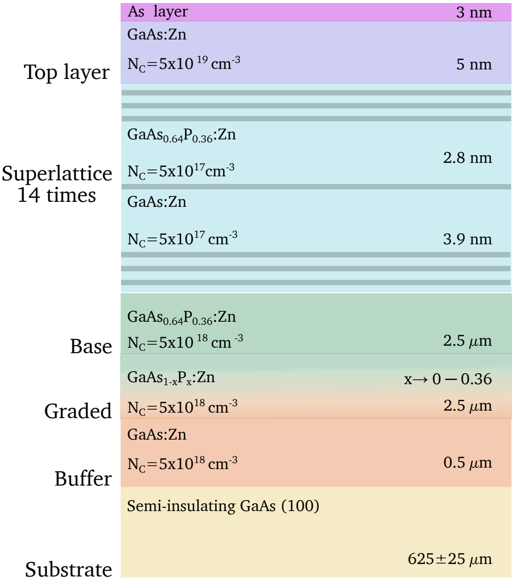

Figure 3.5: Structure definition of the photocathode sample EB96. N_C denotes the Zn-doping density.

An attempt has been made to grow a single wafer of GaAs/GaAs$_{0.64}$P$_{0.36}$ for the future operation of Photo-CATCH with pulsed spin-polarized electron beams. The design parameters such as the quantum well thickness and doping profiles have been kept identical to the sample B702 that produced electron bunches with a degree of polarization of 86% at 0.3% *QE* at SPIN. This sample had its superlattice period repeated 14 times and the layer thicknesses for GaAs and GaAs$_{0.64}$P$_{0.36}$ about 3 nm and 4 nm, respectively [53]. $\Delta\mathcal{E}_{\text{strain}}$ of > 80 meV can be expected for a phosphorus fraction of $x = 30 - 40\%$, which corresponds to a t_c of 5 to 10 nm [105].

The structure of the test sample EB96[1] is shown in figure 3.5. The amorphous arsenic cap-layer is included to protect the wafer surface from contamination and oxidation during its transport and storage. This layer is easily removed by annealing the sample surface to $<400\,^{\circ}\mathrm{C}$, prior to the NEA activation.

Scanning Transmission Electron Microscopy (STEM) analysis[2] revealed that the actual EB96-wafer did not conform to the original dimensional specifications. Thickness variations as large as $+1$ nm was observed in many of the superlattice periods. Nevertheless, none of the superlattice layers could be seen to exceed the critical thickness of 5 nm corresponding to phosphorus fraction of 0.358 as measured by x-ray diffraction (XRD). Although strain relaxation may not occur below t_c, it is possible that the increased thickness of the barrier layers considerably reduce vertical electron transport through the structure in addition to enhancing depolarization effects. The characteristics of the MBE-grown strained-superlattice sample EB96 are visible in the STEM images given in figure 3.6.

3.2 High quantum efficiency

Understanding of the mechanism of photoemission in semiconductors opened the path to modification of material properties in the interest of improving their performance. It is apparent that a reduction of the electron affinity of the material could greatly enhance the escape probability of the photoelectrons. Rearranging the equation (3.1) gives

$$\mathcal{E}_\mathrm{A} = e\phi + \delta\mathcal{E}_\mathrm{VF} - \mathcal{E}_\mathrm{G} \quad , \tag{3.8}$$

which clearly indicates that any reduction of $\mathcal{E}_\mathrm{A}$ must proceed through the manipulation of $e\phi$ and $\delta\mathcal{E}_\mathrm{VF}$. Analogous to its action on metallic surfaces, adsorption of cesium (Cs) can reduce $e\phi$ of a semiconductor through dipole layer formation at the surface [106]. Repositioning the Fermi level in a semiconductor requires modification of its electronic structure through introduction of impurities into the material.

The necessity of doping of semiconductors with the intention of reducing the electron affinity has been first pointed out by W. E. Spicer [62]. Doping of a semiconductor causes rearrangement of $\mathcal{E}_\mathrm{F}$ with respect to the position of that in an un-doped crystal (figure 3.7a). *p*-doping moves $\mathcal{E}_\mathrm{F}$ close to the valance band, while

---

[1] Grown by UniversityWafer Inc., Massachusetts, USA.

[2] Institut für Angewandte Geowissenschaften, TU Darmstadt

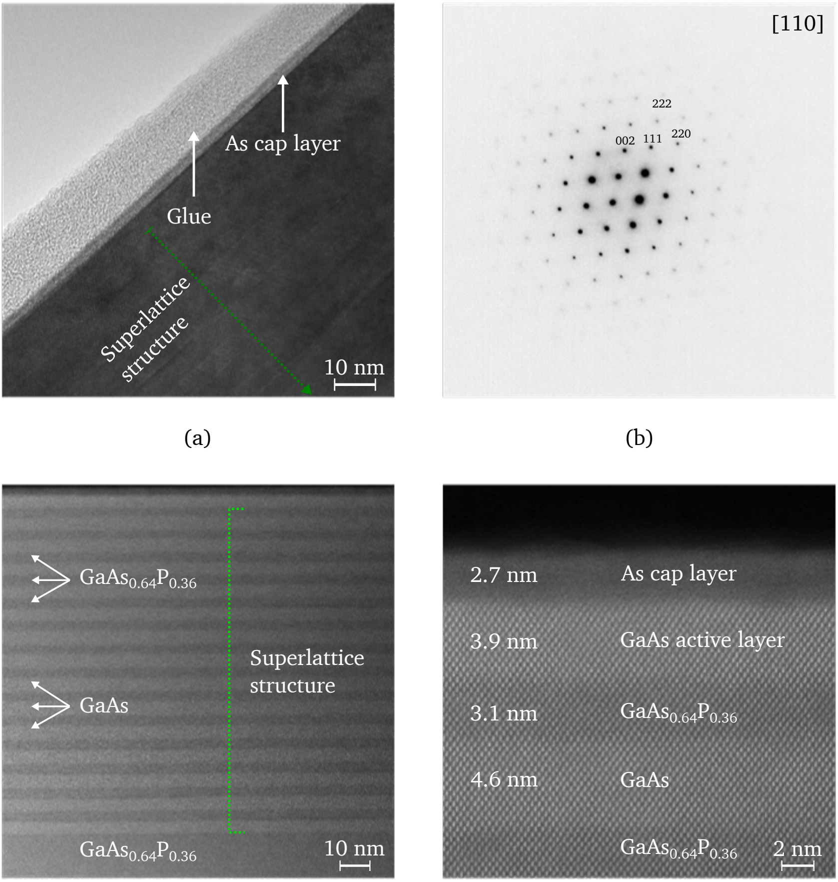

(a) (b) (c) (d)

Figure 3.6: Microscopic images of EB96. **(a)** TEM bright-field image showing top layers and part of the superlattice structure. **(b)** Selected Area Electron Diffraction pattern of the sample. **(c)** STEM dark-field of the superlattice layers. Seven pairs of lightly *p*-doped GaAsP (dark) and GaAs (light), an active layer of heavily *p*-doped GaAs (light), and the As cap layer (dark) can be identified. **(d)** High-resolution image of the top five layers showing the thicknesses of the individual layers.

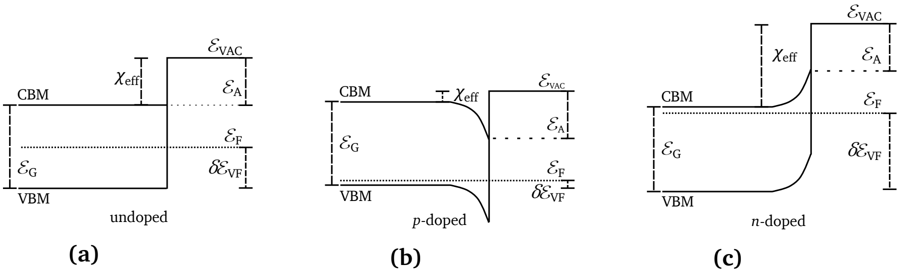

Figure 3.7: Band-deformation at the vacuum interface of a semiconductor due to high-density doping. Figures show band structures of a **(a)** pure semiconductor, **(b)** p-doped material and **(c)** n-doped material. It can be seen that p-doping bends the bands at the surface in a fashion that favors lowering of χ_{eff}, whereas n-doping elevates it.

n-doping moves it closer to the conduction band (figures 3.7b and 3.7c). Band bending occurs due to the pinning of the Fermi-level at the surface, in order that it is continuous from the bulk of the material to the surface [63, 107, 108]. It can be seen in figure 3.7 that, as $\delta\mathcal{E}_{\text{F}}$ moves within the bulk of the material, the value of $\delta\mathcal{E}_{\text{VF}}$ is modified. At very high acceptor concentrations, $\mathcal{E}_{\text{F}}$ can be made to coincide with VBM to attain $\delta\mathcal{E}_{\text{VF}} \approx 0$. It is important to notice that, while $\mathcal{E}_{\text{A}}$ at the semiconductor surface remains unchanged by doping, a variation is apparent for an *effective* value of $\mathcal{E}_{\text{A}}$ as encountered by the conduction-band electrons in the bulk of the material. Accordingly, an effective electron affinity, χ_{eff}, can be defined as

$$\chi_{\text{eff}} = \mathcal{E}_{\text{VAC}} - \mathcal{E}_{\text{G}} \quad , \tag{3.9}$$

which quantifies the energy difference between CBM *in the bulk* of the material and the vacuum level *at the surface*. With a low χ_{eff}, photoelectrons excited into the conduction band in the bulk of the material do not require as much kinetic energy as in an intrinsic semiconductor to make their way into the vacuum.

3.2.1 Negative electron affinity

If the work function is lowered sufficiently that the vacuum level at the surface lies below the bottom of the conduction band in the bulk of the material, $\chi_{\text{eff}} < 0$ can be achieved. This condition is known as negative *effective* electron affinity state (NEA). J. Scheer and J. van. Laar have observed that adsorption of Cs on p-GaAs (110) reduces its χ_{eff} from 4.5 eV to 0.0 eV [109]. Later it was found that application of

Cs and O_2 on a cesiated semiconductor gave an even lower χ_{eff} and higher QE, realizing the first NEA photocathodes [110, 111]. NEA cathodes are fundamentally different from the conventional PEA emitters, chiefly because of their $\alpha_{\text{PE}}/\alpha$ approaching unity and $\mathcal{L}$ increased by about three orders of magnitude, setting $\ell_\alpha/\mathcal{L}<1$. The QE of such cathodes near the threshold of emission is much higher due to the fact that electrons which are inelastically scattered could escape even after thermalizing into the bottom of the conduction band [112]. Values of $\mathcal{P}_{\text{E}}$ approaching 40% has been observed for GaAs:(Cs,O_2) photocathodes and could be considered to be independent of $h\nu$ to a good approximation near $\mathcal{E}_{\text{G}}$, which defines the threshold for emission in an NEA photocathode [113].

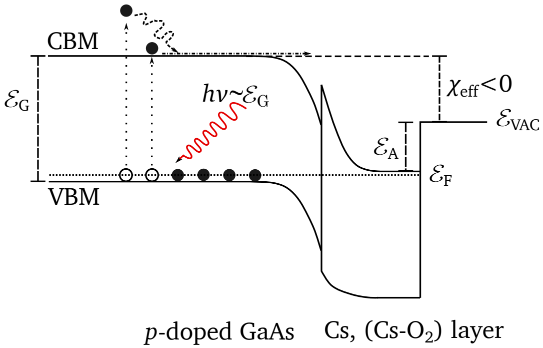

Figure 3.8: Energy-band diagram of an NEA-GaAs photocathode. Negative value of the effective electron affinity resulting from the application of a Cs-O_2 layer allows thermalized electrons in the conduction band to escape into the vacuum.

A simplified illustration of the effects of NEA formation on the band structure of a semiconductor photocathode can be seen in figure 3.8. $\mathcal{P}_{\text{E}}$ is no more determined by the potential barrier at the surface and the escape depth of hot electrons, but by the diffusion length of electrons thermalized into the bulk conduction band minimum where the dominant scattering is of inelastic e-phonon nature. In conventional cathodes, the excited electrons lose enough of their energy via $e-e$ scattering within $\sim 10^{-12}$ s which corresponds to $\mathcal{L}$ about 300 Å. The lifetime of the excited electrons in NEA cathodes is of the order of 10^{-9} s and consequently, escape lengths of over 10 μm can be realized [114]. The technique of producing NEA photocathodes of group III-V materials is well established. The deposition of Cs and O_2 on the semiconductor surface to produce high-efficiency photocathodes is commonly known as NEA *activation* process.

NEA state is activated by depositing an alkali-metal–oxidant combination on a freshly cleaved or *in-situ* cleaned semiconductor surface under ultra-high vacuum ($<1 \times 10^{-10}$ mbar) conditions. The photoresponse from the cathode is monitored throughout the activation process by measuring the photocurrent (I_p) produced using light of known parameters. The alkali of choice is Cs because of its lowest workfunction among the alkali-metals, and (O_2) or Nitrogen tri-Fluoride (NF_3) are preferred as oxidants due to their high electro-negativities. Several 'styles' of activation methods are in practice of which the most straight forward, ergo popular, is the *Co-deposition* (Co-De) method. The typical shape of an activation diagram resulting from the Co-De procedure is given in figure 3.9a. Co-De begins with Cs deposition on the semiconductor surface until the observed I_p peaks and drops to about 75% of the peak. At this point, the oxidant is co-deposited by flowing an appropriate quantity of O_2 or NF_3 into the vacuum chamber, which continues till I_p reached its second peak and enters a plateau. The activation ends with a little over-cesiation of the surface as a common practice. Depending on the flux of Cs and the oxidant and their sticking probabilities on the sample surface, the activation process can take from 15 to 120 min to complete. Co-deposition is the activation method that has been mainly practised in this work to prepare GaAs:(Cs,O_2) photocathodes of moderate, but reproducible, *QE*s.

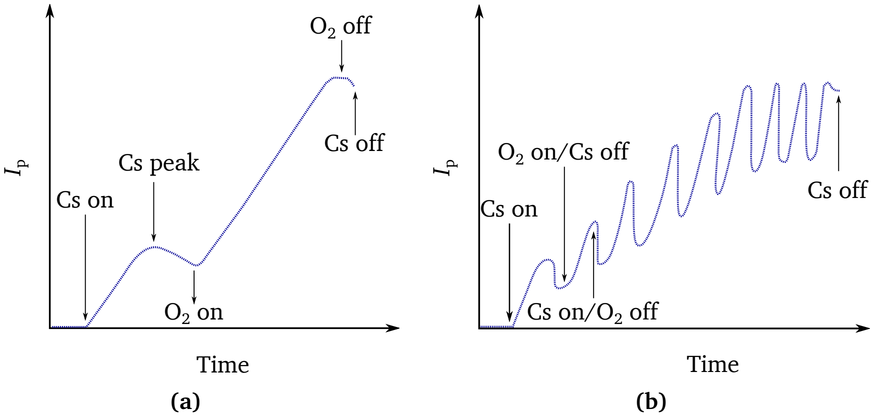

Figure 3.9: Diagram showing the typical time evolution of photocurrent during **(a)** Co-De activation and **(b)** Yo-Yo activation procedures. Arrows point to the times at which oxygen and cesium flow are regulated.

An alternative recipe for preparing NEA surfaces is the *Yo-Yo* procedure [12, 115]. In this method, Cs and O_2/NF_3 are alternately applied beyond the first Cs-response peak. In each turn of Cs application, the photocurrent reduces to about 50% of its previous maximum. With each turn of the admission of O_2 the current rises back to a new peak. This cycle is repeated until no significant improvement of I_p is evident. The behaviour of I_p during a Yo-Yo type activation resembles figure 3.9b. A modified Yo-Yo method, dubbed *Nagoya-Activation* (Na-Ac), differs in that the application of Cs is kept up until I_p drops to zero in each turn [55]. In this activation method, more Cs is deposited on the cathode surface than in a Yo-Yo. Photoresponse in a typical Na-Ac activation follows a curve similar to the one shown in figure 3.10. Bulk-photocathodes of about 27% QE at 650 nm have been obtained using yet another activation practice called the *two-stage* activation [116]. It proceeds by first activating the cathode to its peak QE using one of the methods mentioned above and then annealing the cathode at ∼510 °C for 30 to 60 min, cooling down to room temperature, and activating it again to reach a much higher QE. Although there are disagreements on the optimum annealing temperature between the activations, an increment of 15-30% on the achievable QE in comparison to the other single-stage methods have been regularly observed [117–119]

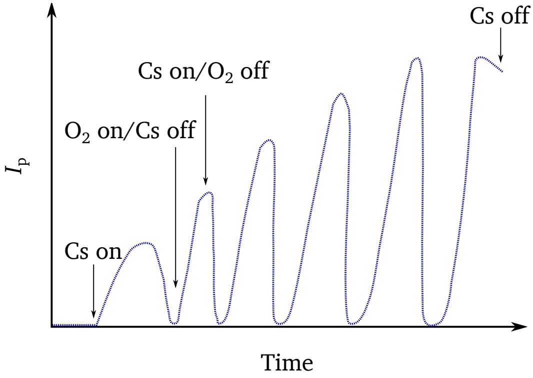

Figure 3.10: Photocurrent evolution during the Nagoya-activation procedure.

As a complete physical description of the activation layer is still lacking, the NEA activation process remains largely empirical. There are basically two schools of thought on the action of the (Cs,O_2) layer at the surface, which are, however, limited to their domains of validity due to fundamental differences in their approaches [120–122]. The available models are (i) the heterojunction (HJ) model and (ii) the dipole-layer (DL) model. The HJ model assumes bulk properties of Cs_2O nature to be responsible for the NEA formation and postulates a heterojunction formation between the cesium covered p-GaAs and the n-type semiconducting Cs_2O. According to the HJ model, the workfunction of the Cs_2O due to band-bending at the interface is given by [123]

$$\phi_{\mathrm{Cs_2O}} = \phi_0 + (t_\mathrm{L} - L_\mathrm{BB})^2 (N_\mathrm{d} e^2 \epsilon) \quad , \tag{3.10}$$

where ϕ_0 is the workfunction of bulk Cs_2O, t_L is the thickness of the layer, L_BB is the band bending distance, N_d is the density of the ionized donors in the band bending region and ϵ is the dielectric constant. The HJ model holds correct when many monolayers[3] are present in the NEA layer, thick enough to form a solid-solid heterojunction [123–126]. However, many studies argue that not more than one monolayer of Cs and one monolayer of Cs_2O are necessarily adsorbed on the surface of an NEA photocathode, which is insufficient for a heterojunction formation. This indicated that a (double) dipole-layer formation must be defining the surface barrier properties of a thin NEA layer rather than a heterojunction at the surface [127–129]. The DL model attributes the lowering of the surface potential to the creation of dipole layers of the form GaAs–O–[Cs]:[Cs^+]–O^{-2}–Cs^+ at the surface [130]. It has also been reported that the structure of the NEA layer undergoes a transformation after the first exposure of Cs [131, 132]. Photocathodes within the domains of validity for both models have been created with reasonably high *QE* [133]. The borders of these domains have been examined and demarcated by V. V. Bakin *et. al.* [116]. Structural studies on the surface layer resulting from different types of activation procedures are discussed in reference [134]. A better fundamental understanding of the NEA layer can lead to the development of novel activation methods and the enhancement of the escape probability of photoelectrons at the surface.

NF_3 and O_2 are interchangeably used as the oxidant species in NEA activation process. Any advantage in terms of the resulting *QE* is inconclusive as mixed results claiming an improvement [13] and no significant improvement [135] of *QE* with NF_3 activation over the O_2 activation are often reported. But, an enhancement of chemical immunity against deteriorative oxidation of the NEA layer appears to be unambiguous in the case of (Cs, NF_3) activation [26, 136]. The quality of the NEA surface, and thus the final *QE* of the prepared cathode, depends entirely on the surface cleanliness prior to its deposition, the purity of Cs and O_2/NF_3 sources, and the ambient vacuum conditions. G. A. Mulhollan et. al. reported on improved chemical

---

[3] 1 monolayer = 4×10^{14} atoms cm^{-2}

immunity of NEA layer against oxidation as well as an increase in the final *QE* by incorporation of Lithium (Li) into the activation recipe. [137]. The nature of the (Cs, Li, NF_3) activation layer has been investigated by Y. Sun et al. [27]. Observations from p-GaAs:(Cs, Li, O_2) photocathode preparation studies are discussed in section 5.2 of this thesis.

3.2.2 Surface cleaning

Contaminants on a GaAs photocathode belong mainly to three categories: metallic impurities adsorbed during growth of the sample wafer - produced mostly by ionizing elements in the vacuum system, other semiconductor impurities of similar band-gap found in III-V element evaporators, and materials of insulating nature consisting of native oxides or carbides on the surface developed during transport and long term storage. Impurities present on the cathode surface adversely affect the photoemission by

- occupying the surface sites and obstructing Cs from making a strong bond to GaAs and thereby preventing the reduction of $\mathcal{E}_{\mathrm{A}}$,
- introducing a surface-potential that leads to a reduction of $\mathcal{P}_{\mathrm{E}}$,
- promoting $e-e$ interaction and phonon-type scattering within the foreign compound thus reducing the energy of the conduction electrons.

The usage of high purity group III-V constituents and observing extreme high vacuum practices can prevent contamination of the semiconductor crystals during their growth, which limits the main contamination phases to their transport, storage and handling in a laboratory environment. An atomically clean surface of the photocathode is necessary in order to produce high-quality NEA photocathodes. Even a monolayer of surface oxides or carbides suffices to significantly reduce the performance of the cathodes.

Commonly the oxidisation of GaAs takes place first on the arsenic sites according to the chemical reaction [138]

$$4\mathrm{GaAs} + 3\mathrm{O}_2 \xrightarrow[\text{fast}]{\text{room temp}} 2\mathrm{As}_2\mathrm{O}_3 + 4\mathrm{Ga} \quad . \tag{3.11}$$

Even though easily desorbed at low temperatures, the formation of As_2O_3 has to be prevented because of their oxygen transferability into the bulk of the material forming more stable oxides. This process has been attributed to a spatially inhomogeneous bulk reaction between the GaAs surface and the arsenic oxides proceeding through the reaction [139]

$$2\mathrm{GaAs(bulk)} + \mathrm{As_2O_3} \xrightarrow[\text{slow}]{\text{temp dependant}} 4\mathrm{As} + \mathrm{Ga_2O_3} \quad , \tag{3.12}$$

and is present irrespective of the conditions in which the sample is stored. This scenario is called *ageing* of GaAs. Since this reaction is temperature dependent, storing the samples at low temperature can significantly slowdown the ageing process. More fittingly, it can be eliminated altogether if As_2O_3 is removed prior to sample storage in vacuum or an inert gas environment.

A contaminant which is generally present on GaAs surface is carbon (C) and has a predictable effect on the *QE* because the interfacial barrier of the system GaAs-C-Cs_2O is too high to allow the low-energy electrons to pass through [140]. Semiconductor surfaces are routinely cleaned in laboratories by wet-chemical methods. The samples are repeatedly washed in solutions of acids and bases and in de-ionized water. Mostly, etching agents such as HCl, H_2SO_4, H_2O_2 and NaOH are used [12,141]. A low temperature (∼400 °C) heat-cleaning of the sample in a vacuum chamber following the chemical cleaning has been found to produce oxide-free semiconductor surfaces [131]. However, the chemical cleaning method is not suitable for cleaning strained-layer or superlattice photocathodes, such as the ones described in section 3.1.1, since the thin surface layers responsible for high *P* and *QE* are susceptible to destruction due to material loss during the etching process.

The simplest and widespread cleaning technique is high-temperature annealing of the sample. As the sample is annealed close to its dissociation temperature, the surface oxides are dissociated and/or desorbed from the surface. Heat cleaning is simple and efficient in most of the cases but comes with several disadvantages. It is known that the cleanliness of a heat cleaned surface is proportional to cleaning temperature [142–144] which is limited by the in-congruent evaporation point, T_{co}, of the crystal. Close to T_{co}, preferential evaporation starts where the rate of desorption of the group V component exceeds that of the group III component. For GaAs it is about 650 °C, and only additional flux of group V material can compensate for the loss at temperatures above 580 °C. During annealing, the Ga^{3+} oxides are removed through thermal decomposition into volatile oxides in which the bulk-GaAs from the substrate is consumed according to [145]

$$\mathrm{Ga_2O_3} + 4\mathrm{GaAs(bulk)} \xrightarrow{>580\,^\circ\mathrm{C}} 3\mathrm{Ga_2O} + 2\mathrm{As_2(As_4)} \quad . \tag{3.13}$$

This reaction is inhomogeneous in nature and is directly responsible for the roughening and pitting of the GaAs surface, which is highly undesirable for their operation as photocathodes. Moreover, annealing could accelerate the production of Ga_2O_3 by promoting the reaction given in equation (3.12). Because of the high diffusion coefficient of zinc (Zn) at high heat-cleaning temperatures, the capability of this method of cleaning Zn-doped cathodes is very limited. As the highly doped surface layer is responsible for removing the surface-charge-limit (SCL) effect in high photocurrent operations of high-gradient-doped cathodes, and dopant loss is very undesirable. [146]. Also, it is difficult to remove carbon contaminants by simple heating [140]. In essence, an optimum heating that results in a high quantum efficiency of heavily doped cathodes is a compromise between apparent loss of doping concentration near the surface and the surface cleanliness. Other standard methods for cleaning semiconductor surfaces include, but not limited to, ion-beam bombardment [147] or plasma assisted mechanisms [148] where energetic ions are used to sputter away the contaminants, laser cleaning [149], or direct conversion of Ga_2O_3 into Ga_2O by exposure of the substrate surface to Ga flux [145]. While bombardments with energetic particles and laser pulses induce irreversible physical damage to the sample surface, the last method is impractical in most of the accelerator electron sources.

Cleaning of semiconductor surfaces with atomic-hydrogen (H_1), known as the atomic-hydrogen cleaning (AHC), has been proven to overcome most of the issues associated with the conventional techniques [150, 151]. AHC is widely used in semiconductor manufacturing facilities and has been successfully applied to cleaning of both bulk and strained/superlattice cathodes at accelerator sources [152–155]. H_1 produced by cracking molecular hydrogen (H_2) is highly chemically reactive. By annealing at a moderate temperature under a flux of atomic-hydrogen, stable surface oxides, carbides, and other common contaminants are converted to unstable, volatile compounds and thus are effectively removed by subsequent desorption of the reaction products. The principle of cleaning relies on both temperature dependent and independent processes that proceed through reactions given in the references [156–158], that will briefly be discussed here. The As_2O_x-type oxides reacting with H_1 produces elemental As and H_2O through[4]

$$As_2O_x + 2xH_1 \xrightarrow{\text{room temp}} As_2^{\uparrow} + xH_2O^{\uparrow} \quad . \tag{3.14}$$

Ga^{3+} oxides are reduced to volatile Ga^{2+} oxides or Ga^{1+} hydroxides according to the reactions

$$Ga_2O_3 + 4H_1 \longrightarrow Ga_2O^{\uparrow} + 2H_2O^{\uparrow} \tag{3.15}$$

---

[4] ↑ indicates that the compound is volatile below 400 °C.

and

$$Ga_2O_3 + 4H_1 \longrightarrow 2GaOH^{\uparrow} + H_2O^{\uparrow} \quad . \tag{3.16}$$

Since the hydroxide is highly unstable, unless evaporated immediately it undergoes the dehydration reaction [159]

$$2GaOH \xrightarrow{\text{room temp}} Ga_2O^{\uparrow} + H_2O^{\uparrow} \quad . \tag{3.17}$$

Ga_2O starts to desorb at 300 °C and is mostly removed via evaporation by keeping the sample at an appropriate temperature. However, the subsidiary reaction

$$Ga_2O + 2H \longrightarrow 2Ga + H_2O^{\uparrow} \tag{3.18}$$

must also exist resulting in a non-stoichiometric surface due to Ga droplets formation. But, around the AHC temperature, additional minor mechanisms may result in removal of most of the excess Ga on the surface preserving the stoichiometry to a good extend through [156]

$$Ga_2O_3 + 4Ga \rightarrow Ga_2O^{\uparrow} + AsH_3^{\uparrow} \quad . \tag{3.19}$$

AsH_3 is desorbed at room temperature. Since the equation (3.14) is a room temperature reaction, a two-step cleaning procedure is suggested for samples with a surface (arsenic) oxide layer of a few nanometer thickness. The easily removable arsenic oxides can be significantly reduced upon irradiation with a molecular hydrogen flux, ϕ_{H_2}, of 100 kL[5] at a moderate temperature and the gallium oxides are removed at 300 °C and ϕ_{H_2} between 100 to 300 kL [160–162]. The first step hinders the formation of Ga oxides produced during the second step of cleaning through equation (3.12), thus reducing the amount of H_1 flux, ϕ_{H_1}[6], required for completing the cleaning. Additionally, heating only to 300 °C avoids thermal desorption of As from GaAs surface. Removal of carbon contaminants from semiconductor surfaces upon H_1 irradiation can take place at room temperature, with the rate of removal increasing with sample temperature. CH_4 is the primary product in the H_1-C reactions and other species such as CO, CO_2, CH_x and C_2H_x groups emanate from secondary processes [163, 164].

AHC performed in optimum conditions can result in the removal of all of the oxides and carbides and completely rejuvenate the photocathode surface. However,

---

[5] Langmuir (L) is the unit of dosage ; 1 L=1.3×10^{-6} mbar s.

[6] $\phi_{H_1} = 2 \times \phi_{H_2} \times \eta$; η is the cracking efficiency of the H_1 source.

prolonged exposure to an H_1 flux can prompt reactions in the clean GaAs substrate via

$$4\mathrm{GaAs} + 12\mathrm{H} \rightarrow 4\mathrm{Ga} + \mathrm{AsH}_3^{\uparrow}, \tag{3.20}$$

which will lead to Ga islands on the sample surface. Although much accepted, doubts around the merits of AHC of heavily doped photocathode samples in terms of dopant passivation and hydrogen migration exist and come regularly under scrutiny. For example M. Baylac *et al*. found that both QE and P of SL and SSL cathodes have degraded after AHC, compared to samples that have undergone only heat cleaning at 580 °C [165]. However, it may not be overlooked that this study used a source based on rf-dissociation of molecular hydrogen to produce the required H_1 beam, which can also produce high energy particles that causes damage to the sample surface. Study done by R. Rahbi et al. suggested dopant-passivation by hydrogen diffusion [166]. Again, the hydrogen rf-plasma source employed for this study could not be entirely free of ions, and may have contributed to both physical and electronic damaging of the surface. This effect was carefully examined by T. Maruyama et. al by performing H_1 cleaning by filtering and not filtering ions from an rf-source. In the low-temperature hydrogen-cleaning experiments performed with gradient doped thin stained layer photocathodes, no surface damage or depolarization effects were observed by even after prolonged exposure to atomic hydrogen when the energetic ions from an rf-resonator source was removed [54]. No acceptor-passivation or loss of stoichiometry was observed in studies carried out by G. R. Bell et al. who have used a source based on thermal-cracking of molecular hydrogen [167]. Similar result has been reported in reference [153]. Annealing at a temperature below 380 °C after AHC, has been found to remove all the adsorbed hydrogen from the sample surface [168].

Compared to other methods, atomic-hydrogen beam produced by cracking of molecular hydrogen at high temperatures is free of energetic ions and neutrals and does not damage the sensitive samples [169]. The source used at Photo-CATCH is a commercially available hydrogen atom beam source (HABS)[7] based on radiative heating of a capillary and subsequent beam formation. Depending on the capillary temperature and feeding pressure, degree of dissociation close to 100% is possible using HABS. This device is highly power efficient as it uses less than 230 W to reach a capillary temperature of 2000 °C. At very low feeding pressures the flow in the hot-capillary is comparable to molecular-regime which results in an angular distribution of the atomic-hydrogen beam narrower than a

---

[7] HABS-40-A-L190D36 | MBE Komponenten GmbH

cosine distribution [170]. Detailed description on the working and characterization of the source can be found in references [171–173]. An identical source has been successfully used by Mainz group to perform multiple cleanings of superlattice photocathodes [155].

3.3 Lifetimes

NEA activated cathodes have a limited operational *lifetime*, the duration up to which an activated cathode provides a satisfactory QE before a rejuvenation of the NEA layer becomes necessary. The QE decay of an NEA activated cathode follows an exponential behavior to a good approximation. The characteristic time constant, τ_{tot}, in the decay equation

$$\frac{\mathrm{d}QE}{\mathrm{d}t} = -\frac{QE_0}{\tau_{\mathrm{tot}}} \quad , \tag{3.21}$$

corresponds to the time required for the QE of the cathode to drop down to $(1/\mathrm{e})^{\mathrm{th}}$ of its initial value, where QE_0 is the initial quantum efficiency of the photocathode. A typical lifetime evolution curve of an NEA activated photocathode is shown in figure 3.11. It is possible to divide the total lifetime degradation into two main categories. First one is the *dark lifetime*, τ_{d}, that is directly related to the vacuum conditions surrounding the photocathode and its temperature. Residual gases present in the vacuum chamber are held responsible for the gradual destruction of NEA layer that is highly chemically active due to its polar nature. Dark lifetime is the 1/e lifetime of the activated cathode under no illumination. It is measured by measuring the photocurrent for a short time in long intervals to eliminate any effect due to a continuous current extraction.

A model for the QE decay during this condition is developed by M. Kuriki et al. [174]. At constant temperature, the degradation due to chemically active gases at pressure p is characterized by a decay constant, $t_{\mathrm{p}} = \tau_0/p$, where τ_0 is the lifetime with a unit pressure. The decay due to thermal desorption has a lifetime, $\tau_{\mathrm{t}} = (1/\nu)\exp^{-E/kT}$, where ν is the rate constant, E is the binding energy of the hypothetical 'NEA molecule', k is the Boltzmann constant, and T is the temperature. The decay of the cathode QE during idle conditions is then the result of these two processes combined, and follows the form

$$QE = QE_0 \exp^{\frac{-t}{\tau_d}} \;\; ; \; \tau_d = \frac{1}{\tau_p} + \frac{1}{\tau_t} \quad . \tag{3.22}$$

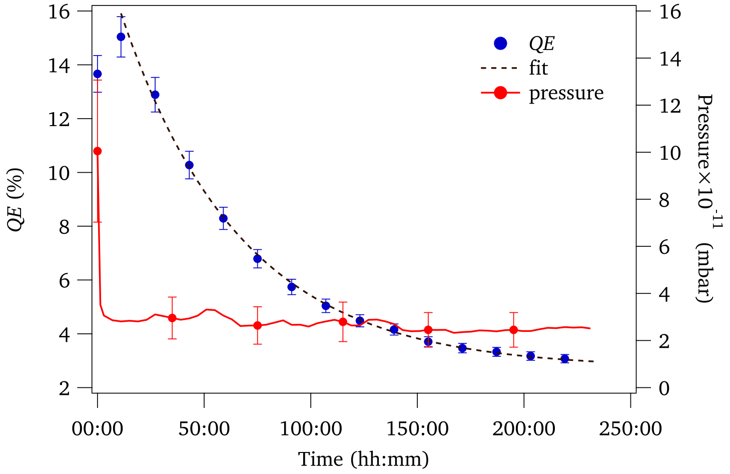

Figure 3.11: Typical lifetime degradation of an activated cathode as observed in the PhotoCATCH activation chamber. From the exponential fit, a lifetime of about (53.0±3.2) hours can be estimated.

This model predicts the effect of temperature to be dominant beyond 50 °C. D. Durek et al. studied the effect of water vapour on the degradation of NEA photocathodes and have estimated a lower limit of the lifetime to be 328 h at an H_2O partial pressure of 1×10^{-12} mbar [24]. T. Wada *et al.* have studied the influence of residual gases on NEA-GaAs lifetime and concluded that chemically active gases such as H_2O, O_2, and CO_2 are detrimental to the photocathodes, while inactive gases such as H_2, N_2, CH_4, Ar, and CO does not influence the lifetime [175]. However, a lesser effect on *QE* by exposure to CO has been reported in a later study, which is reproduced in figure 3.12. Maintaining the best vacuum in the cathode chamber has been proven to improve the dark lifetime considerably. C. K. Sinclair *et al.* achieved a dark lifetime of over 22 000 hours, or about two and a half years, for cathodes with a small area activated to NEA and kept under extreme vacuum conditions with several pumps distributed around close proximity of the cathode [19]. However, not too many facilities around the world can boast such a high investment in vacuum systems. Now that the issue with poor dark lifetimes could be overcome with the betterment of vacuum conditions, the second type of *QE* degradation mechanism preponderates.

The second important degradation mechanism relates to the cathodes operating conditions, and is characterized by the operational lifetime, τ_o. No internal mecha-

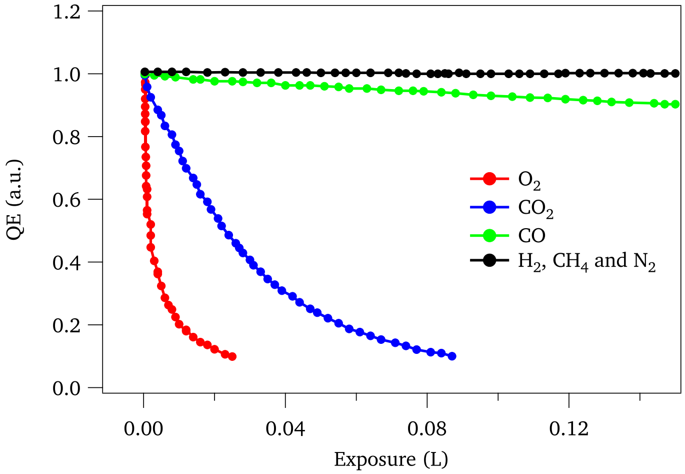

Figure 3.12: Relative *QE* degradation of NEA-GaAs under exposures of active and inactive gases at a partial pressure amounting to 1.5×10^{-10} mbar. Data reproduced from [25].

nism in the photoemission process is known to degrade the *QE* of the photocathode. Therefore the gaseous species in the chamber where high current is extracted from the photocathode is responsible for any degradation in the cathode *QE*. Chemical poisoning of the cathode surface can occur when active gases mentioned before are present in the chamber. More importantly, electrons extracted during the operation can ionize the residual gases. These ions accelerated by the potential at the cathode-electrode (typically 100 to 350 kV) back-bombarding the photocathode at high potential causes severe damage to the NEA surface. This effect was experimentally identified and explained by studies conducted at Mainz [176]. In addition, the field emission due to the high field gradients (4 to 7 MV m^{-1}) can produce small currents that contribute to the degradation. The degraded surface of GaAs can be revived many times by additional Cs deposition, called re-cesiation, although not back to the initial *QE* [177]. Also, the lifetime measured for the original cathode has been found to be much longer than that of the re-cesiated cathode [17]. While degradation caused by H_2O and CO_2 could be recovered to some extent by applying Cs alone, CO_2 has been observed to cause irreversible reduction of *QE* that cannot be repaired with re-cesiation [175]. Prolonging the photocathode life is possible by continuously supplying Cs [178], but evaporation of Cs in the gun chamber can enhance field emission from the electrode surface because of workfunction lowering due to adsorption of Cs atoms.

The contribution of ion-back bombardment is proportional to the current extracted from the cathode. It can be observed that the total charge that can be extracted from an activated cathode at a constant current before its lifetime is limited. This can be expressed as a *charge lifetime*, τ_a, and takes the form

$$\frac{1}{\tau_\mathrm{a}} = \frac{k_\mathrm{A}}{I_\mathrm{P}} \quad , \tag{3.23}$$

where the constant k_A has the dimension of charge and signifies the limit on the total charge that can be withdrawn from a cathode during its lifetime τ_a at an operating current I_P. Although not all these decays happen exponentially, the observed lifetime of a photocathode in operation can be approximated to be the sum of individual degradation lifetimes such that [179],

$$\frac{1}{\tau} = \frac{1}{\tau_\mathrm{d}} + \frac{1}{\tau_\mathrm{o}} + \frac{1}{\tau_a} \quad . \tag{3.24}$$

4 Photo-CATCH

The optimization of cleaning and NEA activation procedures and realization of high dark- and operational-lifetimes of photocathodes are necessary for the successful operation of SPIN both as a source of highly polarized electrons and as an injector of low-emittance unpolarized electron bunches meeting the current and charge requirements of the future energy-recovery linac (ERL) operation of S-DALINAC [180]. Section 2.2 presented the cases for replacing the conventional heat-cleaning of GaAs-based photocathodes with a low-temperature process, and deriving a reproducible activation recipe for the preparation of high QE cathodes. The feasibility study of an inverted-insulator geometry electron-gun (IIGG) with a lift-mechanism used at SPIN electron-gun has also been mentioned. To this end, a standalone facility for *photocathode activation, test, and cleaning using atomic-hydrogen* (Photo-CATCH) has been designed and set-up in a dedicated laboratory. The main objectives of Photo-CATCH system are:

- photocathode research independent from SPIN
- H_1 assisted cleaning of photocathodes
- improvement of NEA activation technique
- studies on wavelength dependency of cathode parameters
- test of inverted-insulator geometry electron-gun
- diagnosis of and experiments with low-energy spin-polarized electrons

The design of Photo-CATCH resembles SPIN and its beamline for the most part, except for the chamber for H_1 cleaning, the IIGG and the double-scattering Mott-polarimeter. Figure 4.1 shows the layout of Photo-CATCH system. It has chambers for sample loading, atomic-hydrogen cleaning, NEA activation, and test of photocathodes at high-voltage. A multi-chamber design allows NEA activation of one cathode in parallel to cleaning another, and loading yet another. As each of these processes are highly time-consuming, having dedicated chambers saves a good amount of time. Separation of cleaning and activation processes ensure consistent vacuum conditions for activation experiments, and prevents contamination of alkali-metal dispensers which are natural adsorbents, the purity of which is essential for producing high-quality NEA surfaces. The beamline of Photo-CATCH will be equipped with devices necessary for the characterization of spin-polarized electron beams.

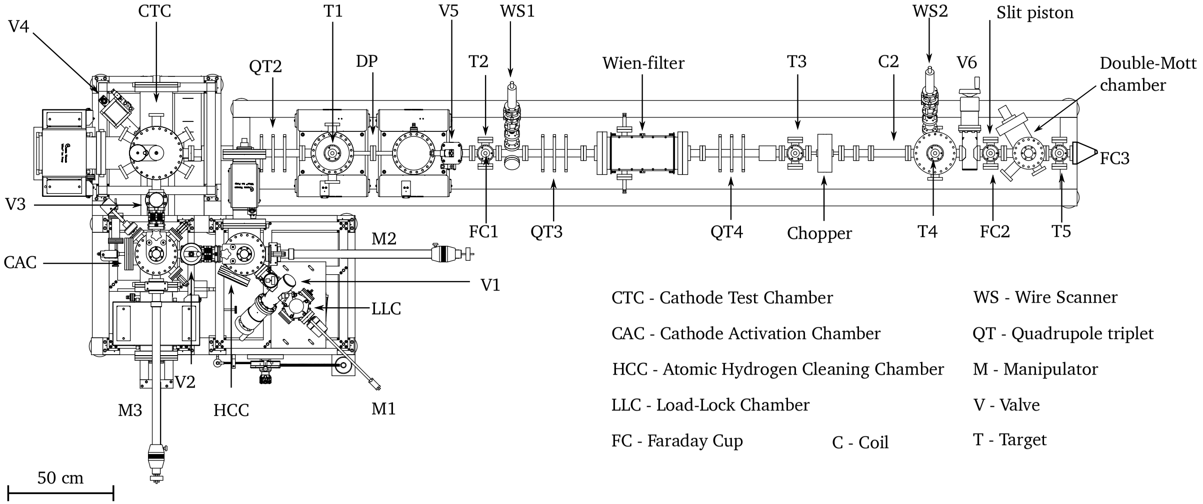

Figure 4.1: The layout of the Photo-CATCH facility. Ultra-high vacuum chambers are dedicated to sample loading (LLC), atomic hydrogen cleaning (HCC), NEA activation (CAC) and low-energy electron beam production (CTC). Electron optics immediately after CTC contain steerer magnets, a quadrupole triplet and a bending-dipole which are not visible in the drawing. The horizontal beamline is equipped with diagnostic elements such as targets, wire scanners, Faraday cups and Mott polarimeter for the characterization of spin-polarized electron beams. Laser from a nearby laboratory can be transported using optical fibers or mirror systems.

4.1 Vacuum terminology

Vacuum is in high demand in particle accelerators, and constitutes a crucial part of photoelectron guns utilizing semiconductor photocathodes. As described in section 3.3, an extreme level of vacuum is absolutely necessary for operating GaAs NEA photocathodes with a long lifetime. Also, the contamination on a cleaned photocathode surface, and consequently the quality of the NEA layer formed on this surface, are determined in part by the vacuum conditions in which these processes take place. Therefore, a major part of this thesis involved producing and maintaining very low pressures in Photo-CATCH chambers. The vacuum vocabulary[1] used in this work is tabulated in table 4.1. UHV is subdivided for the ease of reference. Additionally, the term extreme ultra high vacuum (XHV) is used for pressures below 1×10^{-11} mbar, although a proper definition to this term is lacking [181].

1000 mbar to 1 mbar	rough vacuum (RV)
1 mbar to 1×10^{-3} mbar	fore vacuum (FV)
1×10^{-3} mbar to 1×10^{-7} mbar	high vacuum (HV)
1×10^{-7} mbar to 1×10^{-9} mbar	upper ultra-high vacuum (u-UHV)
1×10^{-9} mbar to 1×10^{-11} mbar	lower ultra-high vacuum (l-UHV)
below 1×10^{-11} mbar	extreme ultra-high vacuum (XHV)

Table 4.1: The vacuum vocabulary used in this work. UHV is divided into three parts to ease the recurrent references to the specific vacuum ranges.

Vacuum, by definition, is any volume where the pressure of gases is less than the surrounding. The pressure, p, in a vacuum chamber of volume V is related to the total gas-load, Q_{tot}, and the effective pumping speed, S_{eff}, in the volume through the relation

$$Q_{\text{tot}} = V \cdot \frac{\mathrm{d}p}{\mathrm{d}t} + S_{\text{eff}} \cdot p \quad , \tag{4.1}$$

where the effective pumping speed is calculated from the nominal pumping speed, S, and the conductance, C, of the connecting element between the pump and the volume, using the relation, $1/S_{\text{eff}} = 1/S + 1/C$. The total gas-load is obtained by

---

[1] ISO 3529-1:1981; Vacuum technology–Vocabulary–Part 1: General terms

summing the gas-contributions from different sources of gases present in the vacuum chamber. It can be expressed as

$$Q_{\text{tot}} = Q_{\text{vol}} + Q_{\text{out}} + Q_{\text{per}} + Q_{\text{dif}} + \text{process gas} \quad , \tag{4.2}$$

where Q_{vol} is the gas existing in the volume at the beginning of the pump-down, Q_{out} is the *outgassing* from materials under vacuum including the chamber surfaces , Q_{per} and Q_{dif} represent gases entering the chamber through permeation and diffusion through the chamber materials. The process gas is defined by specific processes such as, for example, the controlled hydrogen flow during the atomic-hydrogen cleaning process.

4.1.1 Ultra-high vacuum

All of the Photo-CATCH chamber are designed to have a vacuum better than 1×10^{-8} mbar. To achieve a certain base-pressure, contributions from the individual components of Q_{tot} must be reduced below the required pressure. In a UHV system, the major contribution to total gas-load comes from leaks and desorption of gas molecules from the materials under vacuum. Leaks come in two categories: *real* and *virtual*. A real leak is when gases enter the system through a hole, usually caused by an incorrect tightening of the flanges or gaps in the weld, whereas a virtual leak results from volume-gas trapped in pockets within the system – such as windings of a screw or a fissure in the chamber wall. Since both have the same effect of increasing the pressure in the system, it is often difficult to distinguish one from the other. A real leak can be usually identified and isolated with a leak tester and a tracer gas (e.g. ^{4}He). A laboratory helium leak detector is capable of detecting leaks as low as 1×10^{-12} mbar l s^{-1} [182]. Once isolated, such leaks can be readily repaired by blocking the gas passage. ConFlat® (CF) flanges in combination with metal-gaskets offer a leak rating below 1×10^{-13} mbar l s^{-1}, and are recommended to be used at all joints that cannot be welded. Virtual leaks cannot be traced externally with an equipment, and thus, are hard to isolate. However, they can be prevented by taking extra care during chamber manufacturing, for example, adhering strictly to internal-welds and placing vent-holes near possible gas-traps. Virtual leaks present in a vacuum chamber may eventually disappear through outgassing, only to reappear after a chamber vent.

A residual gas analyser (RGA) connected to the vacuum system can also function as a leak testing device. In a chamber where access to neither an RGA nor a leak-detector is possible, the *pressure rise* technique can give some insights into gas-load in the system. In this method, the chamber under investigation is isolated from the pumps ($S_{\mathrm{eff}} = 0$) to let the total pressure in the chamber rise. In this conditions solution to equation (4.1) is

$$p(t) = \frac{Q_{\mathrm{tot}} t + p_0 V}{V} \quad , \tag{4.3}$$

where p_0 is initial pressure. The pressure in an isolated chamber will rise according to this equation in the absence of processes that produce a pumping or saturation effect. But, there is usually a small pumping effect caused by the chamber walls and ionization-gauges and saturation due to the dependence of the out-gassing rate on pressure and temperature. Hence the pressure-rise assumes the form,

$$p(t) = \frac{e^{-\frac{S_{\mathrm{eff}} \cdot t}{V}} (Q_{\mathrm{tot}} e^{\frac{S_{\mathrm{eff}} \cdot t}{V}} - p(0) S_{\mathrm{eff}} - Q_{\mathrm{tot}})}{S_{\mathrm{eff}}} \tag{4.4}$$

The saturation is reached when the number of particles escaping the material under vacuum equals the number being readsorbed. And there is usually a small pumping effect caused by the chamber walls and ionization-gauges which may show up as deviations in the observed pressure-rise curves. In contrast, the pressure of a leaky chamber will continue to rise in a linear fashion beyond the plateau. Knowing the values of V and p_0, the leak-rate can be extracted with an accuracy of ±25% [183]. Such estimates are useful for deciding if a leak has to be eliminated or can be tolerated to achieve the required base-pressure, and has been often used during the set-up of Photo-CATCH chambers.

With detectable leaks eliminated, the second major limitation to achieving lower pressures comes from the outgassing caused by materials in the system with a high vapour pressure near the targeted base-pressure. The process of out-gassing is proportional directly to temperature and inversely to the pressure. Any material that is not an essential part of the system and contributes Q_{out} is termed a contaminant, and has to be removed. Therefore, it is necessary to follow an appropriate cleaning procedure for the quality of the vacuum required. UHV chambers and components for Photo-CATCH have been subjected to a systematic cleaning procedure [184] to get rid of possible contaminations. The steps followed in this cleaning procedure are

- Washing with de-ionized water and wiping with clean cloth soaked in iso-propanol
- Ultrasonic bath, alternately with active/neutral detergent and hot/cold de-ionized water

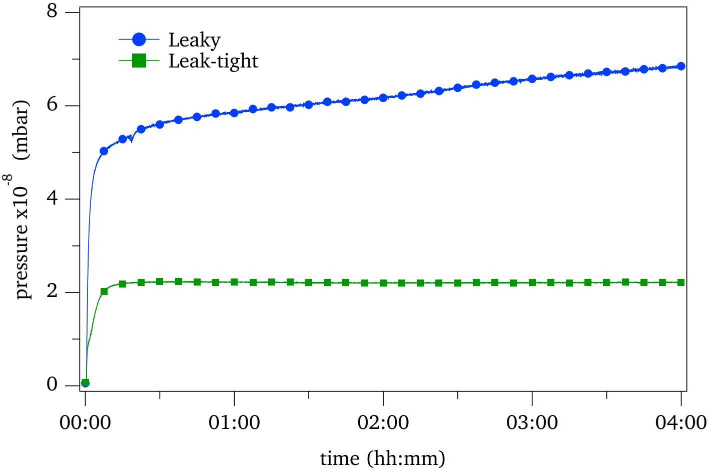

Figure 4.2: Pressure-rise behaviour of leaky and leak-tight chambers in the absence of pumping. The pressure for the leak-tight case can be seen to saturate. Measurement taken at the hydrogen-cleaning chamber.

- Drying in clean hot-air oven at 100 °C
- Clean-room storage, packed in aluminium foil/polyethylene bag

Lint-free wipes wetted with iso-propanol were used to wipe the parts prior to installation. The components were always handled wearing powder-free gloves. Assembly was carried out in a clean-room or under a portable flow-box unit.

Below u-UHV, a practical limit is reached where lower pressures could not be achieved solely by increasing the pumping speed in the chamber. This is expected since the pumping speed of all the UHV pumps strongly depend on the pressure and most of the pumps have their nominal speed in the HV to u-UHV transition region. Under this condition, Q_{out} and Q_{dif} will dominate the gas-load in the chamber and further pressure reduction will only be achievable through minimization of these quantities. The primary source of outgassing in a UHV system is adsorbed H_2O molecules. Due to their polar nature, water molecules can make strong chemical bonds of covalent nature as well as physical adsorption bonds to the exposed surfaces [185]. Outgassing from the chamber walls reduces with pumping usually only in a time^{-1} manner, and the desorption must be quickened by providing energy to the adsorbed molecules to achieve UHV in reasonable span. The most common method of removing water from a vacuum chamber is the thermal-desorption method, known as the *bake-out*. It is done by heating the vacuum chamber under HV or u-UHV conditions for several hours at a temperature between 120 to 400 °C observing the temperature limit of the components attached to the system. The procedure begins with pumping down the chamber to u-UHV pressures at room temperature to remove weakly adsorbed water molecules in order to reduce activated chemisorption during the bake-out. It may last for hours to weeks depending on the material's history of exposure to atmosphere. In a baked-out chamber, H_2 will be the prominent gas species with minor traces of CO, CO_2, O_2, H_2O and CH_4.

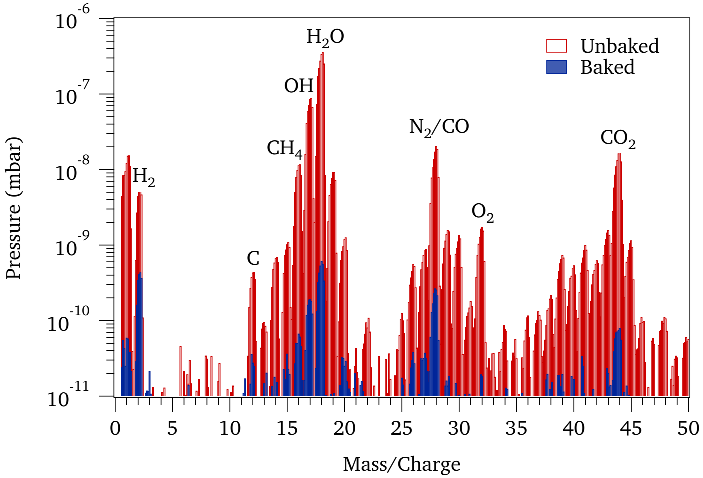

Figure 4.3: Comparison of the residual gas spectra of HCC before and after a bake-out. Presence of high traces of N_2,O_2 and CO_2 in the baked out chamber is an indication of a possible air-leak into the system. H_1 and CO appears mostly due to H_2 and CO_2 cracking at the RGA filament.

It is argued that some of the gaseous species identified by an RGA in a baked-out UHV chamber are artefacts of the ionizing elements in the system, including contributions from the vacuum gauges [186, 187]. A comparison of partial pressures before and after a bake-out of H_1 cleaning chamber at 150 °C for 24 hours is given in figure 4.3. The base pressure after this bake out was $>5 \times 10^{-10}$ mbar. The excess presence of primary components of air indicating a real-leak was responsible for this limitation. In order to achieve XHV conditions, the outgassing needs to be reduced further by surface treatments such as oxidation or electro-polishing. Slow-outgassing of dissolved hydrogen from bulk of the stainless steel, blameable for Q_{dif}, can be suppressed by annealing the chamber at very high temperatures for short time or at modest temperatures for a long time. This process is known as *vacuum firing* [188, 189]. UHV chambers of Photo-CATCH preparation system were vacuum fired at 450 °C for 48 h at a pressure better than 1×10^{-6} mbar in a vacuum oven[2]. The annealing temperature was limited by 304L stainless steel used to construct the chambers.

4.1.2 Pumps in the system

Since there exists no single pump which can pump-down a chamber from atmosphere to UHV/XHV conditions, various pumps based on differing working principles have to be used for this purpose. A positive displacement (roughing) pump, such as a diaphragm pump, can bring the chamber from atmospheric pressure to rough or medium vacuum. All the pumps that operate in HV/UHV regime require such a mechanical pump to create an operable vacuum condition, and to continuously remove the gas from pump-outlets. Most commonly used u-UHV pump is the turbo-molecular pump (TMP) which compresses gases to FV so that a mechanical pump can remove them from the system. The TMP operates in a vacuum range of few mbar down to $<1 \times 10^{-10}$ mbar. Detailed discussion on the theory and operation of TMPs can be found in references [190] and [191]. Below HV, the behaviour of gases is dictated by molecular-flow, and the pumps that base their pumping principle on viscous-flow suffer considerable loss of their pumping speeds. In order to reach l-UHV or XHV, one has to resort to pumps that employ the principle of gas trapping.

Capture pumps rely on chemical or physical adsorption of molecules and their subsequent burial by sputtering (*gettering*) or diffusion of the gas species into the bulk of the pumping material. A sputter ion pump (SIP) works by ionizing gas molecules with electron impact in a Penning cell and then accelerating the ions with a high voltage (3 to 7 kV). The pumping speed and capacity of the SIP depend on the gas species pumped and the cathode material that buries it. Getterable gases are O_2, N_2, CO, CO_2, CH_4, Ar_2 and many others. SIP can only be operated in a vacuum better than 10^{-4} mbar due to glow-discharge occurring at the Penning cells at high pressure, which would prevent the sputtering process. The maximum (nominal) pumping speed is reached at about 10^{-6} mbar and decreases with the pressure in the chamber [192]. Hydrogen, to an extend, is also getterable, but is incapable of

---

[2] Technology Laboratory (ENTL), GSI Helmholtz Centre for Heavy Ion Research, Darmstadt

producing a sufficient sputtering yield by itself. Although a considerable fraction of hydrogen pumping takes place at the anode, the major mechanism of hydrogen pumping is due to the diffusion into the cathode material. The pumping speed for hydrogen is typically two times higher than the speed for nitrogen. If the temperature increases, the diffusion rate is increased but a fraction of pumped hydrogen may be released because the binding energy of titanium hydride is lower than that for nitride and oxide. The base pressure of a chamber pumped by SIP is limited by the equilibrium between pumped and desorbed molecules. It maybe possible to reach XHV in a chamber pumped by an SIP after the baking out both the SIP and the chamber [193, 194].

Another type of capture pump, called the non-evaporable getter (NEG), uses highly reactive alloys to *sorb* the gases. Gases such as O_2, N_2, H_2O, CO and CO_2 impinging on the NEG surface are dissociated and permanently trapped in the form of stable chemical compounds. Hydrogen and its isotopes are diffused and dissolved as a solid solution in the getter-bulk. Some of the dissolved gases could be released by heating the pump material above 400 °C, which makes reversible pumping of these gases possible for an NEG. To date, NEG pumps offer the highest pumping speed/cm^2 for H_2. However, noble gases and CH_4 at room temperature are not pumped by these type of pumps. Combined with an SIP to handle methane and argon, NEG pumped chambers can reach a vacuum in XHV domain. Common NEG materials are Zr-V-Fe (St172) and Ti-V (St185) and the high capacity Ti-Zr-V-Al (ZAO) alloy that can also be operated at high temperatures. Unlike other vacuum pumps, NEG pumps do not require high-voltage or magnetic fields, and relies entirely on chemi- and physi-sorption principles. Otherthan during an activation process of the NEG material by heating at a specified temperature, it does not require any electrical power to for its normal operation. This makes the NEG highly flexible that they can be made into cartridges, tablets or stripes, and can be coated on chamber surfaces to convert the entire chamber into a large pump [195–197].

4.2 Photo-CATCH chambers

During its lifetime, a photocathode moves through four different vacuum vessels in Photo-CATCH. The chambers are identified as the load-lock chamber, the hydrogen cleaning chamber, the cathode activation chamber - together called the *preparation system* - and the cathode test chamber. The transport of H_1-cleaned photocathodes to SPIN can be accomplished by means of a transport vessel, which also functions as a vessel for the long-term storage of cleaned samples in UHV. Almost all of the vacuum chambers, holders and beamline parts are made in-house, using stainless steel 304L, unless specified otherwise. Following sections describe each of these chambers and their components in detail.

4.2.1 Load-lock and transport vessel

A small load-lock chamber (LLC) introduces samples into the system without breaking the vacuum in the other chambers. To load a sample, the LLC is vented to dry N_2 gas, opened to atmosphere and the puck containing the photocathode is placed in a transport-fork (see figure 2.3). After the chamber is sealed and pumped down to u-UHV pressures, the sample can be transferred to the next chamber. This practice helps to avoid frequent venting of the preparation system, thereby lengthy bake-out cycles. The LLC also serves as a chamber for annealing of molybdenum (Mo) pucks and masks in UHV, in order to limit their outgassing. Pre-heating of the samples at moderate temperatures can reduce a substantial amount of gas-load in the hydrogen cleaning chamber which otherwise would have to be pumped by the capture pumps.

A drawing of the LLC is given in figure 4.4. Using a quick-flange® (QCF) at the entry port of LLC yields a faster sample loading compared to a conventional bolted-CF flange, since in a QCF, the gasket is sealed by the action of a single fastener. The puck with photocathode is held in the LLC by a fork, attached to a 400 mm magnetically-coupled linear transfer arm. A $255\,\mathrm{l\,s^{-1}}$ (for N_2) TMP[3], backed by a $\sim 0.7\,\mathrm{l\,s^{-1}}$ diaphragm pump, is used to pump the chamber. The u-UHV pressure is typically reached in less than 30 minutes. A combined Pirani and cold-cathode vacuum gauge operating in 1000 to 5×10^{-9} mbar range of vacuum is used for measuring the pressure in LLC. A tungsten filament is used for annealing the puck up to 500 °C, while the temperature is measured using a portable pyrometer. The photograph of LLC can be seen in figure 4.8 in the following section.

The LLC is always vented using dry N_2 through a PTFE-filter. It has been observed that venting LLC with air causes the pump-down curve to deviate from its standard form. Such a difference arising in the pump-down curves are shown in figure 4.5. The longer the chamber is exposed to atmosphere, the more will be the deviation from its standard pump-down behaviour, due to accumulation of more layers of water on the chamber walls which will only outgas slowly over time. A full recovery is possible only by baking out or long-term pumping of the chamber. Influence of the

---

[3] HiPace® 300M | Pfeiffer Vacuum

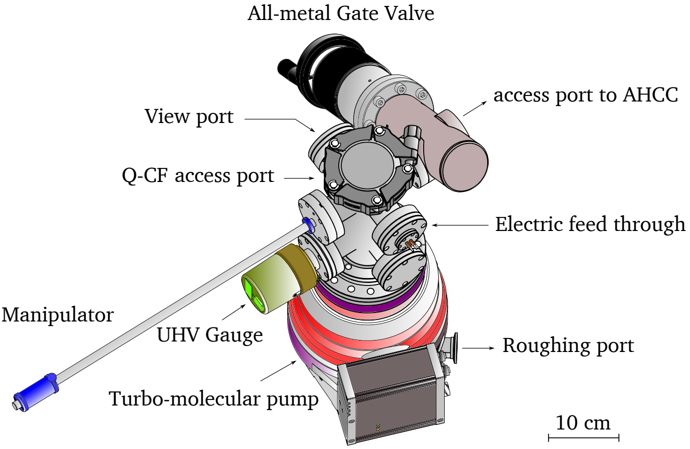

Figure 4.4: Three dimensional drawing of the load-lock chamber.

purity of venting gas on the pumping speeds and the benefits of using ultra-pure nitrogen are discussed in reference [198]. The LLC reaches a pressure in the lower 10^{-8} mbar in about 2 hours. A few months of pumping results in a base pressure less than 5×10^{-9} mbar, below the measurement limit of the vacuum gauge in the LLC.

A portable UHV chamber, the transport vessel (TV), is envisaged for transporting atomic-hydrogen cleaned photocathodes to SPIN, as well as for long term storage of cleaned photocathode samples. The design of such a chamber is given in figure 4.6. It is an about 2 litre rectangular chamber, pumped by a $400\,\mathrm{l\,s^{-1}}$ NEG pump. Use of SIP to reduce the presence of methane and noble gases is omitted on the basis that these gases are not detrimental to the photocathode surface during storage [25]. However, an extra port is added to the chamber for connecting a small SIP, may the need arise. A properly baked-out TV is expected to hold a vacuum better than 5×10^{-11} mbar. Space for up to three pucks is available in the carousel. A magnetically coupled shaft can be used for linear and rotational motions of the carousel to enable the cathode exchange between TV and LLC. An all-metal gate-valve will be used at the entry port to ensure both an easy access and a low leak rate. The vacuum in the camber can be measured using a cold-cathode vacuum gauge.

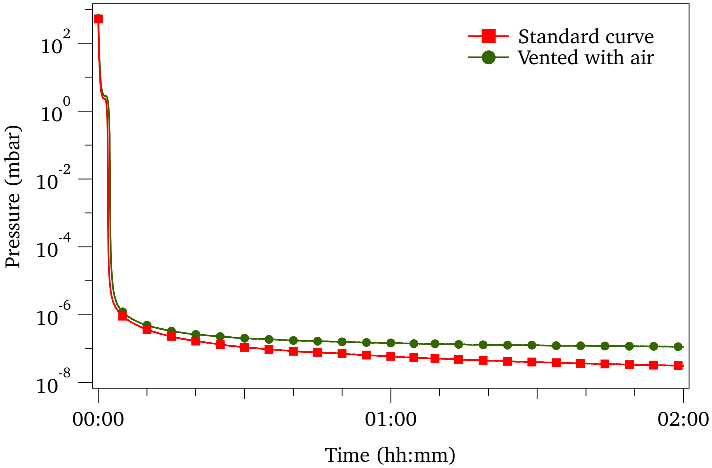

Figure 4.5: Pump-down curves resulting from venting the LLC with N_2 (red) and air (green). Re-adsorption of water molecules on the chamber walls during the exposure to air causes the deviation of the curve upon reaching UHV regime.

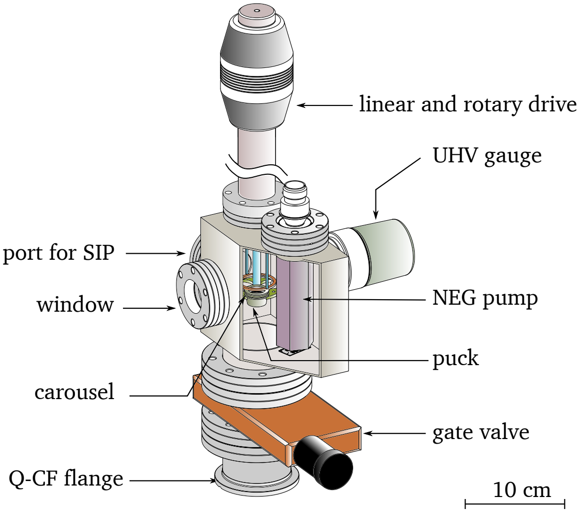

Figure 4.6: Conceptual drawing of the transport vessel for photocathode storage and transport to SPIN.

4.2.2 Hydrogen cleaning chamber

The hydrogen cleaning chamber (HCC) is dedicated to the cleaning of photocathodes, either thermally or by exposure to an H_1-flux, under l-UHV conditions. The chamber is isolated from LLC by an all-metal gate valve[4] which is opened to allow the sample from LLC to be transferred into the carousel in HCC. At a time, two pucks can be stored in the carousel for cleaning. A drawing of this chamber is given in figure 4.7. In this cutaway-view of HCC, a puck next to a heating coil (obscured by puck in the drawing) can be seen to be positioned on axis to the source of atomic-hydrogen, mimicking the arrangement during an H_1-cleaning experiment. There are three UHV view-ports on the chamber used for illumination, temperature measurement, and optical inspection. HCC is pumped by an $100\,\mathrm{l\,s^{-1}}$ SIP and a $400\,\mathrm{l\,s^{-1}}$ NEG to a base-pressure less than 3×10^{-11} mbar measured by both a cold-cathode ionization gauge[5] and the SIP controller. Linear and rotational motions of the carousel is realized through a combination of z-translator and bellow-sealed rotary drive. A magnetically-coupled manipulator arm transfers the samples between HCC and the next chamber.

The hydrogen atom beam source (HABS) operates at temperatures up to 2000 °C and is water-cooled to reduce the thermal load on the system. Samples are brought to cleaning temperatures by radiative-heating using tungsten-coils, that are heated beyond 700 °C. Frequent operation of the component in the HCC at elevated temperatures, and contamination due to species liberated during cleaning process deteriorate the vacuum condition in HCC. Due to this, pressures close to 9×10^{-11} mbar are typical between cleaning processes. Although a pressure rise to 1×10^{-6} mbar of H_2 can occur for a short period during the atomic-hydrogen cleaning (AHC) runs, the pumping speed in the chamber is sufficient to bring it back to l-UHV in less than 2 hours. The NEG pump[6] used in HCC has a very high sorption capacity - about 3700 mbar l - for H_2, making it suitable for pumping large amounts of H_2 before a regeneration of the pump becomes necessary. The SIP, although it pumps hydrogen at twice its nominal pumping speed, is incapable of trapping H_2 permanently. Therefore, the NEG is tactically placed inside the SIP to re-absorb the escaping hydrogen pumped by the SIP, at the expense of about 30–40% of the NEG's pumping speed[7].

---

[4] 48132-CE01-0002 | VAT

[5] IKR 270 | Pfeiffer Vacuum

[6] CapaciTorr® HV 200 | SAES Getters

[7] private communication with Dr. Andrea Cadoppi, SAES Getters

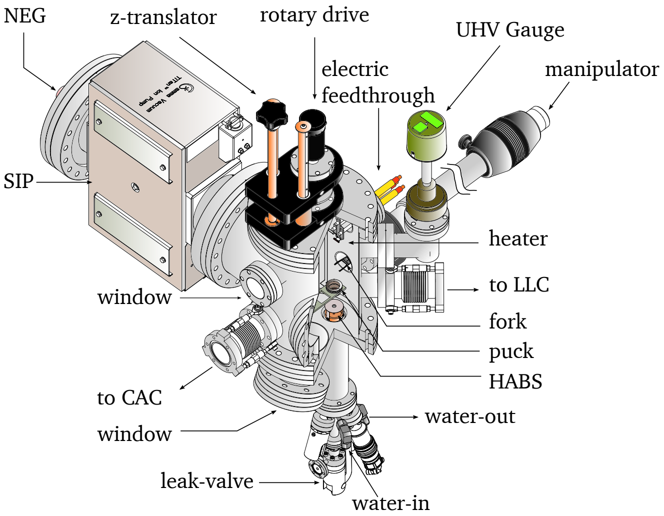

Figure 4.7: Cut-away drawing of the hydrogen cleaning chamber (HCC). Positioning of the puck mimics that during an atomic hydrogen cleaning process. Obscured by the puck is a heating coil that radiatively heats the sample during H_1 cleaning.

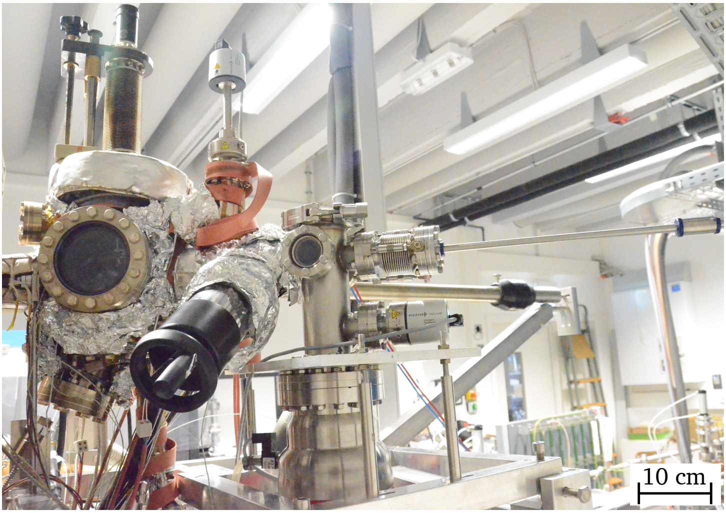

Figure 4.8: Photograph of LLC and HCC as installed at the Photo-CATCH.

Heating the HABS to the operating temperature, T_H, causes an increase in the partial pressures of H_2, N_2 and CO in the chamber. This pressure increase is caused by temperature enhanced desorption from materials such as stainless-steel, tungsten and copper that are used for constructing HABS. Figure 4.9 shows the observed total pressure rise in HCC as a function of T_H. The vapour pressure of tungsten (W), p_W, emanating from HABS strongly depends on the capillary temperature, T_W, of the W-capillary. Data on this dependence is provided by the manufacturer and is tabulated in table 4.2. Also the relative atomic flux, η_{rel}, and the relative lifetime, t_{rel}, of the heater are influenced by T_H as given in the table. Therefore, an appropriate temperature high enough to obtain sufficient H_1 flux, ϕ_{H_1}, and low enough to keep p_W at a minimum shall be endorsed to achieve an optimum cleaning of the semiconductor surfaces. For cleaning samples highly sensitive to contamination, such as GaAs to be activated to NEA state, $T_H \leq 1800\,^\circ\mathrm{C}$ is recommended. A temperature 150 °C lower than the actual temperature of the capillary is measured due to the positioning of the integrated type-C thermocouple inside the HABS. Since this is the only directly measurable temperature, it is taken as the operating temperature of HABS and correction is made in calculations.

T_W (°C)	η_{rel}	t_{rel}	p_W (mbar)
1770-1820	0.25	100-200	$\sim 1 \times 10^{-10}$
1900-1950	0.60	20-30	$\sim 2 \times 10^{-9}$
2000-2050	0.90	4-5	$\sim 1 \times 10^{-8}$
2100-2150	1.00	1	$\sim 1 \times 10^{-7}$

Table 4.2: Manufacturer data for the dependence of tungsten-vapour pressure, relative atomic flux and heater lifetime on the capillary temperature of the HABS.

The temperature of the sample is measured either on the sample surface or on the molybdenum puck using an infrared (IR)-pyrometer[8] which can measure temperatures from 100 to 700 °C with ±0.1 °C accuracy. A diagrammatic representation of the hydrogen-feed arrangement to HABS is presented in figure 4.10. Hydrogen of purity N50 (99.999%) from a laboratory-bottle (12 bar, 1 litre) is pressure reduced and passed through a filter[9] prior to supplying it to HABS via a fine-control leak-valve. The feeding pressure of H_2 is not measured directly at the feed-line, but estimated from the chamber pressure rise. After its installation in the chamber,

---

[8] IMPAC IGA 320/23-LO (MB 7) | LumaSense

[9] MicroTorr Hydrogen purifier MC1-904F with integrated 0.003 μm Filter

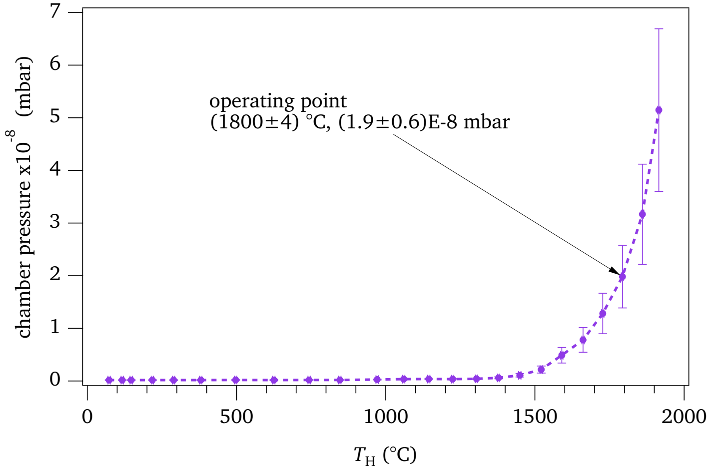

Figure 4.9: Variation of chamber pressure with the temperature of HABS capillary. Near the operating temperature of 1800 °C the pressure stabilizes below 2×10^{-8} mbar.

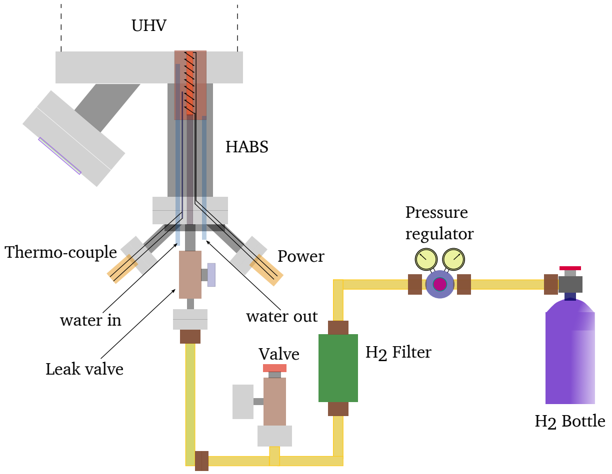

Figure 4.10: Schematic of the gas feed line to the HABS. Hydrogen from the bottle is passed through the pressure regulator and filtered before leaking it to the capillary through an all-metal leak valve. Part of the gas line until the filter is bakeable with a pump attached to the all-metal angle valve in the line.

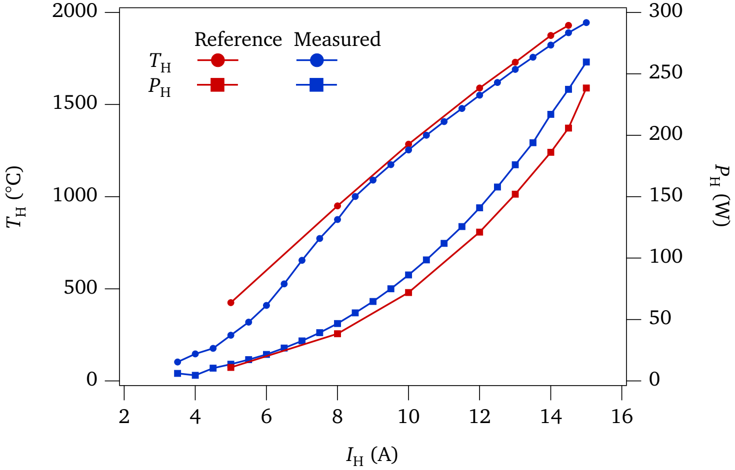

Figure 4.11: Dependence of HABS temperature, T_H, and deposited power, P_H, on applied current, I_H. Reference values are taken from manufacturer's calibration data.

HABS has shown only minor variations from the manufacturer's calibration values. Comparison of the calibration data taken at HCC and that provided by the manufacturer is shown in figure 4.11. The slightly higher electric power required to bring HABS to the operation temperature is thought to be caused by the differences in temperature and flow rate of the cooling water.

4.2.3 Activation chamber

The NEA activation of cleaned cathodes take place at the cathode activation chamber (CAC). This chamber and the HCC are separated with an all-metal gate valve. Pumped by a $200\,\mathrm{l\,s^{-1}}$ SIP and $400\,\mathrm{l\,s^{-1}}$ NEG combination, the chamber maintains a base pressure less than 2×10^{-11} mbar as measured by a cold-cathode ionization gauge. However, the pressure indicated by the SIP controller based on a highly sensitive ion-current measurement falls below the detectable limit (1×10^{-11} mbar). This indicates the possibility of XHV conditions existing, at least, near the pumps. During the activation process, the pressure can rise up to 8×10^{-9} mbar, but returns to the base pressure in less than 3 hours following an activation process. Figure 4.12 shows the drawing of CAC. Configurations of carousel and sample manipulators resemble those in the HCC as described in the previous section. Two

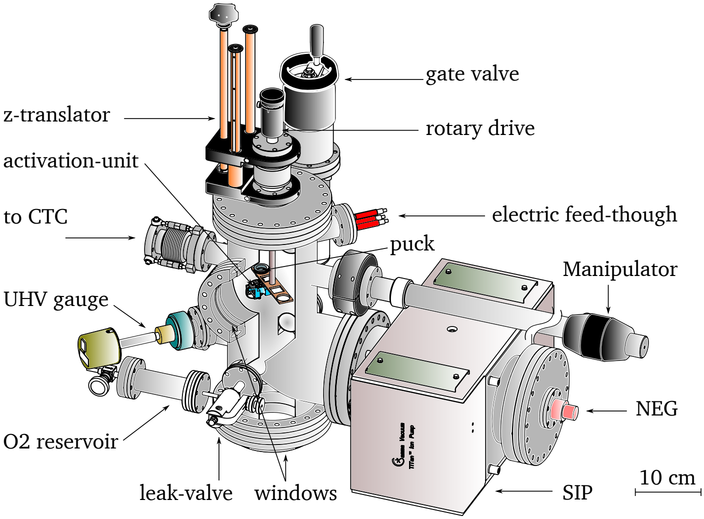

Figure 4.12: Cut-away view of the cathode activation chamber (CAC). Not visible are the heating coils used during two-stage activations.

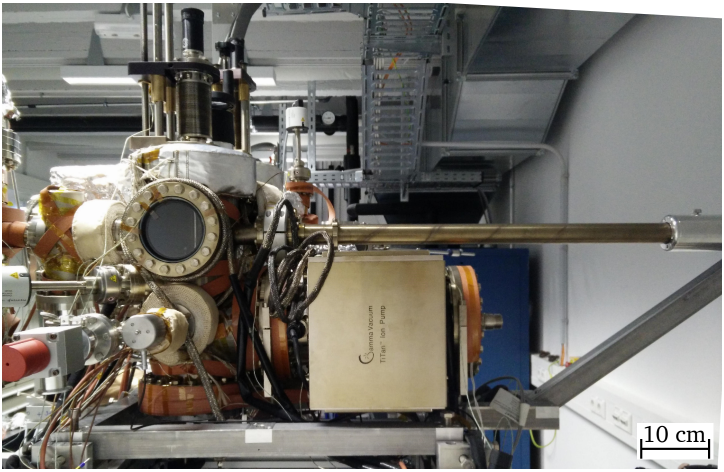

Figure 4.13: Photograph of cathode activation chamber as installed at the Photo-CATCH.

viewports present at the bottom, and on the side of the chamber are used for optical inspection, and laser and pyrometer, respectively. One of the two electrical feed-throughs are connected to a pair of tungsten coils used for heat-cleaning or two-stage activation. The other feed-through carries an assembly of electrical elements used for photocathode activation, here after referred to as the *activation unit*.

Figure 4.14 shows the activation unit. It is held together by a piece of XHV grade machinable glass-ceramic, macor®. Vacuum fired stainless steel bars completes the electrical connections to the Cs and Li dispensers[10]. A ring-shaped anode on this assembly is used to collect the photocurrent. The elements are positioned in such a way that a vault-shaped cut through the insulator-block lets the laser to be focused on the photocathode. The whole assembly is rigid, and is easy to dismantle if a dispenser replacement becomes necessary. O_2 is introduced into the chamber via a piezoelectric leak-valve[11] connected to a reservoir that has been baked-out and evacuated to a pressure below 1×10^{-8} mbar prior to filling O_2 of purity N60. The piezoelectric-valve has a minimum operable leak-rate of 1×10^{-10} mbar l s^{-1}, and can be operated in a pulsed mode up to 30 kHz.

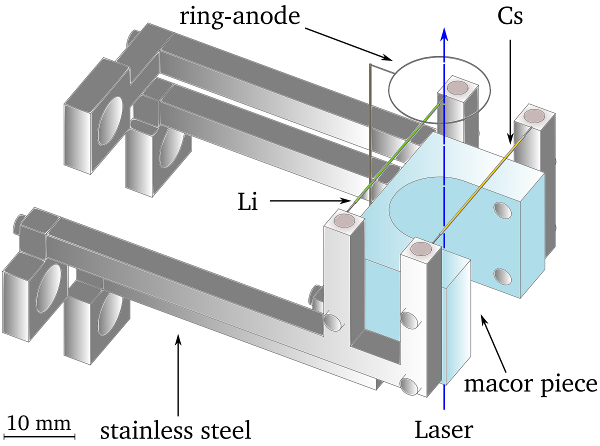

Figure 4.14: Assembly of the electrical components used for the NEA activation process.

---

[10] CS/NF/8/25 & LI/NF/1.25/25 | SAES Getters

[11] PLV1000 | Oxford Instruments

The flow rate of alkali metals can be precisely controlled by adjusting the dispenser current. Even though currents from 4 to 7.5 A is recommended for appreciable alkali evaporation [199], values between 2.8 and 4 A were found to be sufficient for different activation procedures adopted at Photo-CATCH. The observed chamber pressure rise proportional to the alkali fluxes, with respect to current passed through the dispensers are shown in figure 4.15. These evaporation rates are quite reproducible. The piezoelectric leak-valve for O_2 requires up to 1 kV and is driven by a 3 kV-supply. It is remotely controlled through an Arduino™ DUE micro-controller based board, and is limited to a maximum output of 500 V. The operating range of the valve depends on the torque applied to the screw that sets the initial position of the internal sealing. The valve was calibrated by the manufacturer for the required UHV operation with a torque of 38 mN m. However, it was found that use of this value did not suit the vacuum requirements of CAC. Using a moment of 38 mN m prevented complete closing of the valve even in the absence of a voltage across the piezo-stack, and resulted in an constant elevated pressure of $\sim 1 \times 10^{-10}$ mbar in CAC. A new value for the torque, that allows CAC to reach its base pressure and allows the valve to operate in required pressure range has been found by trial and error. The calibration data with new torque is shown in figure 4.16. Presently the valve is tightened to 36 mN m using a calibrated torque-wrench. However, a re-calibration of the valve may become necessary following another bake-out of the system.

4.2.4 Test chamber and beamline

The Cathode test chamber (CTC) contains the electron-gun of Photo-CATCH. This chamber is intended for the test of photocathodes at a high-voltage. Differently from the SPIN, the electron gun in CTC has an inverted-insulator geometry. The high-voltage Pierce-geometry electrode [28] has been simulated for voltages up to 100 kV but, limited by the voltage-supply, will be operated at 60 kV at the Photo-CATCH. Using an inverted-insulator geometry gun (IIGG) permits a compact design of the source chamber and improves the safety of both the operator and the machine compared to traditional external-insulator geometry electron guns. Details on the conceptualization, design and construction of this gun and the chamber can be found in the reference [28]. CTC and CAC are connected through an all-metal gate valve through which the sample can be loaded into the electrode. From the vacuum requirements of the operation of NEA-GaAs photocathodes, as discussed in section 3.3, a stable XHV environment is required in CTC. To this end, this chamber is both constructed using marine-grade stainless steel 316L and electro-polished by

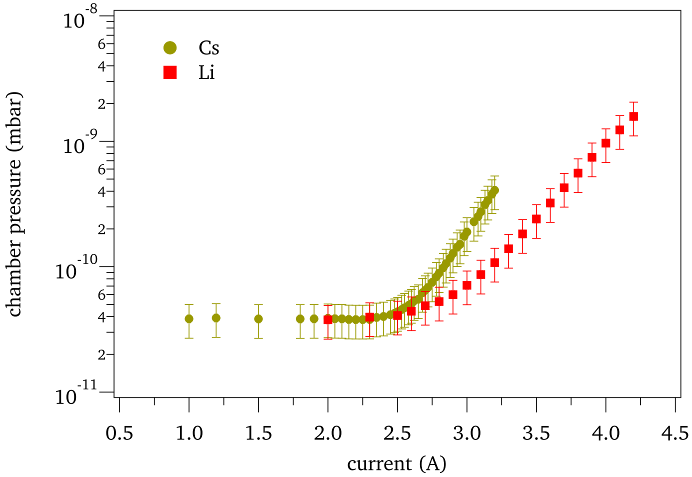

Figure 4.15: Pressure rise in the CAC with respect to current passed through the Cs and Li dispensers.

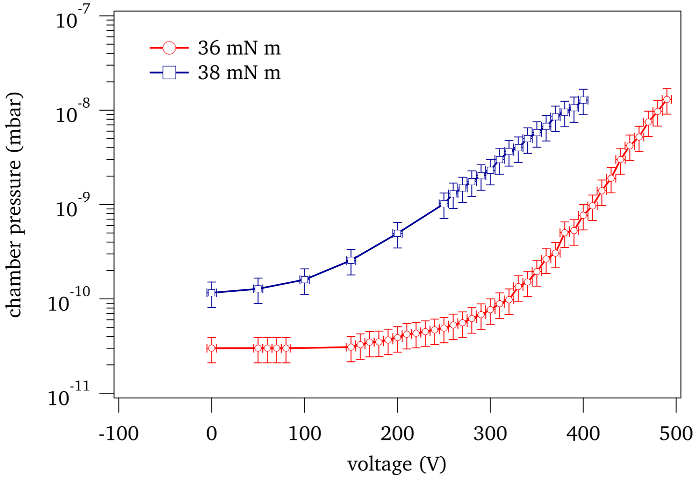

Figure 4.16: Calibration data for the piezoelectric leak-valve at a torque of 36 mN m. Behaviour of the valve at a torque of 38 mN m is added for comparison. The pressure gauge used for the measurement has a repeatability of ±5%.

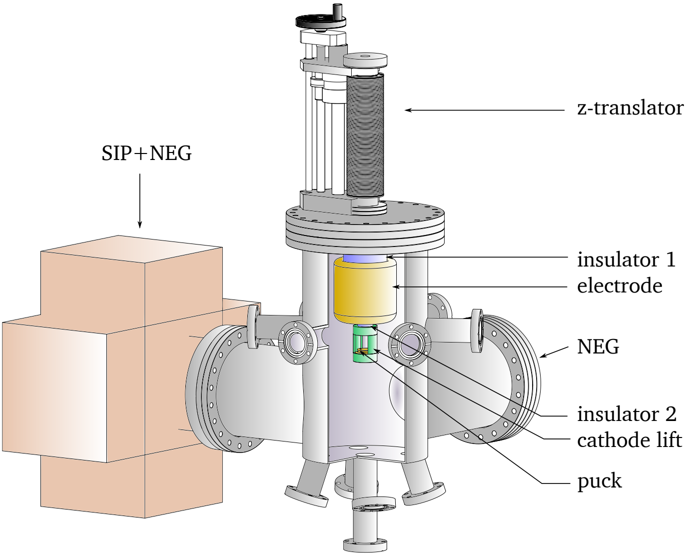

Figure 4.17: Conceptual drawing of CTC showing the inverted-insulator electrode geometry.

the vacuum components manufacturer VACOM. A 400 l s^{-1} SIP and 400 l s^{-1} NEG combination, and a 2000 l s^{-1} NEG pump are employed to pump CTC. Insulators used for the construction of IGG are UHV compatible alumina[12] which has been brazed to 316L parts. A drawing of this chamber is presented in figure 4.17.

For analysing the composition of vacuum in the chamber, a quadrupole mass spectrometer[13] is attached to one of the ports. This unit measures partial pressures in 10^{-14} mbar range with the help of an electron multiplier. Additionally, a hot cathode [14] gauge measures the total pressure in the range of 1×10^{-2} to 5×10^{-12} mbar. IIGG uses a lift-type mechanism identical to SPIN electron gun for positioning the cathode inside its cylindrical electrode. Laser approaches the cathode surface from the bottom of the chamber, through a window in the bending-dipole magnet chamber. The centre of the photocathode aligns with the the geometric and electric centre of IIGG. Electron beams of up to 60 keV from the gun exit through pneu-

---

[12] Al203 97® | SCT Ceramics
[13] Dycor LC-D100M | AMETEK
[14] BARION® XHV (BATX) | VACOM

matically operated gate-valve. A combination of steerer-magnets and quadrupole-magnet triplet, positioned immediately after the valve, can be used for focusing the beam it gets bent by 90° into Photo-CATCH beamline. In order to separate the superior vacuum of CTC from the moderate UHV ($\sim 10^{-9}$ mbar) required in the beamline, a differential pumping (DP) stage consisting of two $300\,\mathrm{l\,s^{-1}}$ SIPs is set-up (see figure 4.1). The pressure in the DP region is measured by the SIP controller and is usually below their detection limit of 1×10^{-11} mbar.

The beamline has magnetic coils, steerer-magnets and quadrupole triplets placed in appropriate positions, as shown in figure 4.1, to guide and focus the electron beam. CROMOX® and gold-plated beryllium oxide targets will be used at different positions to image the beam. A Wien-filter and magnetic coil combination downstream can rotate the electron spin direction throughout the entire solid angle. For measuring the degree of polarization of the electron beams, a double-scattering Mott-polarimeter will be set-up [200]. A chopper-slit arrangement will be used to determine the temporal profile of both the current and the polarization of electron bunches with a resolution of 1 ps [201]. Emittance of the beam will be determined using two wire-scanners. A LabVIEW®-based accelerator control system, utilizing the EPICS server, has been developed and tested [202] to operate all of the beam-diagnostic elements using either the standard input devices of a PC, or with a game-pad in a highly intuitive way.

The same laser systems used at the SPIN for the production of polarized/unpolarized electrons will be readily available for the Photo-CATCH in its operational phase. The laser system based on a Titanium-Sapphire oscillator[15], pumped by a 18 W solid-state laser[16], is typically tunable in a range of 600 to 1000 nm and is capable of producing pico- or femto-second pulses with a peak power of 2 W at 800 nm. For studying the wavelength dependence of polarization and quantum efficiency of the photocathodes at low-currents, a supercontinuum light source tunable within 480 nm to 1000 nm has been recently developed [203, 204]. A detailed description of the laser systems available for Photo-CATCH and SPIN can be found in the published works [205, 206].

At the time of writing this thesis, the use of CTC and the electron gun for characterization of photocathodes was not possible and neither was the installation of beamline finished. There was a mishap at IIGG while trying to load an activated cathode for the first time. Complications arouse, possibly due to a misalignment of

---

[15] Coherent Mira HP-D

[16] Coherent Verdi™V18

the lift in the electrode and insufficient clearance between the lift and outer electrode, resulting in scratches on the polished surfaces of the electrode. An attempt to forcefully move the lift locked the translator in position. The CTC had to be vented to dismantle and inspect the electrode structure. A modification of the electrode design by incorporation of a conical-spring is being considered. Furthermore, lower than expected vacuum conditions measured in the chamber points to a possible leak at the insulator welding or at the top-flange assembly. Test of the re-designed electrode and elimination of the leaks are necessary to take the Photo-CATCH gun into its operational phase.

5 First experiments using the Photo-CATCH preparation system

The first studies using the system which are presented in this dissertation are focused mainly on three goals. First of which is finding a recipe for reproducibly activating GaAs photocathodes to an acceptable quantum efficiency, and trying out novel methods to achieve higher photo-responses. Second, investigating and establishing optimum conditions for atomic-hydrogen cleaning of contaminated photocathodes. Third, addressing the lifetime degradation problem of NEA photocathodes in UHV conditions. GaAs samples used for the experiments are listed in table 5.1. Fresh samples are cleaved in a clean-room environment into approximately 11 mm×11 mm pieces by pressing a knife-edge along the cleavage plane of an epitaxial *p*-GaAs wafer. The square piece of GaAs is then held with a tungsten spring inside an Mo-puck and transferred under atmospheric conditions to the LLC. In addition, used samples which could not be activated to an acceptable *QE* after heat-cleaning below 580 °C are collected from SPIN to test H_1-aided rejuvenation.

Identifier	Condition
B1	unknown, randomly picked from disposed SPIN-samples
B2	freshly cut from an old wafer
B3	left in HCC during bake-out of the chamber
B4	no photo-response at SPIN
B5	freshly cut from relatively new wafer
S1	freshly cut from EB96

Table 5.1: Nomenclature of the samples used for the experiments. B and S stand for bulk-GaAs and for GaAs/GaAsP superlattice photocathodes, respectively. Comments describe the history of the samples.

Sample B1 was used at SPIN and disposed after its lifetime. Sample B2 is cut from half a wafer left in the shelf for at least 5 years. B3 showed very low response at SPIN, and was kept in the HCC as a cold-spot in the chamber during a bake-out to cause heavy contamination to its surface. Sample B4 was removed from SPIN due to insufficient photo-response and was exposed to atmosphere for over an year. B5 is freshly cleaved from a relatively new GaAs wafer[1]. S1 is a piece from EB96 wafer.

---

[1] 2014 batch, Wafer Technology Ltd., UK

All the experiments reported in this chapter has been conducted in HCC and CAC of the Photo-CATCH. Without the gun-chamber in operation, an investigation of many important characteristics of the photocathodes, such as wavelength dependence of *QE*, degree of polarization of electrons emitted from the superlattice sample EB96, dark lifetime and operational lifetime of high *QE* cathodes under XHV conditions were not possible.

5.1 Atomic-hydrogen cleaning

Photo-CATCH does not have any equipment to investigate the morphology and composition of the sample surfaces to verify and quantify the cleaning of the samples. Therefore, the extent of atomic-hydrogen cleaning is determined by evaluating the *QE* achieved after each cleaning cycle. This is valid as long as two conditions are obeyed: (1) Comparisons are only made with a sample to itself, as the *QE* can also vary depending on the crystal parameters which usually differs from sample to sample and (2) activations should follow a standard procedure that is known to produce reasonable *QE* on clean cathode surfaces. To ensure the latter, it was necessary to establish an activation recipe before attempting the AHC optimization. A standard activation procedure based on Co-De was derived from activation experiments conducted with a freshly cleaved sample (B2) as described in section 5.2. The procedure derived is used for activating the samples throughout the H_1 cleaning experiments.

The atomic hydrogen source HABS is operated remotely via an interface provided with the power-supply unit[2]. H_2 is admitted manually via a graduated leak-valve. The pressure in the chamber and the sample temperature are monitored using dedicated computer programmes. The temperature of HABS, T_H, measured by the integrated thermocouple is read in real-time from an indicator[3] using a CCD camera. The values of T_H are limited to the range 1600 to 1800 °C to achieve a sufficient degree of dissociation of H_2 to H_1 (or cracking efficiency), η, while benefiting from a reduced W contamination of the sample and a relatively long lifetime of the HABS-filament. Current of 13.5 A or power about 150 W is required to achieve $T_\mathrm{H} = 1800\,^\circ\mathrm{C}$ (see figure 4.11). The pressure in the chamber is never allowed to exceed 5×10^{-6} mbar at any point of HABS operation. Prior to a cleaning procedure, the sample-heating coils are degassed above 700 °C for 10 min or until the chamber pressure stabilizes in the lower 10^{-9} mbar. The sample to be cleaned is then

---

[2] GEN750W | TDK-Lambda

[3] 2132i | Eurotherm

positioned along the capillary axis, with co-ordinates specified by scales on the rotary drive and the z-translator. The distance from the capillary orifice to the sample surface, d_S, is noted on the z-translator stroke. A pyrometer adjusted for emissivity values of 0.70 (polished GaAs) or 0.90 (oxidized Mo) measures the temperatures as the sample is brought to the cleaning temperature, T_S. It takes about 25 min until the sample achieves a uniform maximum temperature of 450 °C. Ideally, the HABS is always kept above 300 °C by passing ∼3 A to avoid the contamination of the source by residual gases in the HCC. Because of this practice, degassing of HABS is not required prior to AHC.

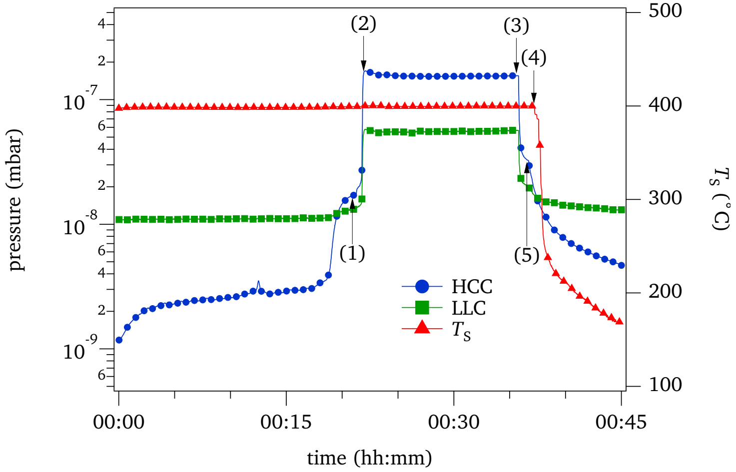

Figure 5.1: Pressure profiles in the HCC (circles) and LLC (squares) during an atomic-hydrogen cleaning process. The numbers in brackets indicate times when (1) the HABS reaches ≥1800 °C (2) H_2-valve open (3) H_2-valve closed (4) sample-heater off and (5) the HABS begins to cool. TMP in the LLC is used as a support pump. Triangles represent the temperature of the sample.

A quintessential pressure and temperature chart representing an AHC procedure is shown in figure 5.1. To begin a cleaning process, T_H is slowly raised to the operating temperature at a rate not exceeding $2\,°C\,min^{-1}$. When the chamber pressure stabilizes around 2×10^{-8} mbar, H_2 is leaked into the capillary until the chamber pressure reaches a specified value. Since below 1×10^{-5} mbar the pressure indication of the gauge in the HCC is linear for all measurable gas species, the pressure of molecular hydrogen in the chamber, p_{H_2}, can be calculated by multiplying the gauge reading by a given calibration constant equal to 2.4. The total hydrogen molecules entering the chamber is expressed in units of Langmuir (L), where 1 L corresponds to 1.3×10^{-6} mbar s of dosage. The total atomic-hydrogen dosage, D_{H_1}, is given as twice the product of corresponding degree of dissociation, η, and molecular hydrogen dosage, D_{H_2}. Knowing the effective pumping speed, S_{eff} , for H_2 in the chamber the molecular hydrogen flow rate, $\dot{Q}_{H_2}$, can be estimated. Hydrogen cracking efficiency of the HABS is a function of $\dot{Q}_{H_2}$ and T_W, and can be calculated using the formulas

$$\eta = \sqrt{\frac{K_p}{4\frac{p_{eq}}{p^0} + K_p}} \tag{5.1}$$

$$\log K_p = 6.304 - \frac{23760K}{T_W} \quad , \tag{5.2}$$

where T_W is the capillary temperature in Kelvin , K_p is an equilibrium constant, $p^0 = 1000$ mbar and p_{eq} represents the equilibrium pressure in a virtual-chamber, the value of which depends on $\dot{Q}_{H_2}$. Reference [172] has the values of p_{eq} tabulated for different feeding pressures. A typical AHC performed at Photo-CATCH has $T_H = (2074 \pm 5)$K, $\dot{Q}_{H_2} = (2.4 \pm 0.7) \times 10^{-4}$mbar l s^{-1}, and corresponding $\eta \approx (48 \pm 3)\%$. The dependence of the degree of dissociation on HABS temperature and flow rate is shown in figure 5.2.

As soon as HCC became operational, sample B1 was subjected to trial AHC experiments. Heat-cleaning to 450 °C for 1 hour and activation of the sample showed no photo-response. AHC was performed on B1 using typical values mentioned in the HABS user's manual. Following two consecutive AHCs with $D_{H_1} = 0.7$ kL, the sample progressively showed responses of 12 and 17 μA mW^{-1}, respectively. No attempts were made to optimize either the H_1 cleaning or the activation processes during these experiments. However, T_H, d_S and T_S were kept the same in all the treatments. These experiments solely served the purpose of familiarizing with the operation of HABS and the hydrogen cleaning process in general.

For the optimization of AHC, the sample B3 was chosen. This sample was deliberately contaminated by leaving it as a cold spot inside HCC during a bake-out. Initially, a heat-cleaning was performed at about 470 °C for 1 h and the cathode was activated to verify that the surface contamination was not removable by heat cleaning at this temperatur. This was confirmed by being unable to observe any photo-response from the activated sample. AHC was performed by keeping the parameters $d_S = (150.0 \pm 0.5)$ mm, $T_H = (1800 \pm 4)$ °C and $T_S = (400 \pm 1)$ °C constant,

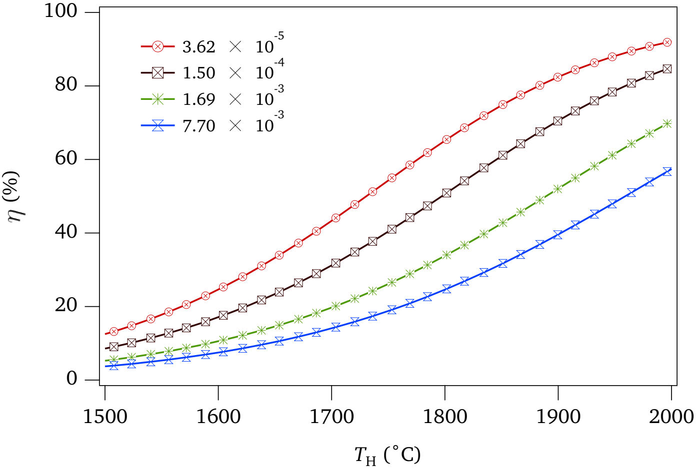

Figure 5.2: Simulated curves showing the dependence of hydrogen cracking efficiency of the HABS on its operating temperature and the flow rate of H_2. The legend shows values of $\dot{Q}_{H_2}$ in $\mathrm{mbar\,l\,s^{-1}}$. A combination of low flow rate and high temperature yields the maximum value for η.

and the exposure time, t_H, and p_{H_2} as variables. The sample was exposed successively to doses of (1.7 ± 0.1) kL, (2.6 ± 0.2) kL, and (5.9 ± 0.6) kL in experiments AHC 1, AHC 2 and AHC 3, respectively. The activation curve after each cleaning is compared to the standard activation curve of a fresh sample to decide if further cleaning is necessary. The results of these cleaning experiments are shown in figure 5.3. Gradual improvements in *QE* are seen after 10 min long AHC 1 and 15 min long AHC 2, and no change occurred after 30 min long AHC 3. From this observation, an upper limit of 10 kL for atomic-hydrogen dosage could be deduced. This amount of atomic hydrogen in HCC is sufficient to produce a surface comparable to fresh GaAs from a heavily contaminated sample.

Two features are noticeable in the activation diagrams in figure 5.3. First, the dirtier the surface, the longer it takes to reach the final *QE* for a particular activation. This is due to the fact that the contamination on the surface reduces the sticking coefficients for Cs and O_2 on GaAs. Second, the magnitude of the initial photocurrent peak corresponding to pure Cs adsorption on the surface depends on its cleanliness. It can be explained by reasoning that the contamination present on the surface poses its own potential barrier to the photoelectrons trying to make an escape. As the contamination is removed through reaction with H_1, this additional

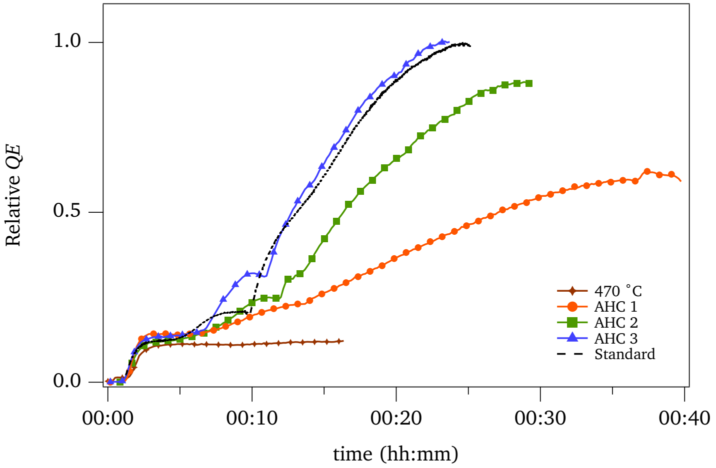

Figure 5.3: Quantum efficiency evolution of the sample B3 after a heat cleaning and repeated exposure to atomic-hydrogen. Dosages of (1.7 ± 0.1) kL [AHC 1], (2.6 ± 0.2) kL [AHC 2] and (5.9 ± 0.6) kL [AHC 3] are used for consecutive cleanings. Activation curve of the sample cleaned at (470 ± 1) °C can be seen to show no photo-response even after an exposure to Cs for more than 15 minutes. Comparison to the standard activation curve of a heat cleaned sample pronounces the difference in pure cesium response of an atomic-hydrogen cleaned sample.

barrier disappears and strong bonding of Cs on GaAs surface takes place resulting in a better reduction of the work function. It is also noted that, even though a cesium-response peak higher than the standard activation curve of a fresh sample is evident after AHC 3, the final *QE* of both the samples are comparable. This is expected since after NEA is achieved, all of the electrons excited to and thermalized in the conduction band have equal probability of escape for any similar samples.

The atomic-hydrogen beam formed by HABS capillary has an angular distribution of intensity about its axis. Figure 5.4 shows the distribution of both atomic and molecular hydrogen for an angular range of ±30° for $\dot{Q}_{H_2} = 8.5 \times 10^{-3}\,\mathrm{mbar\,l\,s^{-1}}$ and $T_S = 2070\,^{\circ}\mathrm{C}$ [171]. At the range of values HABS is usually operated, a distribution of a similar shape can be expected. For a particular set of parameters, the angular distribution of H_2 is narrower than the the atomic flux and the beam becomes narrower with decreasing of the feeding flux [172]. Without dedicated devices, it is not possible to quantify the absolute atomic-hydrogen flux impinging on the sample. However, a relation exists between the flux density of atomic-hydrogen, ϕ_{H_1}, and the distance, d_0, of the sample from the end of the capillary, which is given by

$$\phi_{\mathrm{H}_1} = \frac{J_0}{d_{\mathrm{S}}^2} \quad , \tag{5.3}$$

where J_0 is the on-axis intensity for a given $\dot{Q}_{\mathrm{H}_2}$ and T_{W}. Equation (5.3) can be used to calculate the relative flux on a sample at a different distance. Reducing d_{S} from 15 cm to 8 cm results in a 3.5 times higher ϕ_{H_1} on the sample due to geometry. This means that an exposure time 3.5 times lower is required to treat the sample to an equal amount of atomic-hydrogen flux. The relation between the exposure time and sample position is plotted in figure 5.5. Assuming an upper limit of dosage calculated before, it is possible to clean an equally contaminated sample at 8 cm away from the HABS's orifice with about 15 min of H_1 exposure.

The distance 8 cm is chosen for specific reasons: HABS has an Mo aperture plate used for limiting the beam to the sample proper to prevent hydrogen atoms from causing desorption by impinging on other equipments or walls of the chamber. This 6 mm aperture limits the beam to a 10 mm diameter sample surface area at 8 cm and is specifically designed considering the fact that the exposed area of the GaAs surface in the Mo-puck is 10 mm. Also, the second heating coil available for sample heating during AHC is located at about 8.5 cm from HABS orifice. To have a maximum sample heating efficiency for the minimum electrical-power on the coil, the sample has to stay as close to the coil as possible. For these reasons, 8 cm from the orifice is the optimum position for hydrogen cleaning of the samples in HCC.

The hydrogen cleaning process was optimized when only the SIP in HCC and TMP in LLC were available to pump the hydrogen in the chamber. SIP is known to release a good part of the hydrogen back into the chamber due to diffusion and the TMP has a low pumping speed for hydrogen which is diminished further by the poor conductance between HCC and LLC. As a consequence, pumping for long a time was required to bring HCC close to its base pressure after a cleaning process. To pump hydrogen more efficiently, a 400 $\mathrm{l\,s^{-1}}$ NEG pump added and is installed inside SIP. This arrangement ensures that the hydrogen released by the SIP is captured by NEG before it migrates to the chamber. The extra pump changed the effective pumping speed in the chamber for hydrogen[4] from 218 $\mathrm{l\,s^{-1}}$ to 498 $\mathrm{l\,s^{-1}}$. With this change, it is now possible to conduct a cathode cleaning at about 2.3 times lower chamber pressure, and it takes only about 2 h to reach l-UHV pressures between AHC cycles.

---

[4] SIP pumps hydrogen with double its nominal pumping speed.

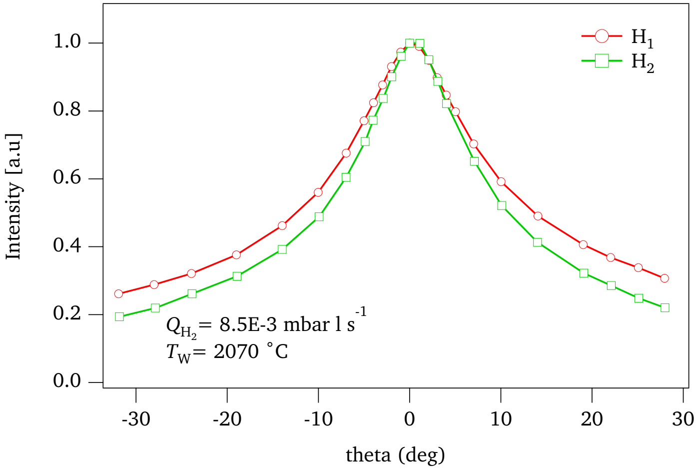

Figure 5.4: Typical intensity distribution of H_2 and H_1 in the beam formed by HABS. Data taken from reference [171].

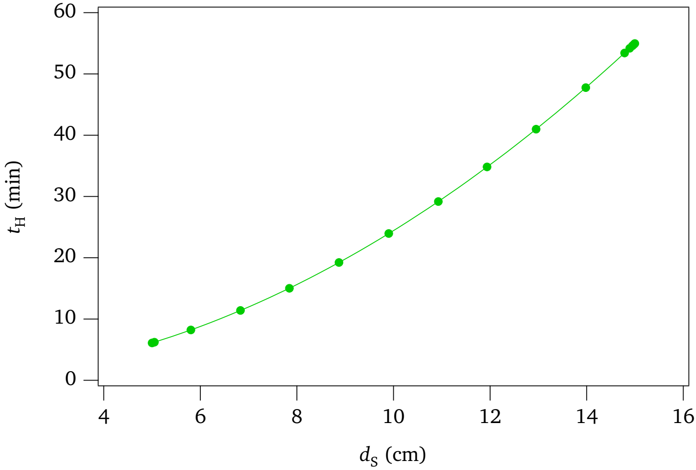

Figure 5.5: Variation of the time required for atomic-hydrogen cleaning with respect to the distance of the sample surface from HABS orifice.

The latest values used for routine hydrogen cleaning of activated samples stored in vacuum is tabulated in table 5.2. However, a proper cleaning of differently contaminated samples may require different amounts of H_1 dosage.

d_S (mm)	T_H (°C)	p_{H_2} (mbar)	T_S (°C)	t_H (min)
80.0 ± 0.5	1800 ± 4	$(5.0 \pm 1.5) \times 10^{-7}$	400 ± 1	10

Table 5.2: Parameters currently used for the atomic-hydrogen cleaning of GaAs samples at the Photo-CATCH.

From the cleaning experiments conducted with other samples, its has also been observed that the photocathodes, once atomic-hydrogen cleaned and activated to NEA, can be simply heat-cleaned at 550 °C to prepare it for re-activations. After repeated heat cleanings, an atomic-hydrogen cleaning can be applied to restore the surface to initial conditions of the cathode.

5.2 NEA activations

A dedicated LabVIEW interface is used for performing NEA activations. The set-up of the components and circuits involved is diagrammatically given in figure 5.6. The devices CPS07 and CPS10 supply current to Cs and Li dispensers and QM07[5] is an analogue-to-digital current converter with a resolution of 0.1 nA and maximum measurable current limit of 100 μA. It measures the photocurrent collected by a ring anode held at +102 V potential, where the usual range of photocurrent extracted during a an activation is 0.01 to 2 μA. The piezoelectric leak-valve voltage supply as well as a diode-laser module are driven by a commercial micro-controller unit[6]. The activation-interface has options for switching on and off, and adjusting the values of the photocurrent extraction limit, alkali-dispenser current, O_2 leak-valve voltage and intensity of the laser. A data file is generated by the programme that lists all of these values, in addition to the date and time data, photocurrent and pressure in the chamber. Using the calibration data for the laser modules, the *QE* is calculated and plotted in real time along with values of photocurrent and pressure. A snapshot

---

[5] CPS07, CPS10 and QM07 are produced in-house by the electronics workshop.

[6] Arduino® Due

of this graphical interface is shown in figure 5.7. The computer-controlled activation is a major improvement from the approach at the SPIN preparation facility, and offers better control over the parameters of the process.

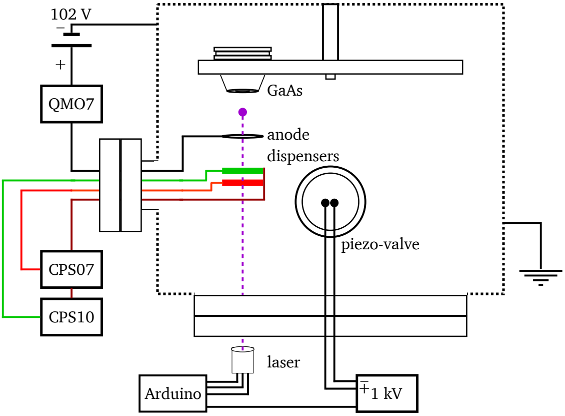

Figure 5.6: Diagram of the set-up used for activation experiments at Photo-CATCH. The current supplies CPS07 and CPS10, and the ammeter QM07 are connected to the EPICS server. The laser and leak-valve controllers are hooked to a local network through a USB server. The photocurrent is collected by the ring-shaped anode at +102 V with respect to the phtotocathode grounded via the vacuum chamber.

The laser modules are calibrated with a separate set-up, in which the laser power is measured through a borosilicate window using a power meter with a pre-calibrated photodiode-sensor[7]. The measured output power of laser modules of wavelength and maximum power (405 nm, 5 mW), (650 nm, 3 mW) and (780 nm, 2 mW), regulated via pulse-width modulation is shown in figure 5.8. The abrupt jumps in output power appear consistently, and are an attribute of the modulating signal. Typically, laser powers in the range of 2 to 8 μW are used during activation experiments.

A successful Co-De activation maintains a constant growth of the photocurrent up until its peak, if adequate amounts of Cs and O_2 are constantly supplied. It is perceptible that a good Co-De recipe would have a special ratio between the Cs and the O_2 fluxes, which would keep a continuous growth of current until the end of the process. Several activation experiments were carried out using a freshly cleaved

---

[7] PM100D with S150C | Thorlabs

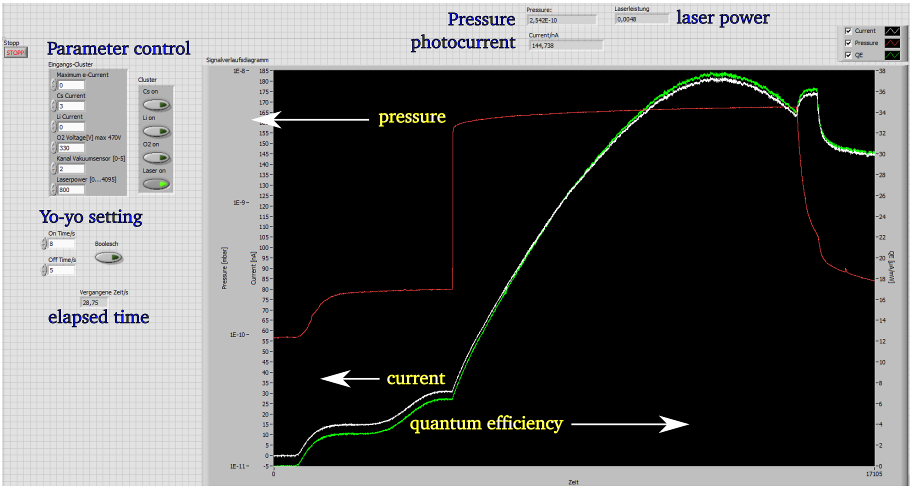

Maximum e-Current: 0
Cs Current: 3
Li Current: 0
O2 Voltage[V] max 470V: 330
Kanal Vakuumsensor [0-5]: 2
Laserpower [0…4095]: 800
On Time/s: 8
Off Time/s: 5
Vergangene Zeit/s: 28,75
Pressure: 2,542E-10
Current/nA: 144,738
Laserleistung: 0,0048

Figure 5.7: The interface used for controlling and monitoring the photocathode activation process.

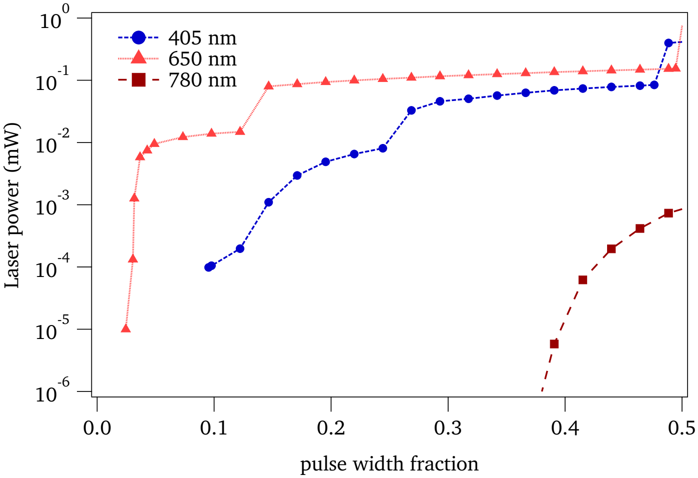

Figure 5.8: Calibration curves of pulse-width modulated diode-laser modules. The laser at 405 nm is used for all the activation experiments reported in this dissertation. The pulse is divided into a total of 4095 parts. Power used for extracting the photocurrent during activation is between 2 and 8 μW.

sample, B2, to examine the influence of such a ratio on the NEA layer formation. Since an optimized AHC was not in place for cleaning the sample surface after its introduction from atmospheric conditions, *in-situ* heat cleaning at 600 °C was employed prior to its first activation. Thereafter, subsequent activations were done on a hydrogen cleaned sample at 450° with an overdose of hydrogen (about 4 kL at 8 cm) which produced clean surfaces that achieved similar QE as in the heat-cleaned trial. Before each activation, it was made sure that no remnant NEA photoemission is present on the sample even at the full power (5 mW) of the laser.

At an excitation wavelength of 405 nm, it is reasonable to expect quantum efficiencies amounting to 10-15% from bulk NEA-GaAs photocathodes, which is equal to collecting a photocurrent of 35 to 50 $\mathrm{nA\mu W^{-1}}$. This criteria is used in all the activation experiments to determine whether an activation was successful. The ratio, $r = p_{\mathrm{Cs}}/p_{\mathrm{O_2}}$, is defined as the main parameter to be optimized in Co-De procedure, where p_{Cs} and $p_{\mathrm{O_2}}$ are the pressures of Cs and O_2 as measured by the ionization gauge in the CAC. Varying this parameter, several Co-De activations were performed with the sample B2. Selected results from these experiments are shown in figure 5.9. Examining the curves (1), (3) and (5), it became clear that as the ratio r increases, the final quantum efficiency decreases. Curve (4) emphasizes the importance of controlling the value of r for a successful Co-De activation. It needs to be mentioned that even though the part of curve (4) with $r = (0.038 \pm 0.002)$ has a higher slope, this is evidently due to the compensation of O_2 by Cs from the first part where r was equal to (0.075 ± 0.005). This supposition was justified by observing that the activation of sample with $r = (0.038 \pm 0.002)$ at the same fluxes proceeds too slow for practical purposes.

Another important feature of the curves in figure 5.9 is that the pace of QE growth increases considerably with increasing the absolute flux of Cs and O_2. On one hand, with $p_{\mathrm{Cs}} = 9.3 \times 10^{-11}$ mbar, curve (1) exhibits a constant but rather slow formation of the NEA layer on the surface, reaching its plateau in about 45 minutes resulting in the highest QE of all the curves. On the other hand, curves (2) and (3) with p_{Cs} of 2×10^{-10} mbar and 2.1×10^{-10} mbar, respectively, and with an r close to that of curve (1) reached the peak in 22.5 minute and 25 minute, respectively. The lower QE achieved by these activations is due to a higher r as discussed before. Curve (5), which was given the highest Cs flux can be seen to reach its QE peak in less than 15 minute, with a poor QE owing to the highest ratio.

These observations are sufficient to draw the conclusion that a good Co-De activation at Photo-CATCH must posses r close to 0.043 and fluxes of Cs and O_2 should

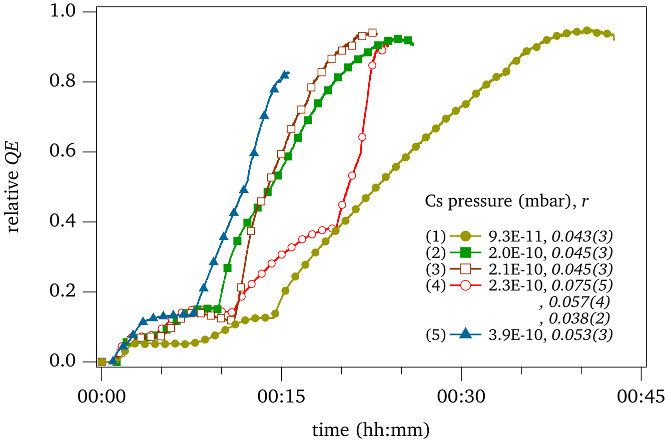

Figure 5.9: Co-De activation curves obtained by manipulating the Cs/O_2 ratio and absolute fluxes. The ratio used for each curve are given in the boxes, and the initial Cs pressures are given in the legend. Boxes and curves are color coded and are attached to the respective curves. The curve (3) has three different ratios corresponding to the three different slopes of photocurrent growth.

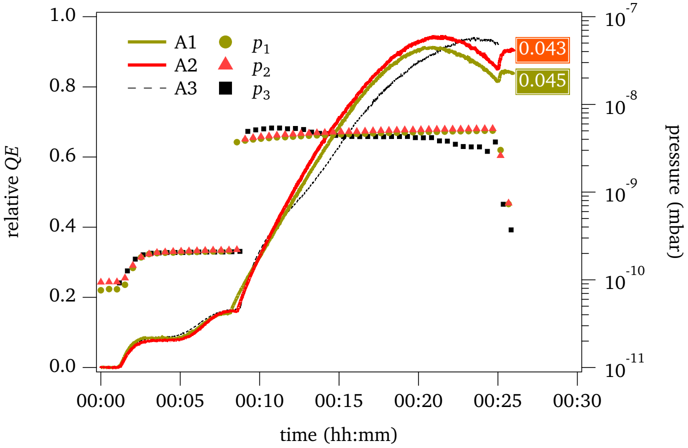

Figure 5.10: Digram of activations performed after optimization of the parameters. Variations in r and O_2 flux are notable in the final quantum efficiencies and in the shapes of the curves.

be kept to sufficient amount in order to achieve the final QE in a required time. To test this proposition, activations were performed with predefined values for p_{Cs} and $p_{\mathrm{O_2}}$ and aiming for the ratio 0.043. The diagrams obtained from two of these activations are shown in figure 5.10. Slight deviations from the intended ratio is inevitable due to variations in flow-rates from the piezoelectric valve. However identical growth patterns (curves A1 and A2) could be accomplished by using almost the same initial values. Curve A3 is added to show the influence of oxygen flow-rate deviation on the pattern. The final QEs are different as expected due to the difference in r value of the curves. Parameters extracted from these studies, as given in table 5.3, are used to optimize AHC using sample B3.

A higher QE than that obtained from the Co-De activations is frequently reported by laboratories which use Nagoya activation (Na-Ac) method. This possibility is investigated at Photo-CATCH using the samples S1 and B5. Na-Ac proceeds by first achieving the photoresponse by deposition of Cs, growing it to a new peak with oxygen and bringing it down to zero by over-cesiation. This process is repeated until no improvement in photocurrent is observed, and the activation is ended in the usual way by slightly over cesiating the cathode. Na-Ac can definitely surpass Co-De as the activation methods for photocathodes used at Photo-CATCH and SPIN. The advantage of not requiring to subtly balance p_{Cs} and $p_{\mathrm{O_2}}$ to produce a high quality NEA layer makes activating GaAs cathodes an easy task to perform.

In order to achieve even higher quantum efficiencies, a two-stage activation can be performed by following an *activation-annealing-activation* procedure. This has been studied using the sample S1 and the best of the activation diagrams is shown in figure 5.11. In this experiment, S1 was activated to its maximum photoresponse by Co-De, and annealed at 520 °C for 40 min. After cooling down the sample, a Nagoya-type activation is performed to reach a new QE peak. About 25% increase of QE over what is obtained by a single Na-Ac is achieved by the two-stage method.

I_{Cs} (A)	$V_{\mathrm{O_2}}$ (V)	p_{Cs} (mbar)	$p_{\mathrm{O_2}}$ (mbar)	t_1 (min)	t_1 (min)	t_1 (min)
3	380	$\sim 2.1 \times 10^{-10}$	$\sim 5 \times 10^{-9}$	3	8	25

Table 5.3: parameters for an optimum Co-De activation of bulk-GaAs photocathodes at Photo-CATCH.

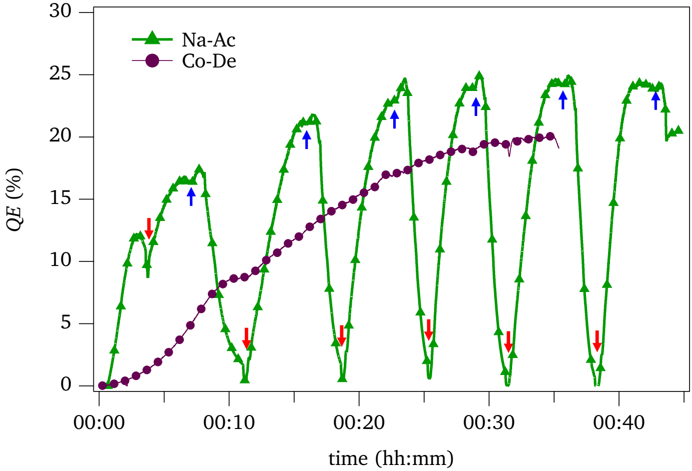

Figure 5.11: Activation diagrams resulting from Nagoya and Co-De activations of the sample S1. The down-arrows (red) indicate where Cs was switched off and O_2 was flown in and the up-arrows (blue) represent the reverse.

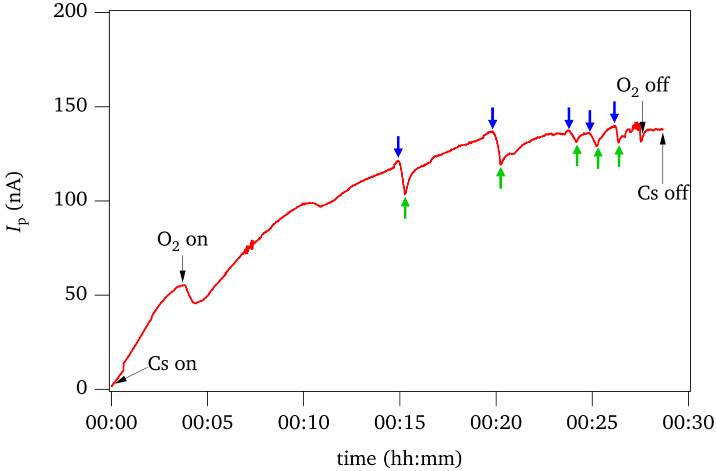

Figure 5.12: Activation diagram of an NEA activation with Cs, Li and O_2. the down-arrows (blue) indicate the point where lithium was introduced and the up-arrows (green) show when it was turned off.

Including lithium in the activation process has the ability to make the NEA layer resistant to the attack from residual gases [137]. The recipe for (Cs,Li,O_2) activation is completely empirical and could only be achieved through trial and error. Most of the activations performed at Photo-CATCH with Cs, Li and O_2 ended up resulting in poor final *QE* of the cathode, where a slight increase in *QE* is actually expected following a proper activation. After several tries, an activation that preserved the final *QE* was performed. The diagram resulted from this activation is shown in figure 5.12. Elaborate experiments in this direction were not possible due to the occurrence of a conflict between the controls of the CPS07 and CPS10 current supplies which is currently being resolved. Finally, a comparison of the best results obtained from different activations on different cathodes are presented in figure 5.13. The results show that the achievable *QE* follows the order two-stage > Na-Ac > Co-De.

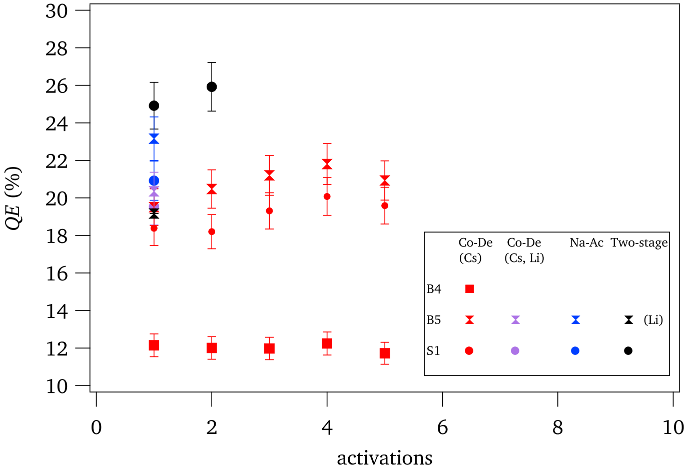

Figure 5.13: Coparison of quantum efficiencies resulted from different types of activations on three different photocathode samples.

5.3 Lifetimes studies

The behaviour of all GaAs photocathodes activated to NEA follows a pattern of *QE* evolution, similar to that in figure 3.11. Soon after an activation, the photocathode begins to recover the lost *QE* due to the over-cesiation at the termination of the process. After a saturation point, the QE stays stable for a while before starting its decay. A programme different from the activation-interface was used for monitoring this behaviour of the activated photocathodes stored in the CAC. The photocurrent was measured intermittently by turning the laser on for a fixed duration (typically 1 s). The programme takes data at a predefined time interval and stores it in a file. The lifetime of a an activated cathode in the same chamber where it is just prepared is expected to be very low due to the presence of a high amount of oxygen remaining in the chamber after the activation process. The oxygen pressure in CAC after an activation process usually reaches below 1×10^{-10} mbar within 2.5 to 3 hour which is, however, long enough to degrade the NEA layer almost completely (see figure 3.12). Nevertheless, lifetime studies are conducted in the CAC to have an estimate of the lifetimes of the cathodes in this chamber. Such an estimate is useful to determine the duration up to which an activated cathode can be kept inside the preparation chamber before its transfer to the electron-gun. An improvement of this time span can open the possibility of activating and storing multiple cathodes in CAC for quick replacement of used cathodes in the electron-gun.

To verify if oxygen in the chamber at pressures below 1×10^{-10} mbar is indeed detrimental to QE, lifetime measurements at different oxygen pressures were made on samples undergone identical activation. Oxygen is leaked into the chamber at a fixed rate using the piezoelectric leak valve and the pressure is maintained at a constant value. The result of this investigation is shown in figure 5.14. A correlation between the decay rate and oxygen pressure is clearly seen. It is possible to conclude that even at an oxygen pressure of 3×10^{-11} mbar the decay is enhanced. Since 1.8×10^{-11} mbar is the lowest pressure measured in the CAC thus far, it is logical to assume that a lifetime of more than about 100 hours will be difficult to achieve for the photocathodes saved in this chamber. It could also be said that the lifetimes observed in the activation chamber cannot be directly comparable to what maybe achieved in a properly baked out XHV electron-gun chamber that has a pressure below 5×10^{-12} mbar and hydrogen is the most prominent component of the residual gas. At this pressure the partial pressures of oxygen and other oxygen-containing species are usually less than 1×10^{-14} mbar. On similar grounds, a comparison of the lifetimes of different samples activated using different types of procedures, where different doses of oxygen are used, is also incompatible.

Activations of S1 with $Cs+O_2$ and $Cs+O_2+Li$ have used similar oxygen doses and thence reached comparable base pressures of the chamber in same amount of time. Therefore the lifetime measurements of these two experiments could be compared to see if adding Li has improved the lifetime of the cathode. Figure 5.15 shows a

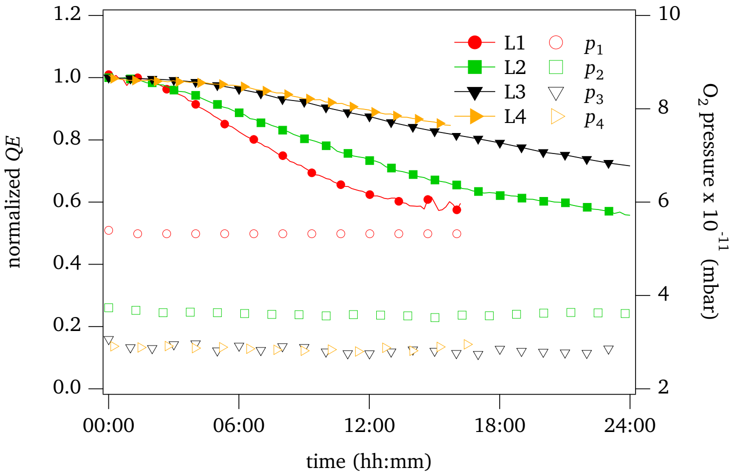

Figure 5.14: Oxygen induced *QE* degradation curves of the sample S1. Variation in the rate of degradation with varying oxygen pressure in the chamber is clearly seen.

comparison of the degradation curves. Contrary to expectations, no difference in the rate of degradation is observed at a chamber pressure of $\sim 3 \times 10^{-11}$ mbar. More experiments with increased oxygen pressure will be able to magnify any minute differences in the immunity of NEA layer, if at all present.

It was assumed that annealing the sample after Li deposition could help the Li atoms redistribute and may arrange themselves in appropriate sites in the NEA layer. Based around this idea, a different approach for incorporating Li in the NEA layer is tried. A two-stage activation is performed by first activating the cathode B5 with Cs+O_2+Li following the recipe given in figure 5.12. Then the sample is annealed at 515 °C and activated again by Na-Ac using only Cs and O_2. The *QE* achieved by this method and the lifetime decay of the sample are given in figure 5.16. Although the final quantum efficiency was lower than what was achieved by a single Co-De activation with the same sample, the new procedure resulted in a lifetime of 298±36 hours, the highest that has been measured so far in the CAC. This indicates that a much better lifetime could expected in a XHV chamber for GaAs photocathodes activated by (Cs,Li,O_2)–(Cs,O_2) two stage activation.

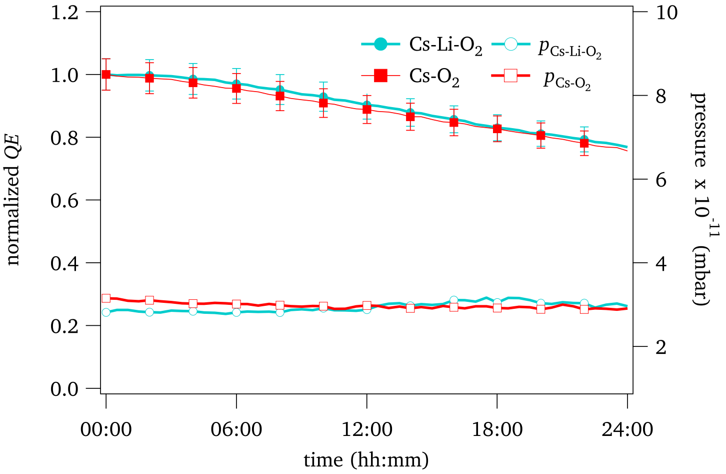

Figure 5.15: Comparison of *QE* degradation curves of a sample activated with Cs+O_2 and Cs+O_2+Li.

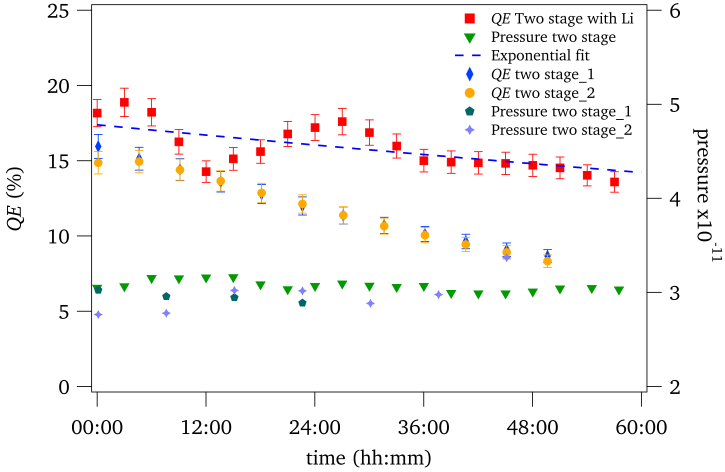

Figure 5.16: Comparison of lifetime evolution of a sample activated using the standard two-stage and (Cs+O_2+Li)-(Cs+O_2) activations.

6 Summary and outlook

In this work, reasons for the optimization of photocathode preparation techniques to improve the *QE* and lifetimes of GaAs based semiconductor photocathodes used at the spin-polarized electron injector SPIN at S-DALINAC were addressed. Research was aimed at basic understanding of the NEA activation procedure can result in photocathodes capable of high-current applications. The improvement of vacuum conditions in the electron-gun chamber was realized to better the vacuum and operational lifetimes of cathodes. To this end, the test stand Photo-CATCH was constructed.

A standardized activation procedure was defined and employed, and the surface cleaning of photocathodes at low-temperatures using atomic hydrogen produced by a thermal cracking cell was investigated. Parameters corresponding to an optimum cleaning of heavily contaminated GaAs sample have been optimized. Using the values extracted, repeated cleaning of GaAs samples has been accomplished. Different types of activations have been studied to find the best activation recipe. The ratio of fluxes is analyzed, and the optimum values are extracted for the co-deposition method using cesium and oxygen. Based on the findings, a reproducible activation procedure controlled via a computer-interface has been developed. The yo-yo type Nagoya activation with cesium and oxygen was used to activate the photocathodes to high quantum efficiencies. Significant improvement in final quantum efficiency, exceeding 26% for 405 nm excitation wavelength, could be demonstrated using a two-stage activation procedure. Through the comparison of different types of activations, the best method has been identified for GaAs photocathodes for high-current operation at S-DALINAC. The effect of very low partial pressures of oxygen on the vacuum lifetime was investigated by monitoring cathodes at steady flow-rates of oxygen. Co-deposition of lithium during NEA activation has been applied, but no improvement in photocathode lifetime has been observed so far. However, a novel two-stage activation recipe involving lithium, cesium and oxygen has been tested and found to produce an NEA cathode with about four times the lifetime usually observed in the preparation chamber using other recipes.

With the design of a vacuum-suitcase conceived in this dissertation, a long-term storage of hydrogen-cleaned photocathode samples under UHV conditions to suppress native oxide formation will become available. It would also enable the transfer of samples between Photo-CATCH and SPIN. As an upgrade to the cleaning system, a sample heating-stage can be devised. In this way, a precise control of the sample temperature can be achieved, and anomalies in the temperature measurement with the pyrometer due to background radiation can be avoided. This would also exclude heating of other parts of the system as in the case of radiative heating using bare coils, and can consequently reduce thermally induced outgassing and desorption of adsorbed gases. To improve the charge lifetime of the photocathodes, the method of selective NEA activation of a small surface area of the cathode with a suitable sample-mask [207] needs to be implemented. Measuring the feeding pressure using an appropriate vacuum-gauge between the leak valve and the HABS will help to optimize the atomic-hydrogen cleaning process more quantitatively. Using the available supercontinuum light-source, an exploration of wavelength dependent characteristics of photocathodes may become possible. With the high-voltage source and the Mott-polarimeter in operation, a systematic study of the impact of atomic-hydrogen cleaning on the polarized-emission from lattice-strained photocathodes could encourage further optimization of the cleaning process. Development of high-performance photocathodes can be beneficial to experiments suing high-brightness, ultra-low emittance electron beams for cooling relativistic ion beams, for e.g. at the future FAIR complex [208].

Bibliography

[1] T. Christian. Review of electron guns. In *Fourth European Particle Accelerator Conference (EPAC)*, pages 317–321, 1994.

[2] M. F. M. Iqbal, G. Islam and Z. Zhou. Electron beam guns for high energy electron accelerators: An overview. *J. Mod. Phys.*, 4(11):1536–1539, 2013.

[3] A. Todd. State-of-the-art electron guns and injector designs for energy recovery linacs (ERL). *Nucl. Instruments Methods Phys. Res. Sect. A: Accel. Spectrometers, Detect. Assoc. Equip.*, 557(1):36–44, 2006.

[4] C. K. Sinclair. DC photoemission electron guns as ERL sources. *Nucl. Instruments Methods Phys. Res. Sect. A: Accel. Spectrometers, Detect. Assoc. Equip.*, 557(1):69–74, 2006.

[5] A. Arnold and J. Teichert. Overview on superconducting photoinjectors. *Phys. Rev. ST Accel. Beams*, 14(2):024801, 2011.

[6] R. Xiang, A. Arnold, M. Freitag, et al. Research activities on photocathodes for HZDR SRF gun. In *International Particle Accelerator Conference (IPAC)*, pages 1524–1526, 2012.

[7] A. Richter. Operational experience at the S-DALINAC. In *Proc. of the 5th EPAC, Sitges*, page 110, 1996.

[8] Y. Poltoratska, C. Eckardt, W. Ackermann, et al. Status and recent developments at the polarized-electron injector of the superconducting Darmstadt electron linear accelerator S-DALINAC. *J. Physics: Conf. Ser.*, 298(1):012002, 2011.

[9] C. Eckardt, R. Barday, J. Enders, et al. Polarized Eletrons for Experiments at Low Momentum Transfer SPIN@ S-DALINAC. *Proc. 18th SPIN*, page 919, 2008.

[10] J. Enders, T. Bahlo, P. Bangert, et al. Reactions with polarized electrons and photons at low momentum transfers at the superconducting Darmstadt electron linear accelerator S-DALINAC. *J. Physics: Conf. Ser.*, 295(1):012152, 2011.

[11] J. Enders. Ideas for fundamental electron scattering at the S-DALINAC. *AIP Conf. Proc.*, 1563(1):223–226, 2013.

[12] D. T. Pierce, R. J. Celotta, G.-C. Wang, et al. The GaAs spin polarized electron source. *Rev. Sci. Instruments*, 51(4):478–499, 1980.

[13] G. D. Cates, V. W. Hughes, R. Michaels, et al. The BATES polarized electron source. *Nucl. Instruments Methods Phys. Res. Sect. A: Accel. Spectrometers, Detect. Assoc. Equip.*, 278(2):293–317, 1989.

[14] R. Alley, H. Aoyagi, J. Clendenin, et al. The Stanford linear accelerator polarized electron source. *Nucl. Instruments Methods Phys. Res. Sect. A: Accel. Spectrometers, Detect. Assoc. Equip.*, 365(1):1 – 27, 1995.

[15] K. Aulenbacher, C. Nachtigall, H. Andresen, et al. The MAMI source of polarized electrons. *Nucl. Instruments Methods Phys. Res. Sect. A: Accel. Spectrometers, Detect. Assoc. Equip.*, 391(3):498–506, 1997.

[16] T. Rao, A. Burrill, X. Chang, et al. Photocathodes for the energy recovery linacs. *Nucl. Instruments Methods Phys. Res. Sect. A: Accel. Spectrometers, Detect. Assoc. Equip.*, 557(1):124 – 130, 2006.

[17] J. Zou, B. Chang, Z. Yang, et al. Stability and photoemission characteristics for GaAs photocathodes in a demountable vacuum system. *Appl. Phys. Lett.*, 92(17):172102, 2008.

[18] D. A. Orlov, F. Sprenger, M. Lestinsky, et al. Photocathodes as electron sources for high resolution merged beam experiments. *J. Physics: Conf. Ser.*, 4(1):290–295, 2005.

[19] C. K. Sinclair, P. A. Adderley, B. M. Dunham, et al. Development of a high average current polarized electron source with long cathode operational lifetime. *Phys. Rev. ST Accel. Beams*, 10(3):023501, 2007.

[20] J. B. Murphy. Energy recovery linacs light sources: an overview. In *Particle Accelerator Conference PAC, 2003*, volume 1, pages 176–180, 2003.

[21] L. Merminga, D. R. Douglas, and G. A. Krafft. High-current energy-recovering electron linacs. *Annu. Rev. Nucl. Part. Sci.*, 53(1):387–429, 2003.

[22] V. N. Litvinenko, I. Ben-Zvi, D. Kayran, et al. Potential uses of ERL-Based γ-Ray sources. *IEEE Transactions on Plasma Sci.*, 36(4):1799–1807, 2008.

[23] A. Brachmann, J. E. Clendenin, E. Garwin, et al. The ILC Polarized Electron Source. In *Proceedings of the 2005 Particle Accelerator Conference*, pages 3420–3422, 2005.

[24] D. Durek, F. Frommberger, T. Reichelt, et al. Degradation of a gallium-arsenide photoemitting NEA surface by water vapour. *Appl. surface science*, 143(1):319–322, 1999.

[25] N. Chanlek, J. D. Herbert, R. M. Jones, et al. The degradation of quantum efficiency in negative electron affinity GaAs photocathodes under gas exposure. *J. Phys. D: Appl. Phys.*, 47(5):055110, 2014.

[26] S. Pastuszka, A. Terekhov, and A. Wolf. 'Stable to unstable' transition in the (Cs, O) activation layer on GaAs (100) surfaces with negative electron affinity in extremely high vacuum. *Appl. Surf. Sci.*, 99(4):361 – 365, 1996.

[27] Y. Sun, R. E. Kirby, T. Maruyama, et al. The surface activation layer of GaAs negative electron affinity photocathode activated by Cs, Li, and NF_3. *Appl. Phys. Lett.*, 95(17):174109, 2009.

[28] M. Espig. Entwicklung, Aufbau und Charakterisierung einer variabel repetierenden, spinpolarisierten Elektronenkanone mit invertierter Isolatorgeometrie. Doctoral Dissertation D-17, Technische Universität Darmstadt, 2016.

[29] J. Auerhammer, H. Genz, H.-D. Gräf, et al. The S-DALINAC facility - operational experience from the accelerator and the experimental installations. *Nucl. Phys. A*, 553(C):841 – 844, 1993.

[30] D. Husmann. Review of CW Electron Machines. In *Fourth European Particle Accelerator Conference (EPAC)*, pages 62–66, 1994.

[31] J. O'Brien, D. Sober, L. Fagg, et al. Design and testing of apparatus for 180° electron scattering at low momentum-transfer. *Nucl. Instruments Methods Phys. Res. Sect. A: Accel. Spectrometers, Detect. Assoc. Equip.*, 312(3):531 – 541, 1992.

[32] T. Walcher, R. Frey, H.-D. Gräf, et al. High resolution electron scattering facility at the Darmstadt linear accelerator (DALINAC). *Nucl. Instruments Methods*, 153(1):17 – 28, 1978.

[33] D. Savran, K. Lindenberg, J. Glorius, et al. The low-energy photon tagger NEPTUN. *Nucl. Instruments Methods Phys. Res. Sect. A: Accel. Spectrometers, Detect. Assoc. Equip.*, 613(2):232 – 239, 2010.

[34] L. Schnorrenberger, K. Sonnabend, J. Glorius, et al. Nuclear astrophysics with tagged photons: NEPTUN@S-DALINAC, Darmstadt. *J. Physics: Conf. Ser.*, 202(1):012027, 2010.

[35] K. Sonnabend, D. Savran, J. Beller, et al. The Darmstadt High-Intensity Photon Setup (DHIPS) at the S-DALINAC. *Nucl. Instruments Methods Phys. Res. Sect. A: Accel. Spectrometers, Detect. Assoc. Equip.*, 640(1):6 – 12, 2011.

[36] B. Alikhani, A. Givechev, A. Heinz, et al. Compton polarimetry with a 36-fold segmented HPGe-detector of the AGATA-type. *Nucl. Instruments Methods Phys. Res. Sect. A: Accel. Spectrometers, Detect. Assoc. Equip.*, 675:144 – 154, 2012.

[37] M. Arnold. Doctoral Dissertation D-17, Technische Universität Darmstadt, In preparation, 2016.

[38] H. Homeyer and C. Petit-Jean-Genaz. Operational Experience and Results from the S-DALINAC. In *Third European Particle Accelerator Conference, EPAC92, Berlin, Germany*, volume 1, pages 49–51, 1992.

[39] T. Kürzeder, J. Conrad, F. Hug, et al. Development and test of a new cryostat module for the injector of the S-DALINAC. In *Proceedings of SRF2013, Paris, France*, pages 334–336, 2013.

[40] F. Hug, C. Burandt, J. Conrad, et al. Operational findings and upgrade plans on the superconducting electron accelerator S-DALINAC. In *Proc. of PAC, New York, NY, USA*, pages 1999–2001, 2011.

[41] M. Kleinmann, J. Conrad, R. Eichhorn, et al. CW energy upgrade of the superconducting electron accelerator S-DALINAC. In *Proceedings of the IPAC'12, New Orleans, USA*, pages 1161–1163, 2012.

[42] C. Heßler. Konzeption, Aufbau und Test einer Quelle spinpolarisierter Elektronen für den superleitenden Darmstädter Elektronenlinearbeschleuniger. Doctoral Dissertation D-17, Technische Universität Darmstadt, 2008.

[43] C. Eckardt, T. Bahlo, P. Bangert, et al. Implementation of a polarized electron source at the S-DALINAC. In *Proceedings of the IPAC'10, Kyoto, Japan*, page 4083, 2010.

[44] M. Salomaa and H. Enge. Velocity selector for heavy-ion separation. *Nucl. Instruments Methods*, 145(2):279 – 282, 1977.

[45] Y. Poltoratska. Design and setup of a compact Mott polarimeter for the future S-DALINAC polarized injector. Diploma Thesis, Technische Universität Darmstadt and Karazin Kharkiv National University (unpublished), 2005.

[46] V. Tioukine and K. Aulenbacher. Operation of the MAMI accelerator with a Wien filter based spin rotation system. *Nucl. Instruments Methods Phys. Res. Sect. A: Accel. Spectrometers, Detect. Assoc. Equip.*, 568(2):537 – 542, 2006.

[47] N. F. Mott. The scattering of fast electrons by atomic nuclei. *Proc. Royal Soc. Lond. Ser. A, Containing Pap. a Math. Phys. Character*, pages 425–442, 1929.

[48] T. J. Gay and F. Dunning. Mott electron polarimetry. *Rev. scientific instruments*, 63(2):1635–1651, 1992.

[49] F. Dunning. Mott electron polarimetry. *Nucl. Instruments Methods Phys. Res. Sect. A: Accel. Spectrometers, Detect. Assoc. Equip.*, 347(1):152 – 160, 1994.

[50] J. R. Pierce. Rectilinear electron flow in beams. *J. Appl. Phys.*, 11(8):548–554, 1940.

[51] B. Zwecker. A position stabilized Titan:Sapphire-Laser transfer for the polarized electron source at the S-DALINAC. Master Thesis, Technische Universität Darmstadt (unpublished), 2011.

[52] J. Lindemann. Construction and development of a Stokes-Polarimeter. Bachelor Thesis, Technische Universität Darmstadt (unpublished), 2011.

[53] Y. Fritzsche. Aufbau und Inbetriebnahme einer Quelle polarisierter Elektronen am supraleitenden Darmstädter Elektronenlinearbeschleuniger S-DALINAC. Doctoral Dissertation D-17, Technische Universität Darmstadt, 2011.

[54] T. Maruyama, D.-A. Luh, A. Brachmann, et al. Atomic hydrogen cleaning of polarized GaAs photocathodes. *Appl. Phys. Lett.*, 82(23):4184–4186, 2003.

[55] K. Togawa, T. Nakanishi, T. Baba, et al. Surface charge limit in NEA superlattice photocathodes of polarized electron source. *Nucl. Instruments Methods Phys. Res. Sect. A: Accel. Spectrometers, Detect. Assoc. Equip.*, 414(2–3):431 – 445, 1998.

[56] T. Van Buuren, M. K. Weilmeier, I. Athwal, et al. Oxide thickness effect and surface roughening in the desorption of the oxide from GaAs. *Appl. Phys. Lett.*, 59(4):464–466, 1991.

[57] C. Schwebler. Einfluss der verschiedenen Aktivierungsmethoden auf die Lebensdauer der GaAs Photokathode. Bachelor Thesis, Technische Universität Darmstadt (unpublished), 2015.

[58] M. Breidenbach, M. Foss, J. Hodgson, et al. An inverted-geometry, high voltage polarized electron gun with UHV load lock. *Nucl. Instruments Methods Phys. Res. Sect. A: Accel. Spectrometers, Detect. Assoc. Equip.*, 350(1):1–7, 1994.

[59] P. Adderley, J. Clark, J. Grames, et al. Load-locked dc high voltage GaAs photogun with an inverted-geometry ceramic insulator. *Phys. Rev. Special Top. Beams*, 13(1):010101, 2010.

[60] V. Apalin, I. Kutikov, I. Lukashevich, et al. Asymmetry in double Mott electron scattering for energies from 45 to 245 keV. *Nucl. Phys.*, 31:657 – 663, 1962.

[61] S. Mayer, T. Fischer, W. Blaschke, et al. Calibration of a Mott electron polarimeter: Comparison of different methods. *Rev. Sci. Instruments*, 64(4):952–957, 1993.

[62] W. E. Spicer. Photoemissive, photoconductive, and optical absorption studies of alkali-antimony compounds. *Phys. Rev.*, 112(1):114–122, 1958.

[63] W. E. Spicer. Photoemission and related properties of the alkali-antimonides. *J. Appl. Phys.*, 31(8):2077–2084, 1960.

[64] C. N. Berglund and W. E. Spicer. Photoemission studies of copper and silver: Theory. *Phys. Rev.*, 136(4A):A1030–A1044, 1964.

[65] C. N. Berglund and W. E. Spicer. Photoemission studies of copper and silver: Experiment. *Phys. Rev.*, 136(4A):A1044–A1064, 1964.

[66] A. Einstein. Concerning an heuristic point of view toward the emission and transformation of light. *Am. J. Phys.*, 33(5):367, 1965.

[67] J. Pendry. Theory of photoemission. *Surf. Sci.*, 57(2):679 – 705, 1976.

[68] M. Glasser and A. Bagchi. Theories of photoemission from metal surfaces. *Prog. Surf. Sci.*, 7(3):113 – 148, 1976.

[69] N. A. Soboleva. A new class of electron emitters. *Sov. Phys. Uspekhi*, 16(5):726–738, 1974.

[70] W. Spicer and R. Bell. The III-V photocathode: A major detector development. *Publ. Astron. Soc. Pac.*, 84(497):110–122, 1972.

[71] W. Spicer. Negative affinity 3–5 photocathodes: Their physics and technology. *Appl. physics*, 12(2):115–130, 1977.

[72] C. D. Thurmond. The standard thermodynamic functions for the formation of electrons and holes in Ge, Si, GaAs , and GaP. *J. The Electrochem. Soc.*, 122(8):1133–1141, 1975.

[73] H. Ehrenreich. Band structure and electron transport of GaAs. *Phys. Rev.*, 120(6):1951–1963, 1960.

[74] J. P. Walter and M. L. Cohen. Calculation of the reflectivity, modulated reflectivity, and band structure of GaAs, GaP, ZnSe, and ZnS. *Phys. Rev.*, 183(3):763–772, 1969.

[75] M. Cardona, N. E. Christensen, and G. Fasol. Relativistic band structure and spin-orbit splitting of zinc-blende-type semiconductors. *Phys. Rev. B*, 38(3):1806–1827, 1988.

[76] J. Blakemore. Semiconducting and other major properties of gallium arsenide. *J. Appl. Phys.*, 53(10):R123–R181, 1982.

[77] V. M. Goldschmidt. Crystal structure and chemical constitution. *Trans. Faraday Soc.*, 25:253–283, 1929.

[78] V. Glazov, A. Malkova, L. Pavlova, et al. The heat capacity of solid gallium arsenide. *Russ. J. Phys. Chem.*, 74(2):145–149, 2000.

[79] B. Goldstein, D. J. Szostak, and V. S. Ban. Langmuir evaporation from the (100), (111A), and (111B) faces of GaAs. *Surf. Sci.*, 57(2):733 – 740, 1976.

[80] C. Foxon, J. Harvey, and B. Joyce. The evaporation of GaAs under equilibrium and non-equilibrium conditions using a modulated beam technique. *J. Phys. Chem. Solids*, 34(10):1693 – 1701, 1973.

[81] H. R. Philipp and H. Ehrenreich. Optical properties of semiconductors. *Phys. Rev.*, 129(4):1550–1560, 1963.

[82] L. W. James, G. A. Antypas, J. J. Uebbing, et al. Optimization of the $InAs_xP_{1-x}$–Cs_2O photocathode. *J. Appl. Phys.*, 42(2):580–586, 1971.

[83] J. C. Woolley, C. M. Gillett, and J. A. Evans. Electrical and optical properties of GaAs-InAs alloys. *Proc. Phys. Soc.*, 77(3):700–704, 1961.

[84] L. W. James and J. J. Uebbing. Long-wavelength threshold of Cs_2O-coated photoemitters. *Appl. Phys. Lett.*, 16(9):370–372, 1970.

[85] J. Kessler. *Polarized Electrons*. Springer Series on Atomic, Optical, and Plasma Physics. Springer Berlin Heidelberg, 2013.

[86] R. Prepost and T. Maruyama. Advances in polarized electron sources. *Annu. Rev. Nucl. Part. Sci.*, 45(1):41–88, 1995.

[87] E. L. Garwin and D. T. Pierce. Polarized Photoelectrons from Optically Magnetized Semiconductors. *Helvetica Phys. Acta*, 47(4):393, 1974.

[88] R. R. Parsons. Band-to-band optical pumping in solids and polarized photoluminescence. *Phys. Rev. Lett.*, 23:1152–1154, 1969.

[89] M. I. D'yakonov, B. P. Zakharchenya, V. I. Perel', et al. Orientation of electron spins in semiconductors. *Sov. Phys. Uspekhi*, 14(6):806–807, 1972.

[90] F. Meier and B. Zakharchenya. *Optical Orientation*. Modern Problems in Condensed Matter Sciences. Elsevier Science, 2012.

[91] A. V. Subashiev and J. E. Clendenin. Polarized electron beams with P≥90%, will it be possible? *Int. J. Mod. Phys. A*, 15(16):2519–2527, 2000.

[92] Y. A. Mamaev, Y. P. Yashin, A. V. Subashiev, et al. Polarized elecrton photoemission studies of spin relaxation in thin GaAs epitaxial films. In *9th Int. Symp. "Nanostructures: Physics and Technology", St. Petersburg, Russia*, pages 234–237, 2001.

[93] P. Zorabedian. Optical pumping and photoluminescence detection of spin-polarized electrons in uniaxially stressed gallium arsenide. Doctoral Dissertation, Stanford University, 1982.

[94] F. Ciccacci, E. Molinari, and N. Christensen. GaAs/AlAs monolayer superlattices: A new candidate for a highly spin-polarized electron source. *Solid State Commun.*, 62(1):1 – 3, 1987.

[95] T. Maruyama, E. L. Garwin, R. Prepost, et al. Observation of strain-enhanced electron-spin polarization in photoemission from InGaAs. *Phys. Rev. Lett.*, 66(18):2376–2379, 1991.

[96] T. Maruyama, E. L. Garwin, R. Prepost, et al. Electron-spin polarization in photoemission from strained GaAs grown on $\mathrm{GaAs}_{1-x}\mathrm{P}_x$. *Phys. Rev. B*, 46(7):4261–4264, 1992.

[97] F. Meier, J. C. Gröbli, D. Guarisco, et al. Spin-polarized electrons from $\mathrm{In}_x\mathrm{Ga}_{1-x}\mathrm{As}$ thin films. *Phys. Scripta*, 1993(T49B):574, 1993.

[98] E. Pelucchi, S. D. Rossi, and F. Ciccacci. Spin polarized photoemission from thin GaAs photocathodes. *J. Electron Spectrosc. Relat. Phenom.*, 76(1):505 – 509, 1995.

[99] T. Nakanishi, H. Aoyagi, H. Horinaka, et al. Large enhancement of spin polarization observed by photoelectrons from a strained GaAs layer. *Phys. Lett. A*, 158(6):345 – 349, 1991.

[100] P. Hartmann, J. Bermuth, J. Hoffmann, et al. Picosecond polarized electron bunches from a strained layer GaAsP photocathode. *Nucl. Instruments Methods Phys. Res. Sect. A: Accel. Spectrometers, Detect. Assoc. Equip.*, 379(1):15 – 20, 1996.

[101] T. Omori, Y. Kurihara, T. Nakanishi, et al. Large enhancement of polarization observed by extracted electrons from the AlGaAs-GaAs superlattice. *Phys. Rev. Lett.*, 67:3294–3297, 1991.

[102] T. Omori, Y. Kurihara, Y. Takeuchi, et al. Highly polarized electron source using InGaAs–GaAs strained-layer superlattice. *Jpn. J. Appl. Phys.*, 33(10R):5676–5680, 1994.

[103] T. Nishitani, T. Nakanishi, M. Yamamoto, et al. Highly polarized electrons from GaAs–GaAsP and InGaAs–AlGaAs strained-layer superlattice photocathodes. *J. Appl. Phys.*, 97(9):094907, 2005.

[104] Y. A. Mamaev. Search for optimal photocathode structure for polarized electron sources. *Nucl. Instruments Methods Phys. Res. Sect. A: Accel. Spectrometers, Detect. Assoc. Equip.*, 536(3):289 – 294, 2005.

[105] A. Moy. Advanced strained-superlattice photocathodes for polarized electron sources. Technical report, SVT Associates Inc., 2005.

[106] J. van Laar and J. Schear. Influence of band bending on photoelectric emission from silicon single crystals. *Philips Res. Reports*, 17(2):101–124, 1962.

[107] J. Scheer and J. van Laar. Fermi level stabilization at cesiated semiconductor surfaces. *Solid State Commun.*, 5(4):303 – 306, 1967.

[108] J. van Laar and J. Scheer. Influence of volume dope on fermi level position at gallium arsenide surfaces. *Surf. Sci.*, 8(3):342 – 356, 1967.

[109] J. Scheer and J. van Laar. GaAs-Cs: A new type of photoemitter. *Solid State Commun.*, 3(8):189 – 193, 1965.

[110] A. A. Turnbull and G. B. Evans. Photoemission from GaAs-Cs-O. *J. Phys. D: Appl. Phys.*, 1(2):155–160, 1968.

[111] R. L. Bell and J. J. Uebbing. Photoemission from InP-Cs-O. *Appl. Phys. Lett.*, 12(3):76–78, 1968.

[112] W. E. Spicer and A. Herrera-Gomez. Modern theory and applications of photocathodes. In *Proc. SPIE, Photodetectors and Power Meters*, volume 2022, pages 18–35, 1993.

[113] L. W. James, G. A. Antypas, J. Edgecumbe, et al. Dependence on crystalline face of the band bending in Cs_2-Activated GaAs. *J. Appl. Phys.*, 42(12):4976–4980, 1971.

[114] B. F. Williams and J. J. Tietjen. Current status of negative electron affinity devices. *Proc. IEEE*, 59(10):1489–1497, 1971.

[115] B. Militsyn, I. Burrows, R. Cash, et al. First results from the III-V photocathod preparation facility for the ALICE ERL photoinjector. In *Proceedings of IPAC'10, Kyoto, Japan*, page 2347, 2010.

[116] V. V. Bakin, K. V. Toropetsky, H. E. Scheibler, et al. p-GaAs(Cs,O)-photocathodes: Demarcation of domains of validity for practical models of the activation layer. *Appl. Phys. Lett.*, 106(18):183501, 2015.

[117] G. Vergara, L. J. Gómez, J. Presa, et al. Electron diffusion length and escape probability measurements for *p*–type GaAs(100) epitaxies. *J. Vac. Sci. & Technol. A*, 8(5):3676–3681, 1990.

[118] B. Stocker. AES and LEED study of the activation of GaAs-Cs-O negative electron affinity surfaces. *Surf. Sci.*, 47(2):501 – 513, 1975.

[119] G. H. Olsen, D. J. Szostak, T. J. Zamerowski, et al. High-performance GaAs photocathodes. *J. Appl. Phys.*, 48(3):1007–1008, 1977.

[120] W. E. Spicer, P. W. Chye, P. R. Skeath, et al. New and unified model for schottky barrier and III–V insulator interface states formation. *J. Vac. Sci. & Technol.*, 16(5):1422–1433, 1979.

[121] M. G. Burt and V. Heine. The theory of the workfunction of caesium suboxides and caesium films. *J. Phys. C: Solid State Phys.*, 11(5):961, 1978.

[122] D. G. Fisher, R. E. Enstrom, J. S. Escher, et al. Photoemission characteristics of transmission-mode negative electron affinity GaAs and (ln,Ga)As vapor-grown structures. *IEEE Transactions on Electron Devices*, 21(10):641–649, 1974.

[123] J. J. Uebbing and L. W. James. Behavior of cesium oxide as a low workfunction coating. *J. Appl. Phys.*, 41(11):4505–4516, 1970.

[124] R. L. Bell and W. E. Spicer. 3-5 compound photocathodes: A new family of photoemitters with greatly improved performance. *Proc. IEEE*, 58(11):1788–1802, 1970.

[125] H. Sonnenberg. Low-work-function surfaces for negative-electron-affinity photoemitters. *Appl. Phys. Lett.*, 14(9):289–291, 1969.

[126] A. F. Milton and A. D. Baer. Interfacial barrier of heterojunction photocathodes. *J. Appl. Phys.*, 42(12):5095–5101, 1971.

[127] J. V. Laar and J. J. Scheer. Photoemission of semiconductors. *Philips Tech. Rev.*, 29(2):54–66, 1968.

[128] A. H. Sommer, H. H. Whitaker, and B. F. Williams. Thickness of Cs and Cs–O films on GaAs(Cs) and GaAs(Cs–O) photocathodes. *Appl. Phys. Lett.*, 17(7):273–274, 1970.

[129] D. G. Fisher, R. E. Enstrom, J. S. Escher, et al. Photoelectron surface escape probability of (Ga,In)As : Cs–O in the 0.9 to $\sim$1.6 μm range. *J. Appl. Phys.*, 43(9):3815–3823, 1972.

[130] C. Y. Su, W. E. Spicer, and I. Lindau. Photoelectron spectroscopic determination of the structure of (Cs,O) activated GaAs (110) surfaces. *J. Appl. Phys.*, 54(3):1413–1422, 1983.

[131] V. L. Alperovich, A. G. Paulish, and A. S. Terekhov. Unpinned behavior of the electronic properties of a *p*-GaAs(Cs,O) surface at room temperature. *Surf. Sci.*, 331–333(Part B):1250 – 1255, 1995.

[132] K. Hayase, T. Nishitani, K. Suzuki, et al. In situ observation of formation process of negative electron affinity surface of GaAs by surface photoabsorption. *Jpn. J. Appl. Phys.*, 52(6S):06GG05, 2013.

[133] S. Pastuszka, D. Kratzmann, D. Schwalm, et al. Elucidation of activation layer model by means of measurements of photoelectron energy distribution curves. *AIP Conf. Proc.*, 421(1):493–494, 1998.

[134] S. Moré, S. Tanaka, Y. Fujii, et al. Interaction of Cs and O with GaAs (100) at the overlayer–substrate interface during negative electron affinity type activations. *Surf. Sci.*, 527(1):41–50, 2003.

[135] F. Ciccacci and G. Chiaia. Comparative study of the preparation of negative electron affinity GaAs photocathodes with O_2 and with NF_3. *J. Vac. Sci. & Technol. A*, 9(6):2991–2995, 1991.

[136] N. Chanlek, J. D. Herbert, R. M. Jones, et al. High stability of negative electron affinity gallium arsenide photocathodes activated with Cs and NF_3. *J. Phys. D: Appl. Phys.*, 48(37):375102, 2015.

[137] G. A. Mulhollan and J. C. Bierman. Enhanced chemical immunity for negative electron affinity GaAs photoemitters. *J. Vac. Sci. & Technol. A*, 26(5):1195–1197, 2008.

[138] D. Allwood, N. Mason, A. Mowbray, et al. MOVPE homoepitaxial growth used to study the effect of aging and chemical treatment on GaAs substrates. *J. Cryst. Growth*, 248:108 – 113, 2003.

[139] C. D. Thurmond, G. P. Schwartz, G. W. Kammlott, et al. GaAs oxidation and the Ga–As–O equilibrium phase diagram. *J. The Electrochem. Soc.*, 127(6):1366–1371, 1980.

[140] J. J. Uebbing. Use of auger electron spectroscopy in determining the effect of carbon and other surface contaminants on GaAs-Cs-O photocathodes. *J. Appl. Phys.*, 41(2):802–804, 1970.

[141] A. Guillén-Cervantes, Z. Rivera-Alvarez, M. López-López, et al. GaAs surface oxide desorption by annealing in ultra high vacuum. *Thin Solid Films*, 373(1–2):159 – 163, 2000.

[142] C. L. Garden, E. W. Hoyt, D. C. Schultz, et al. Photocathode performance measurements for the SLC polarized electron gun. In *Proceedings of the Particle Accelerator Conference'93*, volume 4, pages 3039–3041, 1993.

[143] Y. Z. Liu, J. L. Moll, and W. E. Spicer. Effects of heat cleaning on the photoemission properties of GaAs surfaces. *Appl. Phys. Lett.*, 14(9):275–277, 1969.

[144] N. Chanlek, J. Herbert, L. Jones, et al. Study of activated GaAs surface for application as an electron source in particle accelerators. In *AIP Conference Proceedings*, volume 1149, pages 1022–1026, 2009.

[145] Y. Asaoka. Desorption process of GaAs surface native oxide controlled by direct Ga-beam irradiation. *J. Cryst. Growth*, 251(1–4):40 – 45, 2003.

[146] T. Maruyama, A. Brachmann, J. Clendenin, et al. A very high charge, high polarization gradient-doped strained GaAs photocathode. *Nucl. Instruments Methods Phys. Res. Sect. A: Accel. Spectrometers, Detect. Assoc. Equip.*, 492(1–2):199 – 211, 2002.

[147] S. Ohkouchi, N. Ikoma, and I. Tanaka. Scanning tunneling microscopy of argon-ion bombarded GaAs (100) surfaces. *J. Vac. Sci. & Technol. B*, 12(3):2030–2032, 1994.

[148] K. A. Elamrawi and H. E. Elsayed-Ali. GaAs photocathode cleaning by atomic hydrogen from a plasma source. *J. Phys. D: Appl. Phys.*, 32(3):251–256, 1999.

[149] D. Rodway, A. Cullis, and H. Webber. Laser cleaning of GaAs surfaces in vacuo. *Appl. Surf. Sci.*, 6(1):76 – 81, 1980.

[150] D. A. Orlov, C. Krantz, A. Wolf, et al. Long term operation of high quantum efficiency GaAs (Cs, O) photocathodes using multiple recleaning by atomic hydrogen. *J. Appl. Phys.*, 106(5):054907, 2009.

[151] A. Khatiri, J. Ripalda, T. Krzyzewski, et al. Atomic hydrogen cleaning of GaAs(001): A scanning tunnelling microscopy study. *Surf. Sci.*, 548(1–3):L1 – L6, 2004.

[152] P. Tomkiewicz, A. Winkler, and J. Szuber. Comparative study of the GaAs(100) surface cleaned by atomic hydrogen. *Appl. Surf. Sci.*, 252(21):7647 – 7658, 2006.

[153] S. Ritchie, S. Johnson, C. Lavoie, et al. Semiconductor substrate cleaning and surface morphology in molecular beam epitaxy. *Surf. Sci.*, 374(1):418 – 426, 1997.

[154] L. Hirsch, Z. Yu, S. Buczkowski, et al. The use of atomic hydrogen for substrate cleaning for subsequent growth of II-VI semiconductors. *J. Electron. Mater.*, 26(6):534–541, 1997.

[155] V. Tioukine, K. Aulenbacher, and E. Riehn. Hydrogen cleaning of superlattice photocathodes. In *SPIN PHYSICS: 18th International Spin Physics Symposium*, volume 1149, pages 1002–1006. AIP Publishing, 2009.

[156] M. Yamada and Y. Ide. Direct observation of species liberated from GaAs native oxides during atomic hydrogen cleaning. *Jpn. J. Appl. Phys.*, 33(5A):L671, 1994.

[157] Z. R. Wasilewski, J.-M. Baribeau, M. Beaulieu, et al. Studies of oxide desorption from GaAs substrates via Ga_2O_3 to Ga_2O conversion by exposure to Ga flux. *J. Vac. Sci. & Technol. B*, 22(3):1534–1538, 2004.

[158] T. Kikawa, I. Ochiai, and S. Takatani. Atomic hydrogen cleaning of GaAs and InP surfaces studied by photoemission spectroscopy. *Surf. Sci.*, 316(3):238 – 246, 1994.

[159] M. Yamada. GaOH: Unstable species liberated from GaAs surface oxides during atomic hydrogen cleaning. *Jpn. J. Appl. Phys.*, 35(5B):L651, 1996.

[160] E. J. Petit and F. Houzay. Optimal surface cleaning of GaAs (001) with atomic hydrogen. *J. Vac. Sci. & Technol. B*, 12(2):547–550, 1994.

[161] E. J. Petit, F. Houzay, and J. M. Moison. Interaction of atomic hydrogen with native oxides on GaAs(100). *J. Vac. Sci. & Technol. A*, 10(4):2172–2177, 1992.

[162] T. Sugaya and M. Kawabe. Low-temperature cleaning of GaAs substrate by atomic hydrogen irradiation. *Jpn. J. Appl. Phys.*, 30(3A):L402, 1991.

[163] A. Snelson. The reaction of atomic hydrogen with carbon. *Adv. Chem. Ser.*, (131):54–71, 1974.

[164] P. Tomkiewicz, A. Winkler, M. Krzywiecki, et al. Analysis of mechanism of carbon removal from GaAs(100) surface by atomic hydrogen. *Appl. Surf. Sci.*, 254(24):8035 – 8040, 2008.

[165] M. Baylac, P. Adderley, J. Brittian, et al. Effects of atomic hydrogen and deuterium exposure on high polarization GaAs photocathodes. *Phys. Rev. ST Accel. Beams*, 8:123501, 2005.

[166] R. Rahbi, B. Pajot, J. Chevallier, et al. Hydrogen diffusion and acceptor passivation in p-type GaAs. *J. Appl. Phys.*, 73(4):1723–1731, 1993.

[167] G. Bell, N. Kaijaks, R. Dixon, et al. Atomic hydrogen cleaning of polar III–V semiconductor surfaces. *Surf. Sci.*, 401(2):125 – 137, 1998.

[168] W. Mokwa, D. Kohl, and G. Heiland. Hydrogen adsorption on GaAs(110) studied by temperature-programmed desorption. *Phys. Rev. B*, 29(12):6709–6715, 1984.

[169] U. Bischler and E. Bertel. Simple source of atomic hydrogen for ultrahigh vacuum applications. *J. Vac. Sci. & Technol. A: Vacuum, Surfaces, Films*, 11(2):458–460, 1993.

[170] K. G. Tschersich and V. Von Bonin. Formation of an atomic hydrogen beam by a hot capillary. *J. Appl. Phys.*, 84(8):4065–4070, 1998.

[171] K. G. Tschersich, J. Fleischhauer, and H. Schuler. Design and characterization of a thermal hydrogen atom source. *J. Appl. Phys.*, 104(3):034908, 2008.

[172] K. G. Tschersich. Intensity of a source of atomic hydrogen based on a hot capillary. *J. Appl. Phys.*, 87(5):2565–2573, 2000.

[173] T. Schwarz-Selinger, A. von Keudell, and W. Jacob. Novel method for absolute quantification of the flux and angular distribution of a radical source for atomic hydrogen. *J. Vac. Sci. & Technol. A: Vacuum, Surfaces, Films*, 18(3):995–1001, 2000.

[174] M. Kuriki, C. Shonaka, H. Iijima, et al. Dark-lifetime degradation of GaAs photo-cathode at higher temperature. *Nucl. Instruments Methods Phys. Res. Sect. A: Accel. Spectrometers, Detect. Assoc. Equip.*, 637(1):S87 – S90, 2011.

[175] T. Wada, T. Nitta, T. Nomura, et al. Influence of exposure to CO, CO_2 and H_2O on the stability of GaAs photocathodes. *Jpn. J. Appl. Phys.*, 29(10R):2087, 1990.

[176] H. G. Andresen, K. Aulenbacher, T. Dombo, et al. Operating experience with the MAMI polarized electron source. In *Workshop on Photocathodes for Polarized Electron Sources for Accelerators, SLAC, California, USA.*, pages 2–12, 1993.

[177] M. Miyao, T. Wada, T. Nitta, et al. The state of Cs on negative electron affinity surfaces. *Appl. Surf. Sci.*, 33:364 – 369, 1988.

[178] Z. Jun-Ju, C. Ben-Kang, F. Xiao-Qian, et al. Influence of cesium on the stability of a GaAs photocathode. *Chin. Phys. B*, 20(8):087902, 2011.

[179] K. Aulenbacher, G. Arz, R. Barday, et al. Photocathode life time research at MAMI. *Proc. SPIN 2004*, page 975, 2005.

[180] M. Arnold, F. Hug, T. Kürzeder, et al. Final design and status of the third recirculation for the S–DALINAC. In *7th International Particle Accelerator Conference (IPAC'16), Busan, Korea*, pages 1717–1719, 2016.

[181] J. K. Fremerey. Residual gas: traditional understanding and new experimental results. *Vac.*, 53(1–2):197 – 201, 1999.

[182] G. Reich. Modern vacuum practice leak detection with tracer gases; sensitivity and relevant limiting factors. *Vac.*, 37(8):691 – 698, 1987.

[183] G. L. Gregory. Experimental study in vacuum of the rate–of–rise outgassing–measurement technique. Technical Report D-4973, National Aeronautics and Space Administration, USA, 1969.

[184] B. Halliday. Cleaning materials and components for vacuum use. *Vac.*, 37(8):587 – 591, 1987.

[185] A. Berman. Water vapor in vacuum systems. *Vac.*, 47(4):327 – 332, 1996.

[186] J. R. J. Bennett and R. J. Elsey. Anomalies in the measurement of the residual gases in a large UHV system using a quadrupole mass analyser. *Vac.*, 44(5):647 – 651, 1993.

[187] J. R. J. Bennett, S. Hughes, R. J. Elsey, et al. Outgassing from stainless steel and the effects of the gauges. *Vac.*, 73(2):149 – 153, 2004.

[188] R. Calder and G. Lewin. Reduction of stainless-steel outgassing in ultra-high vacuum. *Br. J. Appl. Phys.*, 18(10):1459, 1967.

[189] Y. Ishikawa and V. Nemanič. An overview of methods to suppress hydrogen outgassing rate from austenitic stainless steel with reference to UHV and EXV. *Vac.*, 69(4):501 – 512, 2003.

[190] W. Becker. The turbomolecular pump, its design, operation and theory; calculation of the pumping speed for various gases and their dependence on the forepump. *Vac.*, 16(11):625 – 632, 1966.

[191] D. Hucknall and D. Goetz. Turbomolecular pumps. *Vac.*, 37(8):615 – 620, 1987.

[192] A. Dallos. The pressure dependence of the pumping speed of sputter ion pumps. *Vac.*, 19(2):79 – 80, 1969.

[193] M. Audi and M. de Simon. Ion pumps. *Vac.*, 37(8):629 – 636, 1987.

[194] M. Audi. Pumping speed of sputter ion pumps. *Vac.*, 38(8):669 – 671, 1988.

[195] C. Benvenuti, P. Chiggiato, F. Cicoira, et al. Decreasing surface outgassing by thin film getter coatings. *Vac.*, 50(1–2):57 – 63, 1998.

[196] C. Benvenuti, J. Cazeneuve, P. Chiggiato, et al. A novel route to extreme vacua: the non-evaporable getter thin film coatings. *Vac.*, 53(1–2):219 – 225, 1999.

[197] C. Benvenuti, P. Chiggiato, P. C. Pinto, et al. Vacuum properties of TiZrV non-evaporable getter films. *Vac.*, 60(1–2):57 – 65, 2001.

[198] K. Yamazaki, J. Shike, M. Yamagata, et al. High-speed pumping to UHV. *Vac.*, 84(5):756 – 759, 2009.

[199] M. Succi, R. Canino, and B. Ferrario. Atomic absorption evaporation flow rate measurements of alkali metal dispensers. *Vac.*, 35(12):579 – 582, 1985.

[200] D. Heichelt. Characterization and optimizationof the wien filter and double-mott polarimeter at the test source of spin-polarized electrons Photo-CATCH. Bachelor Thesis, Technische Universität Darmstadt (unpublished), 2016.

[201] P. Krkotić. Development of a deflector cavity for the test source of polarized electrons Photo-CATCH. Bachelor Thesis, Technische Universität Darmstadt (unpublished), 2014.

[202] H. A. Rösch. Development of a LabVIEW based surface with an innovative control for the controlsystem of the spinpolarized electron test source Photo-CATCH. Bachelor Thesis, Technische Universität Darmstadt (unpublished), 2015.

[203] A. Kaiser. Development of a supercontinuum, a control system and further components of the test source for spin polarized electrons Photo-CATCH. Master Thesis, Technische Universität Darmstadt (unpublished), 2015.

[204] M. Michael. Production and investigation of pulsed polarized electron beams at the S-DALINAC. Bachelor Thesis, Technische Universität Darmstadt (unpublished), 2015.

[205] M. Wagner. Erzeugung und Untersuchung gepulster polarisierter Elektronenstrahlen am S-DALINAC. Doctoral Dissertation D-17, Technische Universität Darmstadt, 2013.

[206] M. Espig, J. Enders, Y. Fritzsche, et al. Investigation of pulsed spin-polarized electron beams at the S-DALINAC. In *Proceedings of the XVth International Workshop on Polarized Sources, Targets, and Polarimetry (PSTP)*, volume 1, page 059, 2013.

[207] K. Aulenbacher, V. Tioukine, M. Wiessner, et al. Status of the polarized source at MAMI. *AIP Conf. Proc.*, 675(1):1088–1092, 2003.

[208] S. Schippers. Electron–ion merged-beam experiments at heavy-ion storage rings. *Nucl. Instruments Methods Phys. Res. Sect. B: Beam Interactions with Mater. Atoms*, 350:61 – 65, 2015.

Acknowledgements

"I feel a very unusual sensation
- if it is not indigestion, I think it must be gratitude." -B. Disraeli

I cannot thank Prof. Joachim Enders enough for his guidance, motivation and help, of both professional and personal nature. I am also grateful to Prof. Markus Roth for co-supervising my work. As far as financial support is concerned, procurement of this degree would have been a hefty task if not for the generous scholarship granted by the German Academic Exchange Service (DAAD). Also, highly regarded are funds from German Research Foundation (DFG) through SFB-634 and GRK 2128 "Accelence" and the state of Hesse through HIC for FAIR, and the Federal Ministry of Research and Education (BMBF) position 05H15RDRB1.

It is impossible to put-down my gratitude to Markus in a few words, so I merely hope he understands how greatly I value the hand he never hesitated to lent throughout. Yuliya deserves a chunk of thanks for all the help and in addition, taking up the torturous job of correcting the first drafts of this dissertation. Thanks is also due to Martin for his unconditional help and the part he played in bringing the Photo-CATCH project to fruition. I am particularly grateful for all the advises offered by Dr. Marco Brunken throughout the duration of my employment. I greatly appreciate the support provided by the people at the mechanical and electronic workshops of IKP. I thank Prof. Hans-Joachim Kleebe and Mathis Müller from Institut für Angewandte Geowissenschaften of TUD for their help with the STEM investigations, and Dermati Kalliopi and Marc Wengenroth from GSI Helmholtz Centrum for assisting me with the processing of vacuum chambers.

Dear Olga, how can I express my gratitude to you for being my strongest support? Thanks also to both sides of my family for their care and love. I would like to wrap-up by remembering all those great teachers I was lucky enough to have, and all my good friends in India, Germany and elsewhere, and trust that they know who I am referring to should they ever read this note.

Neeraj Kurichiyanil

Curriculum Vitae

Neeraj Kurichiyanil

05 May 1988	Born in Calicut, Kerala, India.
2000-2003	Secondary Schooling, Kerala, India.
2003-2005	Higher Secondary Schooling, Kerala, India.
2005-2008	Bachelor of Science in Physics, University of Calicut, Kerala, India.
2008-2010	Master of Science in Physics, Cochin University of Science and Technology (CUSAT), Kerala, India Thesis: "*Synthesis and Characterization of Ferrofluids and Fabrication of Transient Hot Wire Setup for Thermal Conductivity Measurement of Fluids*", Magnetics Laboratory, Department of Physics, CUSAT.
2011-2012	Thesis, "*Developments for testing and optimizing the performance of photocathodes at the S-DALINAC polarized-electron injector*", Institut für Kernphysik, Faculty of Physics, TU Darmstadt, Germany.
2012-2016	DAAD PhD Scholarship, Institut für Kernphysik, TU Darmstadt, Germany.
Since 2016	Scientific assistant at Institut für Kernphysik, TU Darmstadt, Germany.

Erklärung zur Dissertation

Hiermit versichere ich, die vorliegende Dissertation ohne Hilfe Dritter nur mit den angegebenen Quellen und Hilfsmitteln angefertigt zu haben. Alle Stellen, die aus Quellen entnommen wurden, sind als solche kenntlich gemacht. Diese Arbeit hat in gleicher oder ähnlicher Form noch keiner Prüfungsbehörde vorgelegen.

Darmstadt, den January 4, 2017

(Neeraj Kurichiyanil)